

GRANT
IN-48-C12
185097

P-158

Equatorial Waves Simulated by the NCAR Community Climate Model

(NASA-CR-184645) EQUATORIAL WAVES SIMULATED
BY THE NCAR COMMUNITY CLIMATE MODEL (Iowa
State Univ. of Science and Technology)
158 p

N89-16246

CSSL 08C

Unclas

G3/48 0185097

Technical Report
Xinhua Cheng and Tsing-Chang Chen

October 1988

National Science Foundation
Grant No. ATM - 8611476
Washington, D.C.
and National Aeronautics and Space Administration
Grant No. NAG5-355
Washington, D.C.



ATMOSPHERIC SCIENCES PROGRAM
DEPARTMENT OF EARTH SCIENCES
IOWA STATE UNIVERSITY

Iowa State University
College of Sciences and Humanities
Department of Earth Sciences
Atmospheric Science Program

TECHNICAL REPORT

Equatorial Waves Simulated by the NCAR Community Climate Model

Ren-Yow Tzeng and Tsing-Chang Chen

CGO Projects: 420-21-14
422-21-15

Under contract with:

National Science Foundation
Grant No. ATM-8611476
Washington, D. C.

and

National Aeronautics and Space Administration
Grant No. NAG5-355
Washington, D. C.

Administered through:

Contracts and Grants Office
Ames, Iowa

October 1988

TABLE OF CONTENTS

	Page
I. INTRODUCTION	1
II. HISTORICAL DEVELOPMENT	5
A. Theoretical Work	5
B. Observational Studies	11
C. Model Simulations	17
III. MODEL AND EXPERIMENTS	25
A. The Model	25
1. The governing equations	25
2. The numerical algorithm	26
3. The initial and boundary conditions	28
a. The initial conditions	28
b. The boundary conditions	29
B. Model Simulations	30
1. The control experiment	30
2. The no-mountain experiment	31
3. The no-cloud experiment	32
IV. DATA AND COMPUTATIONAL SCHEME	34
A. Data	34
B. Computational Scheme	34
1. Pre-filtering	34
2. Lag-correlation and cross-power spectrum	36
3. Space-time spectral analysis	37
4. Maintenance equation	39

V. RESULTS	42
A. The Control Experiment	42
1. Mean zonal wind	42
2. Kelvin wave in the summer season	44
a. Spectral analysis	44
b. Propagation characteristics	47
c. Precipitation and forcing inference	54
d. Maintenance of the Kelvin wave	62
3. Kelvin wave in the winter season	69
a. Spectral analysis	69
b. Propagation characteristics	71
c. Maintenance of the Kelvin wave	73
4. Mixed Rossby-gravity wave in the summer season	75
a. Spectral analysis	75
b. Propagation characteristics	77
c. Precipitation and forcing inference	81
d. Maintenance of the mixed Rossby-gravity wave	83
5. Rossby wave in the winter season	88
a. Spectral analysis	88
b. Propagation characteristics	91
c. Maintenance of the Rossby wave	94
B. The No-mountain Experiment	98
1. Spectral analysis	99
2. Propagation characteristics	101
3. Precipitation and forcing inference	104

4. Maintenance of the Kelvin wave	108
C. The No-cloud Experiment	111
1. Winter zonal-mean wind	111
2. Spectral analysis	113
3. Propagation characteristics	115
4. Maintenance of the Kelvin wave	120
VI. CONCLUDING REMARKS	127
A. Summary and Discussion	127
B. Deficiencies of the Model Simulations	132
C. Suggestions for Future Study	133
VII. REFERENCES	135
VIII. ACKNOWLEDGMENTS	143
XI. APPENDIX	144

LIST OF FIGURES

	Page
Figure 1. A schematic illustration of equatorial planetary waves (extracted from Matsuno, 1966)	7
Figure 2. Time and zonally averaged zonal wind cross sections for the control experiment	43
Figure 3. Power spectral analyses of zonal wave 1 for the control experiment over the northern summer	45
Figure 4. Horizontal structures of Kelvin wave for the control experiment over the northern summer	49
Figure 5. Height-time cross sections of the Kelvin wave in the control experiment over the northern summer	52
Figure 6. Northern summer mean of precipitation rate and root mean square of the precipitation for the control experiment	55
Figure 7. Latitude-time cross sections of geopotential height and precipitation for the rate control experiment over the northern summer	56
Figure 8. Time series of amplitudes of Kelvin wave and precipitation rate for the control experiment over the northern summer	61
Figure 9. Various energy conversions of zonal wave 1 for the control experiment over the north summer	64
Figure 10. Nonlinear energy conversions of zonal wave 1 for the control experiment over the north summer	66
Figure 11. Power spectral analyses of zonal wave 1 for the control experiment over northern winter	70
Figure 12. Horizontal structures of Kelvin wave for the control experiment over the northern winter	72
Figure 13. Various energy conversions of zonal wave 1 for the control experiment over the northern summer	74
Figure 14. Power spectral analyses of zonal wave 5 for the control experiment over northern summer	76

Figure 15.	Horizontal structures of mixed Rossby-gravity wave in the control experiment over the northern summer	78
Figure 16.	Height-time cross section of the mixed Rossby-gravity wave in the control experiment over the northern summer	80
Figure 17.	Latitude-time cross sections of the mixed Rossby-gravity wave and precipitation rate for the control experiment over the northern summer	82
Figure 18.	Various energy conversions of zonal wave 5 for the control experiment over the northern summer	84
Figure 19.	Nonlinear energy conversions of zonal wave 5 for the control experiment over the northern summer	86
Figure 20.	Power spectral analyses of zonal wave 3 for the control experiment over the northern winter	89
Figure 21.	Horizontal structures of the Rossby wave in the control experiment over the northern winter	90
Figure 22.	Height-time cross sections of the Rossby wave in the control experiment over the northern winter	92
Figure 23.	Various energy conversions of zonal wave 3 for the control experiment over the northern winter	95
Figure 24.	Nonlinear energy conversions of zonal wave 3 for the control experiment over the northern winter	97
Figure 25.	Power spectral analyses of zonal wave 1 for the no-mountain experiment over the northern summer	100
Figure 26.	Horizontal structures of the Kelvin wave in the no-mountain experiment over the northern summer	102
Figure 27.	Height-time cross sections of the Kelvin wave in the no-mountain experiment over the northern summer	103
Figure 28.	Northern summer-mean of precipitation rate and root mean square of the precipitation for the no-mountain experiment	105
Figure 29.	Latitude-time cross sections of the Kelvin wave and the precipitation rate for the no-mountain experiment over the northern summer	107

Figure 30.	Various energy conversions of zonal wave 1 for the no-mountain experiment over the northern summer	109
Figure 31.	Time and zonally averaged zonal wind cross section for the no-cloud experiment over the northern winter	112
Figure 32.	Power spectral analyses of zonal wave 1 for the no-cloud experiment over the northern winter	114
Figure 33.	Horizontal structures of the kelvin wave in the no-cloud experiment over the northern winter	117
Figure 34.	Time evolution of the Kelvin wave in the no-cloud experiment over the northern winter	118
Figure 35.	Various energy conversions of zonal wave 1 for the no-cloud experiment over the northern winter	122
Figure 36.	Nonlinear energy conversions of zonal wave 1 for the no-cloud experiment over the northern winter	124
Figure A1.	Height-time cross sections of the Kelvin wave in the control experiment over the northern winter	145
Figure A1.	Northern winter-mean precipitation rate and its root mean square for the control experiment	146
Figure A3.	Latitude-time cross section of geopotential height and precipitation rate for the control experiment over the northern summer	147
Figure A4.	Time series of amplitudes of Kelvin wave and precipitation rate for the control experiment over the northern winter	148

LIST OF TABLES

	Page
Table 1. A description of the observed equatorial planetary waves	16
Table 2. Summary of three GCMs used to simulate equatorial planetary waves	18
Table 3. Characteristics of the equatorial planetary waves simulated by CCM1	48
Table 4. Various physical processes associated with wave maintenance	130

I. INTRODUCTION

Simulations of observed tropical climate by general circulation models (GCMs) have steadily improved over the last three decades as refinements have been made in the treatment of interactive physical processes and in the numerical techniques employed to solve the governing equations. Not only do we know that the tropics is a major energy source which drives the atmospheric motions, but we now need to examine the intricate interaction between middle latitudes and tropics. This investigation may have an important bearing on our understanding of long-term fluctuations of the global climate.

The large-scale motions in the tropics, which are quite different from those of midlatitude systems due to baroclinicity of the atmosphere, are driven primarily by latent heat released from strong cumulus convections. Because of the special nature of this driving force as well as the smallness of the Coriolis parameter, the large-scale motion system has certain distinctive structural features such as monsoon circulation associated with the tropical region of Asia and Africa, and east-west Walker circulation spanning the breadth of the Pacific Ocean.

Based upon a shallow water model, Matsuno (1966) investigated the nature of large-scale waves in the equatorial area. He found that two fundamental large-scale wave modes could exist in the equatorial atmosphere: westward moving mixed Rossby-gravity waves and eastward moving Kelvin waves. Later, observational studies by Yanai and Maruyama (1966) and Wallace and Gutzwiller (1968) confirmed the existence

of the equatorial planetary waves. These discoveries revived interest in wave disturbances in the tropics and have prompted subsequent observational and theoretical studies on this topic [see review articles by Wallace (1973) and Holton (1975)]. At present, three ideas appear true. First, both the Kelvin waves and the mixed Rossby-gravity waves are excited in the upper troposphere. Second, they are the predominant disturbances of the equatorial stratosphere. And third, through their vertical energy and momentum transport, the waves play a crucial role in the general circulation of the stratosphere.

In addition to their role in the stratospheric quasi-biennial oscillation, equatorial planetary waves also are believed to be responsible for the eastward propagating 30-50 day oscillations. Madden and Julian (1971; 1972) first described the 30-50 day oscillation as global-scale eastward propagating zonal circulation cell along the equator. Due to the propagating feature and time scale of the oscillation, Chang (1977) suggested that the eastward propagation is the manifestation of convectively driven equatorially trapped Kelvin waves. Following the same line, Lau and Peng (1987) recently proposed that the observed eastward propagation of intraseasonal oscillation in the tropical atmosphere arises as an intrinsic mode of oscillation resulting from an interaction of convection and dynamics via the so-called "mobile" wave-CISK mechanism. Through this mechanism, the heat source feeds on the east-west asymmetry of forced equatorial waves. As a result, Kelvin waves are selectively amplified and, in turn, cause the heat source to

propagate eastward.

Therefore, it is essential to simulate the equatorial planetary wave in a proper manner with a GCM before attempting to use it for climatic studies. Equatorial planetary waves have been simulated by both the GCM of the Geophysical Fluid Dynamics Laboratory (GFDL) (Hayashi, 1974) and by the first generation GCM of the National Center for Atmospheric Research (NCAR) (Kasahara et al., 1973). Since the NCAR Community Climate Model (CCM1) is the latest version of the spectral GCM at NCAR, we will examine its ability to successfully simulate the equatorial planetary waves. We shall also examine how these waves are maintained.

There have been several theoretical studies to explain the generation and maintenance of the equatorial planetary waves (see Chapter III for details). In view of the controversies among the proposed linear theories, we feel that numerical experiments with a GCM may be used to clarify some issues on the generation of the tropical disturbances. Three experiments with the NCAR CCM1 under seasonal variation conditions were analyzed in this study. The first is a control experiment run with complete physics. The second and the third experiments run without the effects of topography and clouds, respectively (see Chapter III for details).

The outline of this study is as follows: Chapter II reviews the past studies on the equatorial planetary waves. Chapter III describes the basic GCM used in this study and the three experiments. The data and computational schemes used in this study are discussed in Chapter

IV. The results are presented in Chapter V. Chapter VI presents the concluding remarks and future studies.

II. HISTORICAL DEVELOPMENT

There has been significant progress in observational and theoretical studies of equatorial planetary waves since the discovery of mixed Rossby-gravity waves and Kelvin waves in the equatorial stratosphere. In this chapter, we shall review the past studies on equatorial planetary waves. The review consists of three sections: Theoretical Work, Observational Studies, and Model Simulations.

A. Theoretical Work

The rotation of the earth dominates the way the atmosphere and ocean respond to imposed changes. This dynamic effect is caused by the Coriolis acceleration, which is equal to the product of the Coriolis parameter and the horizontal velocity. So the adjustment processes are somewhat special when the Coriolis acceleration vanishes.

Oceanographers found that an ocean channel enclosed in an equatorial zone can have an oscillatory mode whose period is much larger than one day. Stern (1963) first suggested this idea by considering inertial gravity waves in a rotating, homogeneous fluid confined between two concentric spheres of nearly equal radii. He showed that there exist standing oscillations of frequency $\Omega(nh/R)^{1/2}$, where Ω is the rate of rotation of the system, h is the thickness of the fluid, R is the mean radius of the spheres, and n is a positive integer. His analysis assumed that $h/R \ll 1$, and he showed that the wave amplitude decreases to zero outside a band of order $(h/R)^{1/2}$ on

either side of the equator.

Bretherton (1964) gave a simple explanation of this trapping phenomenon in terms of wave reflection. He suggested that outside a certain band, the Coriolis parameter is greater than the frequency of waves inside that band. For the waves in the band, both gravitational and Coriolis forces tend to restore a particle to its original latitude. Thus, there is a minimum frequency for the oscillation at a given latitude, namely, that of purely horizontal motions under the action of the Coriolis force. A wave travelling northward or southward must conserve this frequency, and cannot penetrate into a region where the Coriolis parameter exceeds it. So the wave is reflected and a standing oscillation is possible. He discussed baroclinic internal waves in the equatorial ocean using a two-layer model, and he showed that one such oscillation would have a period of about 10 days and would be trapped between 6N and 6S.

In order to study the atmospheric motions in the equatorial area, Matsuno (1966) derived a dispersion relation for the wave solution of the shallow water equations on an equatorial β -plane and gave the horizontal depictions of the wave disturbances, which are a set of equatorially trapped wave modes. Later, the theory of equatorial waves was extended to an isothermal atmosphere by Lindzen (1967) and Holton and Lindzen (1968).

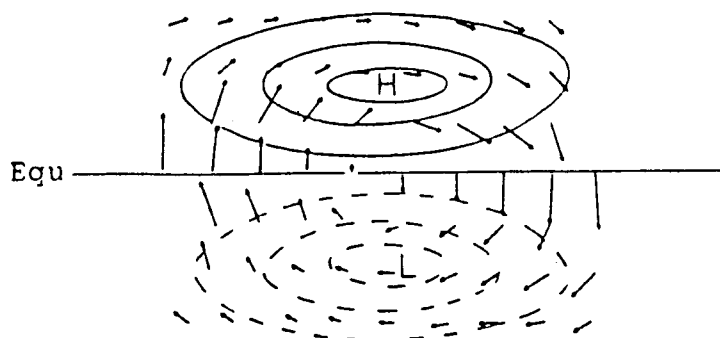
The resulting family of the wave mode in the shallow water model contains gravity and Rossby waves. The gravity waves propagate both eastward and westward, while Rossby waves only propagate westward with

slow velocity. These two types of waves are distinguished from each other by the difference of their frequencies. Namely, frequencies of the gravity waves are much larger than those of the Rossby waves.

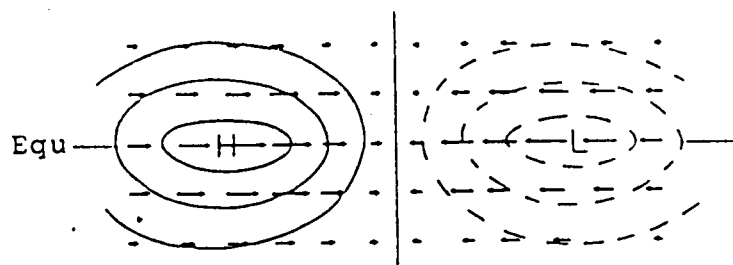
Figure 1a shows the horizontal pattern of the westward moving wave associated with the lowest mode in the wave family. This wave, with the smallest north-south extent, has antisymmetric structures in the temperature and zonal wind, and a symmetric structure in meridional wind with respect of the equator. Examining this figure, we note that this wave has somewhat mixed characteristics of the Rossby and gravity waves. The relationship between the pressure and the velocity fields is approximately geostrophic in the higher latitudes. But near the equator, ageostrophic wind components dominate. The configurations of wind and pressure fields near the equator resemble those of the gravity wave. The dispersion relationship of this wave is similar to that of the Rossby wave when the zonal wavelength is smaller than the meridional extent. For the long-wave part, however, the frequency becomes very long and approaches that of the gravity wave of the same wavelength. For this reason, the wave of this type is called a mixed Rossby-gravity wave.

By assuming zero meridional velocity, the shallow water equation has a special solution, which corresponds to an eastward moving wave with a phase velocity of pure gravity wave. Figure 1b shows the horizontal structure of this wave. It has symmetric structures across the equator in pressure and zonal wind fields and has no meridional velocity component. Figure 1b also shows that the wave behaves like a

(a) Westward Moving



(b) Eastward Moving



(c) Westward Moving

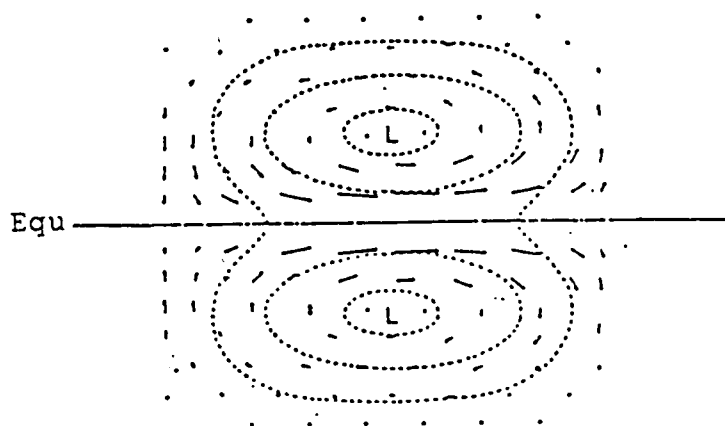


Figure 1. A schematic illustration of (a) mixed Rossby-gravity wave, (b) Kelvin wave and (c) equatorially trapped Rossby wave (extracted from Matsuno, 1966)

pure gravity wave in zonal direction. But in the north-south direction the geostrophic relation holds between zonal velocity and meridional pressure gradient. This type of wave is called a Kelvin wave which propagates along a coastal boundary and has no velocity component normal to the boundary. In the atmospheric case, the equator plays the same role as the coast line.

Figure 1c shows the horizontal distribution of the pressure and velocity fields of the lowest mode Rossby wave. The wave is characterized by the geostrophic balance between pressure and velocity fields. It is interesting that strong zonal velocity is found along the equator. We expect this strong velocity from the approximate geostrophic balance between the pressure gradient and wind.

A very important property of the equatorial disturbances is trapping of the low-frequency waves. In other words, the disturbances are confined to the vicinity of the equator. This trapping effect is entirely due to the variation of the Coriolis parameter. In the case of the inertial gravity wave, the trapping phenomenon can be interpreted from the viewpoint of reflection of the primary wave as explained by Bretherton (1964). The wave generated near the equator will be refracted and reflected toward the equator.

On the other hand, in the case of equatorial Kelvin wave, which propagates eastward with the velocity of a long gravity wave, the deviation of the surface elevation is just in geostrophic balance with the motion associated with the wave. Also, the amplitude of the wave decreases exponentially away from the equator. This changing of the

Coriolis parameter's sign near the equator confines Kelvin waves only in the vicinity of the equator. Here, the equator plays the role of a duct in the propagations of these waves.

Lindzen (1967) studied the vertical structures of equatorial waves in an isothermal atmosphere. He found that waves with periods of several days, which generally decay with height in the middle latitude, may become untrapped and propagate vertically near the equator due to the decreasing Coriolis frequency.

Vertically propagating wave disturbances in the equatorial area influence the atmospheric general circulation by transporting energy and momentum upward. Holton and Lindzen (1968) discussed the characteristics of the vertically propagating Kelvin wave in the tropical atmosphere. They found that the Kelvin wave with eastward tilting phase line is likely to be excited in the upper troposphere and transports westerly momentum upward. Therefore, Lindzen and Holton (1968) proposed a mechanism whereby interactions between the wave disturbances and the mean zonal flow could provide the momentum source for the quasi-biennial oscillation. On the other hand, the mixed Rossby-gravity wave, which tilts westward with height and transports westerly momentum upward, may be partly responsible for the easterly acceleration of the quasi-biennial oscillation of the equatorial stratospheric zonal wind.

The vertically propagating waves are continuously carrying energy upward from the lower atmosphere to an energy sink at a higher level. The energy sink may be the mean zonal flow. Or it may be eddy

viscosity or radiative dumping, if the waves propagate to very high levels without being absorbed by the mean zonal flow. Either case implies a source of wave energy in the lower atmosphere.

To show the steady circulation in the shallow water model, Matsuno (1966) worked out an example that included mass source and sink imposed alternately along the equator. The remarkable feature of the resultant motion is the strong zonal flow confined in the vicinity of the equator. This flow ridge and trough are located along the equator, which divides the pressure cell into two petals. Mathematically, this result can be explained by the fact that Rossby wave solution predominates while gravity waves are suppressed.

B. Observational Studies

Theoretical contributions by Matsuno (1966) and Lindzen (1967) have provided invaluable guidance in the planning of synoptic investigations and the interpretation of results. The existence of the mixed Rossby-gravity wave was confirmed by Yanai and Maruyama (1966) from analyses of wind data in the lower stratosphere over the Marshall Island in the equatorial Pacific. They noticed regular, wavelike fluctuations in the meridional wind component at stratospheric level. These disturbances were observed to propagate westward and downward with a horizontal wavelength of about 10,000 km, a vertical wavelength of about 6 km, and a period of 4-5 days.

Subsequent studies (Maruyama and Yanai, 1967; Maruyama, 1967) revealed the existence of associated fluctuations in the zonal wind component and in temperature. The observed phase relationships rotate

clockwise with time as waves pass, and the maximum temperature occurs at the time of the maximum southerly wind. The reverse is true for a point in the Southern Hemisphere. The waves have antisymmetry about the equator and appear to be confined within 12° of the equator. The horizontal structure and phase velocity of the observed disturbance showed close agreement with those of the mixed Rossby-gravity wave discussed by Matsuno (1966).

Lindzen and Matsuno (1968) further studied the mixed Rossby-gravity wave, observed by Yanai and Maruyama (1966), in terms of forced oscillations. Assuming the wave was excited in the lower part of the atmosphere, they were able to explain the importance of the wave's tilts and the wave's contributions to the mean zonal momentum.

Yanai et al. (1968) used the cross-spectrum analysis method to describe the more prominent fluctuations in the meridional wind component at tropospheric levels. The researchers found a wave mode at levels above 250 mb with a period of 4-5 days. The mode displays the same characteristics as the stratospheric mixed Rossby-gravity wave observed by Yanai and Maruyama (1966). Yanai et al. also established that the mixed Rossby-gravity waves exist in both upper troposphere and lower stratosphere.

The analysis of the large-scale wave in the lower stratosphere suggested the importance of inquiries into the upper troposphere, where the vertically propagating waves might be excited. Maruyama (1968b) and Yanai and Hayashi (1969) calculated vertical and horizontal transports of energy in the upper troposphere and the lower

stratosphere. They obtained the following results:

1. The vertical axis of the large-scale equatorial waves that move west relative to the basic wind have a westward tilt. That tilt indicates that the wave energy is transported upward, if the wind shear is not too strong.
2. The large-scale waves in the equatorial upper troposphere provide the lower stratosphere with wave energy. The vertical convergence of energy occurs at levels from 15-20 km.
3. In the lower stratosphere, horizontal convergence of wave energy occurs near the equator.

Soon after the discovery of 4-5 day stratospheric waves, Wallace and Kousky (1968) provided observational evidence for the existence of the disturbances in the zonal wind component with eastward and downward propagating phase line in the equatorial lower stratosphere. A distinguishing characteristic of the wave is the absence of fluctuations of the meridional wind. The zonal wind and pressure field were found to be in phase and oscillate with a period of 10-15 days and zonal wavenumber 1-2 with vertical wavelength of 5-10 km. This oscillation was identified as an atmospheric Kelvin wave discussed theoretically by Matsuno (1966), Lindzen and Holton (1968), and Holton and Lindzen (1968).

The observed temperature field of a Kelvin wave has a distinct fluctuation. Warmest temperatures precede the maximum westerly by 1/4 cycle, with both oscillations propagating downward. The wave

amplitude is largest at the equator and decays to about half the maximum value at 10° latitude.

This observational evidence suggests some physical interpretations as follows:

1. The absence of meridional wind fluctuations requires that the zonal wind component must be in geostrophic equilibrium with meridional pressure gradient. It follows that the levels of maximum zonal wind and maximum pressure should coincide.
2. Hydrostatic equilibrium requires that the warmest temperature be $1/4$ wavelength below the level of the maximum pressure.
3. The zonal momentum equation requires that maximum westerlies follow $1/4$ cycle behind the maximum east-west pressure gradient.
4. In the absence of the meridional wind component, continuity requires that the zonal wind and the vertical motion oscillations be in phase.

The upper stratospheric wave with period of 5-10 days found by Hirota (1978, 1979) is also likely to be a Kelvin wave and is associated with a larger vertical wavelength (20-25 km) than the lower stratospheric Kelvin wave. This upper stratospheric Kelvin wave may play an important role in the semiannual oscillation in the tropical middle atmosphere through a possible upward transport of eastward momentum as suggested theoretically by Dunkerton (1979; 1982).

At mesospheric levels, there is also evidence of faster eastward propagating disturbances. Salby et al. (1984) reported fluctuations,

identified with Kelvin mode associated with wavenumbers 1 and 2, in satellite observation between 16 and 70 km. The wavenumber 1 component had an eastward moving period of 35-40 days, and an eastward tilt of 40 km vertical wavelength, while the wavenumber 2 component had an eastward moving period of 3.8-4.3 days, and an eastward tilt of about 20 km vertical wavelength.

Recently, Zangvil and Yanai (1980), and Yanai and Lu (1983) presented a wavenumber-frequency analysis of the large-scale transient wave disturbances. The disturbances were at the 200 mb level in the latitude belt from 20S to 40N. The analysis was based on wind data collected during two northern summers, 1967 and 1972. Decomposing the wind data into symmetric and antisymmetric components with respect to the equator (Yanai and Murakami, 1970) and using the wavenumber-frequency analysis technique developed by Kao (1968) and Hayashi (1971; 1973), they were able to separate the equatorial disturbances into eastward and westward moving modes. Three types of equatorial waves were detected in the wind data of 1967: the Kelvin wave associated with zonal wavenumber $m=1$ and 2 and with a period of 7 days, and $m=1$ with a period longer than 20 days; a mixed Rossby-gravity wave associated with zonal wavenumber 4 and a period of 5 days; and an equatorially trapped Rossby wave with $m=2$ and a period near 10 days. On the other hand, in 1972, the mixed Rossby-gravity wave was absent and only weak signals of Kelvin waves with $m=1$ and 2 and the equatorially trapped Rossby wave with $m=2$ were found.

The researchers also showed that all the equatorially trapped

Table 1. A Description of the observed equatorial planetary waves

Theoretical description	Mixed Rossby-gravity waves		Kelvin waves			
	stratosphere	upper-troposphere	lower mesosphere	upper stratosphere	lower stratosphere	upper troposphere
Region of occurrence	Yanai & Maruyama (1966)	Zangvil & Yanai (1980)	Salby et al. (1984)	Hirota (1978,1979)	Wallace & Kousky (1968)	Zangvil & Yanai (1980) Yanai & Lu (1983)
Researcher	4-5 days	4-6 days	3.5-4.3 days	5-10 days	12-20 days	7 days, > 20 days
Periods	10,000 km	10,000 km	20,000 km	40,000 km	40,000 km	> 20,000 km
Horizontal wavelength	6 km		> 20 km	20-25 km	10 km	
Vertical wavelength	westward	westward	eastward	eastward	eastward	eastward
Direction of propagation	downward	downward	downward	downward	downward	downward
Amplitudes	2-3 m/s	1 m/s	3.5 K	3-5 K	8-12 m/s	1.5 m/s 2 m/s
Season	April-July 1962	June-August 1967	Jan-Feb 1979	two years 1973-74	July-Dec 1963,1964	June-Aug 1967

westward moving waves are associated either with equatorward energy flux at both 30N and 15S or with strong equatorward energy flux at 30N and weak poleward energy flux at 15S. They also showed that clear correspondence of the major peaks of meridional convergence of wave energy flux in the tropical belt to the equatorially trapped westward moving waves. Their findings strongly suggests that the westward moving waves may be excited by pressure work due to mid-latitude disturbances, i.e., lateral forcing. However, there was no evidence to suggest the association of the wave energy flux convergence with Kelvin waves.

Zangvil and Yanai (1980) analyzed cloud activities in the latitude belt 20S and 40N for the period June-August 1967 and found cloud activity was accompanied by the long-period eastward moving waves, whose characteristics were quite consistent with those of Kelvin waves.

In order to compare our results with the observational studies, we summarize in Table 1 the properties of Kelvin and mixed Rossby-gravity waves that have been identified observationally.

C. Model Simulations

Remarkable progress has been made in the linear theory and the analysis of the equatorial planetary waves. In order to have a better understanding of the tropical disturbances, the characteristics of the waves appearing in the general circulation models at both NCAR and GFDL have been analyzed. The features of the two models are summarized in Table 2.

Table 2. Summary of three GCMs used to simulate equatorial planetary waves

	NCAR 12-level grid-point PE model, Kasahara et al. (1973)	GFDL 11-level grid-point PE model, Hayashi (1974)	GFDL 40-level grid-point PE model, Hayashi et al. (1984)
Horizontal mesh	5° x 5°	2.4° x 2.4°	5° x 5°
Vertical mesh	12 levels in z-coordinate top level at 36 km	11 levels in σ -coordinate top level at 31 km	40 levels in σ -coordinate top level at 80 km
Independent variables	λ, ϕ, z, t	λ, ϕ, σ, t	λ, ϕ, σ, t
Prognostic variables	$\rho u, \rho v, \rho q, p$	$p^*u, p^*v, p^*T, p^*q, p^*$	$p^*u, p^*v, p^*T, p^*q, p^*$
Diagnostic variables	w, T, ρ	w, ϕ	w, ϕ
Physical processes	<ul style="list-style-type: none"> • Earth's orography • Surface and planetary boundary layer • Subgrid-scale processes • Convective adjustment • Interaction between radiation and clouds • Hydrological cycle • Computed land temperature • Climatological sea-surface temperature, ozone distribution and declination of the sun 	<ul style="list-style-type: none"> • Earth's orography • Planetary boundary layer • Subgrid-scale processes • Moist convective adjustment • Interaction between radiation and clouds • Hydrological cycle • Computed land temperature • Seasonal sea-surface temperature • Distribution of water vapor, ozone and carbon dioxide and declination of the sun 	<ul style="list-style-type: none"> • Earth's orography • Planetary boundary layer • Subgrid-scale processes • Moist convective adjustment • Short and longwave radiations • Hydrological cycle • Computed land temperature • Annual mean sea-surface temperature, cloudiness and pack ice • Fourier filtering at higher latitudes

Kasahara et al. (1973) and Tsay (1974) examined the characteristics of vertically propagating equatorial planetary waves appearing in a January simulation of the NCAR 12-layer stratospheric global circulation model with the top of the atmosphere extending to 36 km. Three types of dominant waves were identified by spectral peaks and phases in the model's lower stratosphere: the Kelvin waves with zonal wavenumber $m=1$ and 2, and with eastward-moving periods of 24 and 12 days, respectively; the mixed Rossby-gravity wave with zonal wavenumber $m=2$ and a westward-moving period of 4.6 days; and the Rossby wave type of free oscillation with zonal wavenumber $m=1$ and a westward-moving period of five days. Both Kelvin and mixed Rossby-gravity waves have a vertical wavelength of about 8.5 km. The amplitude of the Kelvin wave is about the same order of magnitude as that observed in the real atmosphere. However, the amplitude of the mixed Rossby-gravity wave is one order of magnitude smaller than that in the real atmosphere. The reason for this may lie with the prevailing easterlies in the model lower stratosphere.

Tsay (1974) showed that the Kelvin wave probably was determined by a certain filtering effect of the atmosphere since no peak in the tropospheric heating function existed at the wavenumber and frequencies of the Kelvin wave. Tsay also showed that the possible energy source of the Kelvin wave is the meridional energy convergence between 12 and 18 km over the equator.

The characteristic of the simulated Kelvin waves agreed well with those of observed Kelvin waves. However, the simulated wavenumber 1

oscillation had a significantly longer period. The vertical resolution or the forcing characteristics of the model would be responsible for the difference. Also, observations do not indicate wavenumber 2 Kelvin wave with period one-half that of wavenumber 1 oscillation. On the other hand, such a wave was found in Holton's (1973) linearized model with white-noise forcing. They theorized that the frequency was determined by the vertical wavelength that best fit the vertical scale of the forcing field.

Following the same line, Hayashi (1974) analyzed the equatorial waves simulated by the GFDL 11-layer general circulation model (for details, see Table 2). He included seasonal variation during July through October. In addition to easterly waves, three types of traveling waves were isolated from stationary waves and ultralong waves extending from middle latitudes:

1. Kelvin waves with wavenumber 1-2 and a period of 15 days. These waves attain their maximum amplitudes at 38 mb with their phase lines tilting eastward and westward with height in the stratosphere and the troposphere, respectively.
2. Mixed Rossby-gravity waves with wavenumbers 3-5 and a period of 3-5 days. These waves attain their maximum amplitudes at 110-190 mb with their phase lines tilting westward and eastward in the stratosphere and the troposphere, respectively.
3. Rossby-type waves with wavenumbers 1-5 and a period of 15 days. These waves attain their maximum amplitudes at 110-190

mb with their phase lines tilting westward and eastward in the stratosphere and the troposphere, respectively.

All of these traveling waves are maintained primarily by the conversion of available potential energy generated by condensational heating. Due to the coupling between large-scale disturbances and convection, presumably through moisture convergence as in the case of the CISK theories, a broad spectrum of waves are generated and maintained by the latent heat released by the rainfall. The spectra are not random noise, but instead, exhibit certain characteristic wavenumbers and phase velocities.

Hayashi et al. (1984) also analyzed the large-scale equatorial disturbances simulated by the 40-level GFDL general circulation model with annual mean condition. Even though the model had no seasonal cycles, the large-scale equatorial eastward moving disturbances were still successfully simulated and agreed with observations by Wallace and Gutzwiller (1968), Hirota (1978, 1979), and Salby et al. (1984). However, the model did not detect mixed Rossby-gravity waves.

There are, in general, three theories to explain the generation and selection of large-scale equatorial disturbances. The first approach is the theory of resonance to midlatitude forcing (Mak, 1969). Mak found that westward moving equatorial waves exhibit a large resonant response at a period of four days with wavenumber 4. He also found that the waves derive their energy from midlatitude disturbances. His result is consistent with wave propagation theories. According to Charney (1969), waves moving westward relative

to the basic wind can propagate into the tropics, provided the horizontal shear is not too strong and the vertical scale is not too short.

The second approach was an instability (CISK) theory by Hayashi (1970). The theory assumes that convective heating is proportional to surface convergence due to large-scale waves. The researchers found that the instability allows the existence of mixed Rossby-gravity waves and Kelvin waves with realistic three-dimensional structure. However, waves preferred scale did not agree with their observed. This difficulty can be avoided, however, by assuming that cumulus heating becomes inefficient for high-frequency waves due to the constraint of moisture availability (Kuo, 1975). Moreover, the CISK theories also predict sharp spectral peaks in the tropical rainfall which are not clearly detected in general circulation models (Tsay, 1974; Hayashi, 1974).

The third approach is to examine the response of the atmosphere to random thermal forcing in the presence of a vertical wind shear, since the atmospheric heating field does not have spectral peaks at the wavenumbers and frequencies of the observed Kelvin waves and mixed Rossby-gravity waves. Holton (1972) demonstrated that both eastward and westward moving waves were excited in the troposphere by a localized tropospheric heat source pulsating with an imposed periodicity. However, depending on the vertical profile of wind, eastward moving Kelvin waves or westward moving mixed Rossby-gravity waves propagate into the stratosphere. Holton (1973) further pointed

out that a 10-30 day spectral peak in tropospheric thermal forcing is not required to account for the observed spectral distribution of stratospheric Kelvin waves, since the atmosphere acts as a bandpass filter to select these waves. This point was confirmed by the spectral analysis of the general circulation model (Tsay, 1974; Hayashi, 1974).

In view of the controversies among these linear theories, Hayashi and Golder (1978) made an attempt to clarify, to some extent, the causes of the generation of an equatorial planetary wave. He conducted control experiments with a GFDL 13-level general circulation model (for details, see Table 2). By successively eliminating the effects of topography, midlatitude disturbances, and condensational heat from the model, he showed the following results:

1. The amplitude and the characteristic scale and period of both Kelvin and mixed Rossby-gravity waves are hardly affected by the land-sea contrast or the zonal variation of sea surface temperature.
2. Kelvin waves are hardly affected by midlatitude disturbances. But the waves diminish drastically after condensational heat is also eliminated.
3. Mixed Rossby-gravity waves are significantly reduced in amplitude by the elimination of midlatitude disturbances. They diminish completely after latent heat is also eliminated.
4. The total kinetic energy of all equatorial transient

disturbances is generated primarily as the result of latent heat release in the tropics. That of subtropical transient disturbances is reduced significantly in the absence of midlatitude disturbances.

It is of interest to compare Hayashi's results with the existing theories mentioned above. His results are consistent with these theories in that the topographical effect is not an essential factor for the characteristic scale and period of both Kelvin and mixed Rossby-gravity waves. The results are similar to those of both the CIKS and random thermal forcing theories in that both Kelvin and mixed Rossby-gravity waves appear in the stratosphere as a result of latent heat release in the troposphere. On the other hand, the present results are also similar to those of lateral forcing theories in that mixed Rossby-gravity waves can be significantly enhanced by midlatitude disturbances. However, these waves are not generated by midlatitude disturbances in the absence of condensational heating.

Although the above theories have their own drawbacks, they should not be entirely rejected since the nonlinear effect is neglected.

III. MODEL AND EXPERIMENTS

A. The Model

The GCM used in this study is the latest version of the NCAR Community Climate Model version 1 (CCM1). This version has evolved over the last few years from the earlier CCM0B. Substantial changes have been incorporated into the radiation scheme in both the physical parameterizations and the actual structure of the code.

This model was chosen because it is designed for global forecast studies (both medium- and long-range) as well as climate simulations, and because it is widely used for both purposes by university as well as NCAR scientists.

1. The governing equations

The governing equations are similar to those used by Bourke (1974) and Hoskins and Simmons (1975). These equations adopt the vertical coordinate $\sigma = p/p_s$ (p_s is the surface pressure) proposed by Phillips (1957). In the σ -coordinate, the ground is a coordinate surface so that the effect of mountains can easily be incorporated without introducing problems associated with uncentered horizontal differencing. The governing equations include the following:

- the vorticity (η) and divergence (δ) equations;
- the thermodynamic equation; and
- the moisture (q) forecast and continuity equations. The continuity equation is not used directly but, when integrated in the vertical, gives equations for the surface-pressure

tendency and for $\dot{\sigma}$.

Included in the model are the following parameterized physical processes: convection and condensation (Manabe et al., 1965); fluxes of sensible and latent heat following a bulk aerodynamic formulation with the assumption of no heat storage over land; and interactions with subgrid-scale motions through horizontal and vertical diffusion. Moisture in excess of 100% relative humidity is precipitated without evaporation of the condensation in intervening layers. The algorithm is essentially that used in CCM0 and represented in Ramanathan et al. (1983).

2. The numerical algorithm

The model uses a semi-finite difference scheme in space and a central and semi-implicit scheme in time. The vertical and temporal aspects of the model are represented by finite-difference approximations, while the horizontal aspects are treated by the spectral-transform method. In general, physical parameterizations and nonlinear operations are carried out in grid-point space. Horizontal derivatives and linear operations are performed in spectral space. The horizontal representation of an arbitrary variable Q is expanded in a truncated series of surface spherical harmonics:

$$Q(\lambda, \mu) = \sum_{m=-M}^M \sum_{n=|M|}^{N(m)} Q_n^m P_n^m(\mu) e^{im\lambda} \quad (3.1)$$

where

$$\mu = \sin\phi,$$

ϕ = latitude,

λ = longitude,

M = highest Fourier wavenumber included in the east-west representation, and

$N(m)$ = highest degree of the associated Legendre functions included in the north-south representation (can be a function of the Fourier wavenumber (m)).

In this study, the surface spherical harmonics are truncated rhomboidally at wavenumber 15. The associated Gaussian grid has 48 points in longitude with a spacing of 7.5 degrees and 40 points in latitude with an approximate spacing of 4.5 degrees. The algebra involved in the spectral transformations has been presented in several publications (Daley et al., 1976; Bourke et al., 1977; Machenbauer, 1979).

Finite differences are used in the vertical. The model levels, at which σ assumes the values of 0.991, 0.926, 0.811, 0.644, 0.500, 0.336, 0.189, 0.074, and 0.009, are identical to those chosen by McAvaney et al. (1978) and to those used in many GFDL model simulations. On the vertical discrete grid, all prognostic variables and geopotentials are carried at full-index σ -levels, while the vertical velocity $\dot{\sigma}$ is carried by half-index σ -levels. The vertical finite differences are a combination of two differences: 1) the difference adopted by the Australian Numerical Meteorological Research Centre (ANMRC) model (Bourke, 1974; Bourke et al., 1977), and thus by CCM0 and 2) those differences used in the first European Center for

Medium Range Weather Forecast (ECMWF) model (Burridge and Haseler, 1977). The full-index σ -values of grid levels are specified as input to the model. The half-index levels are given as the average of the adjacent full-index levels with the end values set to 0 and 1.

The time differences are basically centered with the terms responsible for fast-moving gravity waves treated semi-implicitly (Hoskins and Simmons, 1975). The vertical and horizontal diffusion terms are treated implicitly using a time-splitting procedure--vertical before the advection processes and horizontal after. After the time step is completed, the temperature and mixing ratios are convectively adjusted. And finally, a time filter is applied to the prognostic variables $\ln p_s$, T , q , δ , and q . The time filter was originally designed by Robert (1966) and later studied by Asselin (1972).

3. The initial and boundary conditions

a. The initial conditions The basic initial data for the model consists of values of u , v , T , q , p_s and ϕ_s on the Gaussian grid at time $t=0$. From these, $U(=u \cos\phi)$, $V(=v \cos\phi)$, T' , and $\ln p_s$ are computed on the grid. The Fourier coefficients of these variables U^m , V^m , T'^m , Q^m , $\ln p_s^m$ are determined via an FFT subroutine. The spherical harmonic coefficients $T'_n{}^m$, $q_n{}^m$, $\ln p_{sn}{}^m$, and $\phi_{sn}{}^m$ are determined by Gaussian quadrature. The relative vorticity ζ and divergence δ spherical harmonic coefficient are determined directly from the Fourier coefficients U_m and V_m using the relations

$$\zeta = \frac{1}{a(1-\mu^2)} \frac{\partial V}{\partial \lambda} + \frac{1}{a} \frac{\partial U}{\partial \mu} , \quad (3.2)$$

$$\delta = \frac{1}{a(1-\mu^2)} \frac{\partial U}{\partial \lambda} + \frac{1}{a} \frac{\partial V}{\partial \mu} . \quad (3.3)$$

The first-time step of the model is forward semi-implicit rather than centered semi-implicit. Therefore, only variables at $t=0$ are needed.

b. The boundary conditions The required boundary data are surface temperature T_s at each ocean point, the surface geopotential at each point, the soil moisture at each ocean point, and the snow amount at nonocean points. However, these data are used only as the first guess in the T_s calculation the first time and are never used again.

When the model is run with seasonal cycle, the sea-surface temperature (SST), sea-ice locations, and snow cover are changed to reflect the seasonal changes. The SST and sea-ice distributions are specified from the monthly mean analysis of Alexander and Mobley (1976). The monthly mean SST values are assigned the mid-month date and updated every 12 hours at each grid point using linear interpolation.

The sea-ice and snow cover are updated at the beginning of every month and are held fixed during the month. The snow cover is a

function of latitude only. The radiation parameterization requires monthly mean ozone mixing ratios and the surface albedo.

B. Model Simulations

For the purpose of this study, three numerical experiments with the NCAR CCMI general circulation model were analyzed. The three experiments were the control experiment, the no-mountain experiment, and the no-cloud experiment.

1. The control experiment

Equatorial planetary waves have been well simulated by both the NCAR (Tsay, 1974) and GFDL (Hayashi, 1974) general circulation models, although the formulations of the GCM used by the two groups vary considerably. Since the CCM is now commonly used for climate studies for troposphere dynamics, the CCMI is the latest version of the GCM with substantial changes incorporated in the radiation scheme. It is of interest to see to what extent the model can simulate the equatorial planetary waves.

The control experiment, with various physics as described in the previous section, was initialized from real data in December 1, 1972 and integrated for four years with seasonal forcing (i.e., sea-surface temperature, sea-ice distribution and solar zenith angle) until the model reached its equilibrium state. Then, the experiment was run for an additional year. Only the last year's experiment instead of that of the first four years was used in order to avoid the effects of initial transients.

2. The no-mountain experiment

There have been numerous studies of the effects of large-scale orography on atmospheric flow. The major effects of large-scale orography which have been identified are:

- The Siberian high appears concurrent with the appearance of the mountain and relates to the mountain's height. A stationary trough appears in the lees of the major mountain ranges (Manabe and Terpstra, 1974; Mintz, 1965).
- The presence of mountains is instrumental in maintaining the South Asian low pressure system and helps to extend a monsoon climate farther north onto the Asian continent (Hahn and Manabe, 1975).
- The subtropical jet streams are weaker and the stationary waves have smaller amplitudes in the no-mountain case than do those in the mountain case (Blackmon et al., 1987).
- The model without mountains produces a more zonally uniform distribution of tropical precipitation.

Therefore, since there is no topographic effect to fix the stationary wave's nodes and antinodes, the no-mountain experiment weakens not only stationary waves, but also standing wave oscillations. Consequently, the interaction between midlatitudes and tropics, which is essentially contributed by the stationary ultralong waves, is also reduced. It will be of interest to examine whether reducing the interaction between midlatitude and tropics affects the characteristic scales and periods of the equatorial planetary waves.

In this experiment, all conditions remained the same as those in the control except for the elimination of topographical effects by replacing the model's surface with ocean points. The numerical time integration was then carried out with the same procedure as the control experiment.

3. The no-cloud experiment

Cumulus convection and latent heat release play key roles in determining the structure of the temperature and moisture fields in the atmosphere. Heating and moistening, due to these processes, interact with radiation and large-scale dynamics in determining important aspects of the general circulation. Due to the monsoon type of the circulation, the energy is transported up from the warm sea-surface temperature area by means of cumulus convection and latent heat release in the tropics. This transport is confirmed by Donner et al. (1982). From a GCM simulation, they showed that cumulus convection warms the upper troposphere and slightly cools the lower tropical troposphere. In general, the large-scale motions of the atmosphere organize the pattern of heating. According to the satellite observations of cloud cover compiled by Sadler (1970), intense convection is associated particularly with the northern part of South America, equatorial Africa, and equatorial western Pacific. Also, the convection is associated with the intertropical convergence zone (ITCZ) and the South Pacific convergence zone (SPCZ). One might expect that the heating due to the latent heat released by condensation is significant over these areas. Cumulus convection, as

feedback, influences the large-scale atmospheric motion both directly through heating and moistening and also indirectly by inducing changes in the meridional circulation. Chen and Baker (1986) calculated the global diabatic heating during FGGE year and pointed out that the diabatic heating in the tropics largely balanced by the vertical motion.

Previous studies (Hayashi, 1970; Holton, 1972) suggested that the latent heat release, which is essential in both the CISK theories and thermal forcing theories, is the possible energy source of the equatorial planetary waves. A no-cloud experiment serves the purpose to examine the generation and maintenance of the equatorial planetary waves in the absence of cumulus convection in the atmosphere.

The no-cloud experiment is identical to the control experiment, except that the cloud formation system in the model was turned off.

IV. DATA AND COMPUTATIONAL SCHEME

A. Data

In this study, we have analyzed three experiments of the NCAR CCM1 global general circulation model. The three experiments are control, no-mountain, and no-cloud experiments. For each experiment, we used two data samples during the periods December 1 to April 30 (winter) and May 1 to September 27 (summer), 1977, the fourth year of the model simulation. Daily simulations were stored for analysis. The data are gridded on an approximately $7.5^\circ \times 4.5^\circ$ mesh in the horizontal and seven levels in the vertical. Since each experiment was run continuously for five years, the data used in this study contain seasonal cycle.

B. Computational Scheme

This study involves several different statistical computational schemes. Among these schemes, space-time spectral analysis is estimated by the lag-correlation method. This section is devoted to a brief description of these schemes.

1. Pre-filtering

In order to isolate the tropical perturbation signals in which we are interested, we have designed a pre-filtering method which removes seasonal cycle and minimizes the signals with periods longer than 30 days.

Seasonal cycle is removed by using the least squares fit method (Bendat and Piersol, 1971). Let $\{U_n\}$, $n=1,2,\dots,N$ be the data values

sampled at an interval of h . Suppose it is desired to fit these data with a polynomial of degree k defined by

$$\hat{U}_n = \sum_{k=0}^K b_k (nh)^k \quad n=1,2,\dots,N \quad (4.1)$$

In a least square fit, the set of coefficients $\{b_k\}$ are chosen so as to minimize the expression

$$Q(b) = \sum_{n=1}^N (U_n - \hat{U}_n)^2 = \sum_{n=1}^N [U_n - \sum_{k=0}^K b_k (nh)^k]^2 \quad (4.2)$$

The desired coefficients can be obtained by taking partial derivatives of Equation (2) with respect to b_ℓ and setting them equal to zero:

$$\frac{\partial Q}{\partial b_\ell} = \sum_{n=1}^N 2[U_n - \sum_{k=0}^K b_k (nh)^k] [-(nh)^\ell] \quad (4.3)$$

This yields $K + 1$ equations of the form

$$\sum_{k=0}^K b_k \sum_{n=1}^N (nh)^{k+\ell} = \sum_{n=1}^N U_n (nh)^\ell \quad \ell=0,1,2,\dots,K \quad (4.4)$$

which now can be solved for the desired $\{b_k\}$.

Since we expect to remove the annual cycle mode in the data, we, therefore, choose $k=2$. In other words, we take second order polynomials to represent the seasonal cycle. The set of coefficients b_0 , b_1 and b_2 are determined by Equation (4.4).

In order to study the transient perturbances in the tropics, we

must separate these modes from the lower frequency signals, which usually obscure the higher frequency signals because of larger energy content. This task is carried out by applying a second-order Butterworth bandpass filter from the FDPACD package stored in the NCAR software library to the time series of the Fourier coefficients. By doing this, signals with periods smaller than 30 days are kept constant, while those with periods longer than 30 days are reduced.

2. Lag-correlation and cross-power spectrum

Following Bath (1974), we assume a real time function $f(t)$ having a fundamental period of 2π and satisfying Dirichlet's conditions can be represented by the following infinite Fourier series:

$$f(t) = \sum_{\omega=-\infty}^{+\infty} F(\omega) e^{-i\omega t} \quad (4.5)$$

and $F(\omega)$ is the Fourier coefficient given by

$$F(\omega) = \frac{1}{2\pi} \int_0^{2\pi} f(t) e^{i\omega t} dt \quad (4.6)$$

Now we consider the same conditions for another two time functions $f_1(t)$ and $f_2(t)$. The lag correlation function is defined as follows:

$$C_{12}(\tau) = \int_{-\infty}^{+\infty} f_1(t) f_2(t+\tau) dt \quad (4.7)$$

Cross-power spectrum is defined as

$$E_{12}(\omega) = F_1^*(\omega) F_2(\omega) \quad (4.8)$$

It can be proved immediately that the cross-correlation forms a Fourier pair with the cross-power spectrum:

$$C_{12}(\tau) = \frac{1}{2\pi} \int_{-\infty}^{+\infty} E_{12}(\omega) e^{i\omega\tau} d\omega \quad (4.9)$$

$$E_{12}(\omega) = \int_{-\infty}^{+\infty} C_{12}(t) e^{-i\omega\tau} d\tau \quad (4.10)$$

In general, the cross-power spectrum $E_{12}(\omega)$ is complex:

$$E_{12}(\omega) = K_{12}(\omega) + iQ_{12}(\omega) \quad (4.11)$$

where $K_{12}(\omega)$ is the cospectrum and $Q_{12}(\omega)$ is the quadrature spectrum.

3. Space-time spectral analysis

In order to interpret observed and simulated disturbances in terms of theoretical wave modes, it is helpful to analyze these disturbances into space-time Fourier components. However, due to the stochastic nature of atmospheric waves, these space-time Fourier components are random variables and are not in themselves statistically and physically meaningful. For this reason, space-time spectral analyses (Kao, 1968; Hayashi, 1971; 1973) have been developed to obtain statistically meaningful results from a given space-time series which is cyclic in space and limited in time.

Let $q(\lambda, t)$ be a real, single-value function that is piecewise differentiable in a normalized domain, $0 \leq \lambda, t \leq 2\pi$, where λ and t stand for longitude and time, respectively. For convenience, a discrete representation is used for frequency as well as wavenumber. $q(\lambda, t)$ can be expanded into a space-time Fourier series as

$$q(\lambda, t) = \sum_{k=-\infty}^{+\infty} \sum_{\omega=-\infty}^{+\infty} Q(k, \omega) e^{i(k\lambda + \omega t)} \quad (4.12)$$

where $Q(k, \omega)$ is the complex space-time transform determined by

$$Q(k, \omega) = \frac{1}{4\pi^2} \int_0^{2\pi} \int_0^{2\pi} q(\lambda, t) e^{-i(k\lambda + \omega t)} d\lambda dt \quad (4.13)$$

Consider the same conditions for another scalar function $q'(\lambda, t)$ with a Fourier transform $Q'(k, \omega)$. Thus, the contribution of $q(\lambda, t)$ and $q'(\lambda, t)$ integrated over a latitude circle and over a normalized time interval 2π may then be expressed in terms of the sum of $Q(k, \omega)$ and $Q'(k, \omega)$ integrated over the frequency and wavenumber domain:

$$\frac{1}{4\pi^2} \int_0^{2\pi} \int_0^{2\pi} q(\lambda, t) q'(\lambda, t) d\lambda dt = \sum_{k=0}^{+\infty} \sum_{\omega=0}^{+\infty} E_{qq'}(k, \pm\omega) \quad (4.14)$$

where $E_{qq'}(k, \pm\omega)$ is the cross-power spectrum of $q(\lambda, t)$ and $q'(\lambda, t)$ due to eddies of wavenumber k and frequency ω . The positive and negative frequencies correspond to eastward and westward velocity, respectively.

The cross-power spectrum between two sets of time series (q, q')

is formulated as

$$\begin{aligned} \text{Eqq}'(k, \pm\omega) &= K_\omega(C_k, C_k) + K_\omega(S_k, S_k) \\ &\quad \pm Q_\omega(C_k, S_k) \mp Q_\omega(S_k, C_k) \end{aligned} \quad (4.15)$$

where K and Q denote cospectra, quadrature spectra, and C_k and S_k are the cosine and sine space Fourier coefficients of $q(\lambda, t)$.

In particular, the power spectrum of the scalar quantity $q(\lambda, t)$ is given by

$$\begin{aligned} P_q(k, \pm\omega) &= \text{Eqq}(k, \pm\omega) \\ &= P_\omega(C_k) + P_\omega(S_k) \pm 2Q_\omega(C_k, S_k) \end{aligned} \quad (4.16)$$

where P_ω is the time power spectrum of a time series.

4. Maintenance equation

The maintenance of the equatorial disturbances will be investigated by using the energy transfer formulas derived by Hayashi (1980).

In spherical coordinates, the time change of wavenumber kinetic energy for large-scale motions is given by

$$\begin{aligned} \frac{\partial K_n}{\partial t} &= N_n(k) - P_n(\alpha, \omega) \\ &\quad - \left[\frac{\partial P_n(\phi, \nu)}{\partial y} + \frac{\partial P_n(\phi, \omega)}{\partial p} \right] \end{aligned} \quad (4.17)$$

where P_n is the wavenumber cospectrum. The kinetic energy per unit

mass, K_n , for the wavenumber n is defined by

$$K_n = \frac{1}{2} [P_n(u,u) + P_n(v,v)] , \quad (4.18)$$

and the nonlinear kinetic energy transfer spectrum $N_n(k)$ is defined by

$$\begin{aligned} N_n(K) = & - [P_n(u, \frac{\partial uu}{\partial x}) + P_n(v, \frac{\partial vv}{\partial x})] \\ & - [P_n(u, \frac{\partial uv}{\partial y}) + P_n(v, \frac{\partial vv}{\partial y})] \\ & + \frac{\tan\theta}{r} [P_n(u, uv) - P_n(v, uu)] \\ & - [P_n(u, \frac{\partial u\omega}{\partial p}) + P_n(v, \frac{\partial v\omega}{\partial p})] . \end{aligned} \quad (4.19)$$

Here,

$$\frac{\partial(\)}{\partial y} = \frac{\partial(\)}{r \cos\theta \lambda} ,$$

$$\frac{\partial(\)}{\partial y} = \frac{\partial \cos\theta(\)}{r \cos\theta \partial\theta} .$$

The nonlinear energy transfer spectra $N_n(K)$ can be further partitioned into two parts as

$$N_n(K) = \langle K_m \cdot K_n \rangle + \langle K_0 \cdot K_n \rangle . \quad (4.20)$$

Here $\langle K_m \cdot K_n \rangle$ is the transfer of energy into wavenumber n by interaction among different wavenumbers excluding 0, while $\langle K_0 \cdot K_n \rangle$ is the transfer of energy into wavenumber n by interaction between the mean

flow and wavenumber n .

By definition, $\langle K_m \cdot K_n \rangle$ is given as

$$\begin{aligned}
 \langle K_m \cdot K_n \rangle = & - \left[P_n(u, \frac{\partial u' u'}{\partial x}) + P_n(v, \frac{\partial u' v'}{\partial x}) \right] \\
 & - \left[P_n(u, \frac{\partial u' v'}{\partial y}) + P_n(v, \frac{\partial v' v'}{\partial y}) \right] \\
 & + \frac{\tan \theta}{r} \left[P_n(u, u' v') - P_n(v, u' u') \right] \\
 & - \left[P_n(u, \frac{\partial u' \omega'}{\partial p}) + P_n(v, \frac{\partial v' \omega'}{\partial p}) \right] . \quad (4.21)
 \end{aligned}$$

Here, the prime denotes deviation from the zonal mean.

$\langle K_o \cdot K_n \rangle$ is given explicitly by linearized equation as

$$\begin{aligned}
 \langle K_o \cdot K_n \rangle = & - \left[\frac{\partial U_o}{\partial x} P_n(u, u) + \frac{\partial V_o}{\partial x} P_n(u, v) \right] \\
 & - \left[\frac{\partial U_o}{r \partial \theta} P_n(u, v) + \frac{\partial V_o}{r \partial \theta} P_n(v, v) \right] \\
 & - \frac{\tan \theta}{r} \left[U_o P_n(u, v) - V_o P_n(u, u) \right] \\
 & - \left[\frac{\partial U_o}{\partial p} P_n(u, \omega) + \frac{\partial V_o}{\partial p} P_n(v, \omega) \right] \\
 & - \left[\frac{\partial U_o K_n}{\partial x} + \frac{\partial V_o K_n}{\partial y} + \frac{\partial \omega_o K_n}{\partial p} \right] , \quad (4.22)
 \end{aligned}$$

where the suffix o denotes zonal mean.

V. RESULTS

A. The Control Experiment

In this section, we shall analyze the Kelvin waves, the mixed Rossby-gravity wave and the equatorially trapped Rossby wave, which are detected in the control experiment.

1. Mean zonal wind

Figure 2 shows the summer and winter mean zonal wind from the model simulation. The midlatitude tropospheric jets generated by the model are well positioned in both latitude and height compared with observations (Newell et al., 1972). The intensity of the jets is reasonably close to the observations, especially the Northern summer, while the jets in the Southern Hemisphere (SH) are 5 ms^{-1} stronger than observed. A defect of the model is the weakness of the simulated tropical easterlies in both seasons. Instead of occupying the whole tropical troposphere, the tropical easterlies in the summer season are broken in the lower part of the troposphere and shift about 10° northward near the 200 mb level, while the surface easterlies and the easterlies near the tropopause compare favorably with observations. On the other hand, the tropical easterlies in the winter season disappear completely except for the weak surface easterlies simulated in agreement with observations.

According to Maruyama and Yanai (1967) and Maruyama (1967), mixed Rossby-gravity waves are generally observed when the prevailing flow is westerly, while Kelvin waves are observed in prevailing easterly

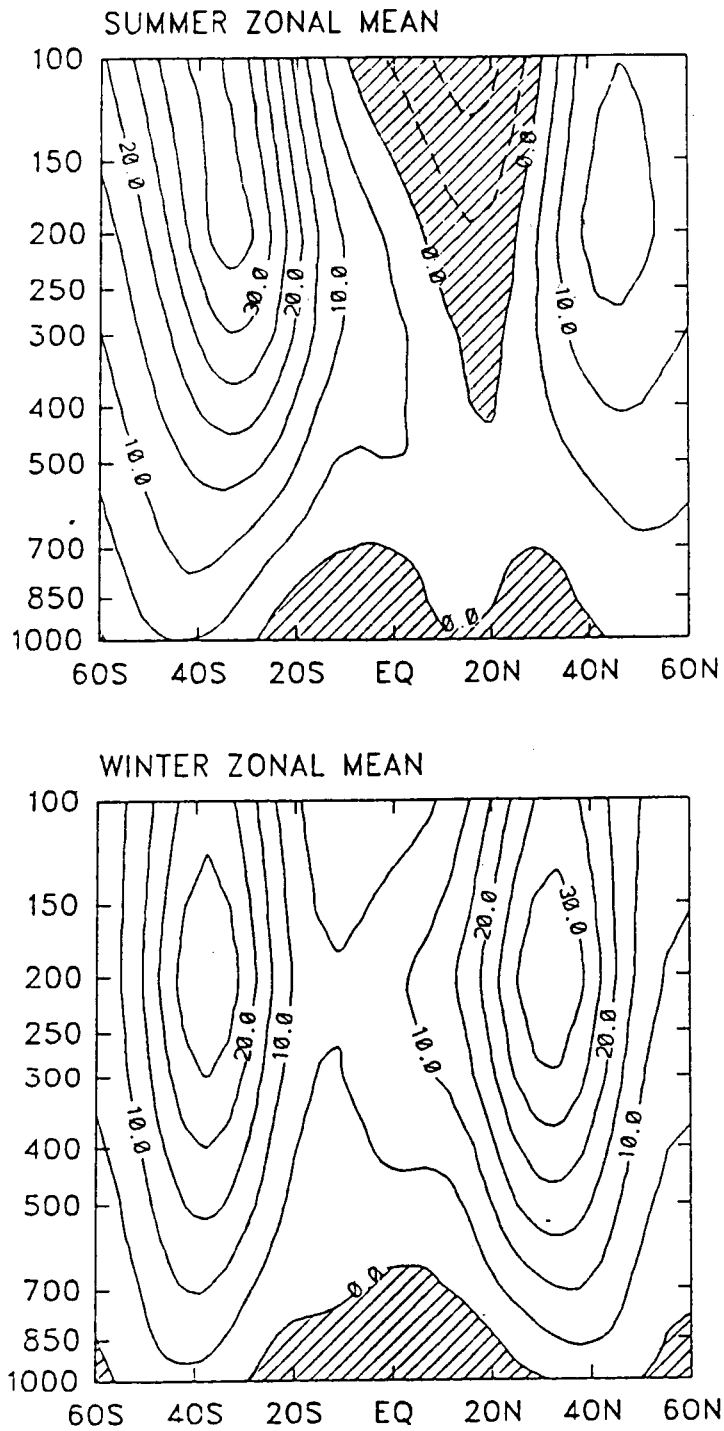


Figure 2. Time and zonally averaged zonal wind (ms^{-1}) cross sections for the control experiment. Values less than zero are hatched

flow (Wallace and Kousky, 1968; Kousky and Wallace, 1971). Thus, the weakness of the model tropical easterlies may have some influences on the simulated equatorial waves.

2. Kelvin wave in the summer season

a. Spectral analysis Figure 3a shows the distribution of the power spectral density of the geopotential height at 2N and 200 mb during summer 1977 in the wavenumber-frequency domain. The power spectra demonstrate that EMWs (Eastward Moving Waves) are more pronounced than WMWs (Westward Moving Waves). It is evident that transient wave energy is contained mainly in eastward propagating long waves. The most distinct spectral peak occurs at zonal wavenumber $m=1$ and an eastward moving period in the range of 18-25 days. Another weaker spectral peak appears at $m=2$ and eastward period 5-6 days and has an energy content about a quarter of that of the strongest peak.

Figures 3b and 3c show the power spectra of geopotential height and zonal wind for $m=1$ as a function of frequency and latitude at the 200 mb level. Distinct tropical and extratropical signals are distinguishable. The extratropical height variance in Figure 3b rapidly dominates beyond 10° latitude. Near the equator, the spectrum is dominated by an eastward propagating disturbance, which is symmetric with respect to the equator and decays away from the equator. Similar features can be also found in the spectrum of the zonal wind in Figure 2c. However, the center of the wind spectral peak is shifted southward and located at about 3S. Spectral peaks of both z and u occur at eastward periods of 18-25 days, which is

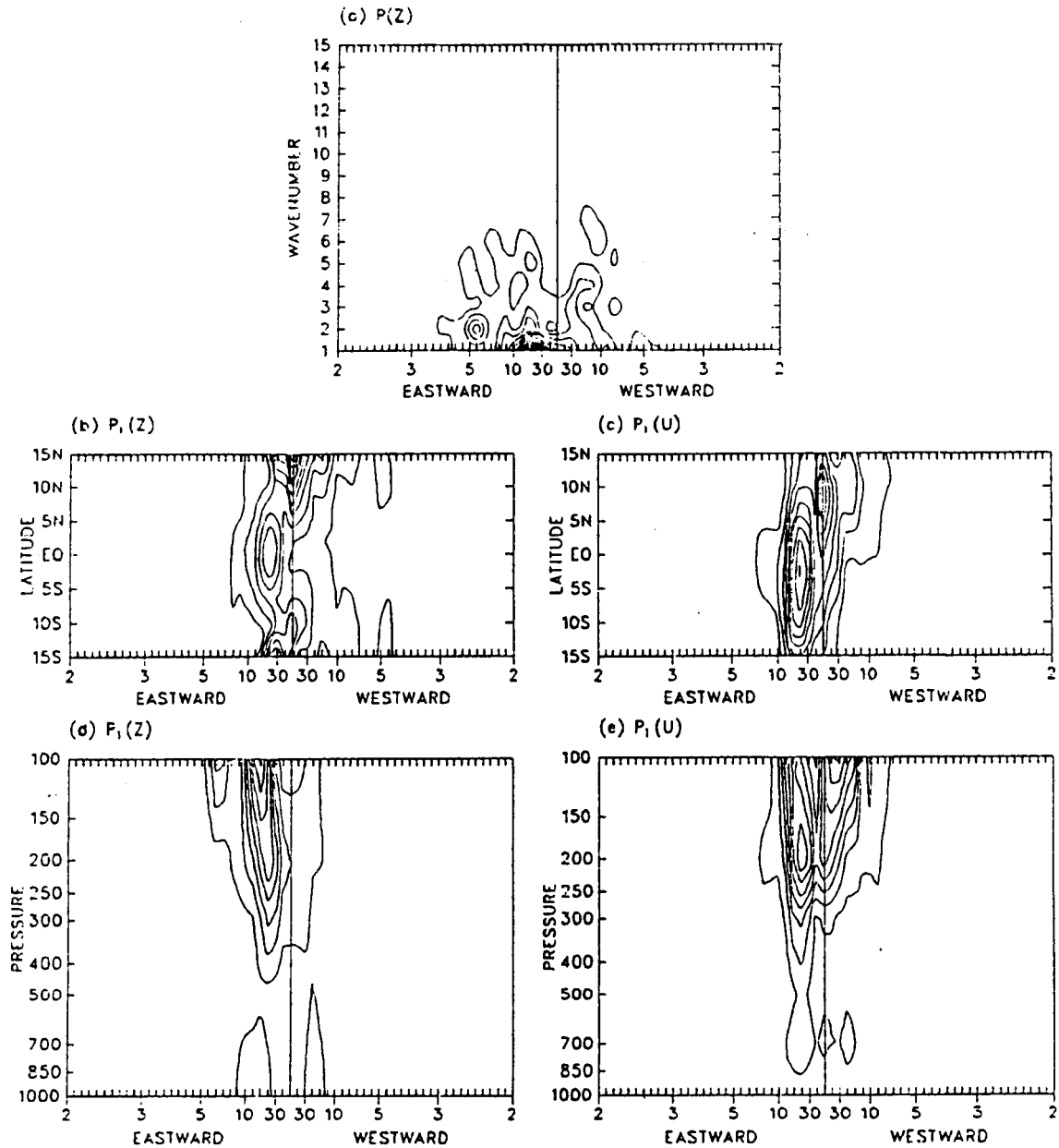


Figure 3. Power spectral analyses of (a) geopotential height (2N, 200 mb), (b) wavenumber 1 geopotential height (200 mb), (c) wavenumber 1 zonal wind (200 mb), (d) wavenumber 1 geopotential height (2N) and (e) wavenumber 1 zonal wind (2N) for the control experiment over the northern

summer. Contour intervals are 10 m^2 day in (a); 25 m^2 day in (b) and (d); and $3 \text{ m}^2 \text{ s}^{-2}$ day in (c) and (e)

consistent with the spectral peak appearing at $m=1$ in Figure 2a. The spectra of meridional wind (not shown) are dominated by westward propagating disturbances in the extratropical region, while the spectral peak of the meridional wind corresponding to those of z and u is negligible.

Figures 3d and 3e show height-frequency sections of the geopotential height and zonal wind at 2N for $m=1$. The vertically coherent structure of eastward propagating disturbances with periods corresponding to that of the spectral peak identified above is evident. Careful observation of this disturbance indicates that the period of the disturbance shifts slightly towards shorter periods with increasing height. The maximum spectral peak of the geopotential height occurs at an eastward moving period of 20 days at 400 mb and approaches 15 days at 100 mb. In contrast to the power spectrum for z , the power spectrum for u for the EMW with a period of 18-25 days attains maximum at the 200 mb level.

Features similar to those mentioned above can also be observed from the EMW associated with the spectral peak at $m=2$ and periods of 5-6 days (not shown).

All the features that have been identified above are good indications of Kelvin waves with periods of 18-25 days for $m=1$, and with periods of 5-6 days for $m=2$.

Since the two wave signals isolated from the spectral analysis have similar behavior, we shall focus only on the signal at $m=1$ and periods of 18-25 days in the following discussion.

b. Propagation characteristics Having isolated the wave signals, we are able to construct their horizontal structure as simulated by the model. Figure 4 presents the horizontal distributions of geopotential height and winds at 200 mb for $m=1$ and periods of 18-25 days. Evidently, the simulated disturbance has a horizontal structure resembling that of the atmospheric Kelvin waves depicted by Matsuno (1966), which are equatorially trapped and symmetric with respect to the equator in both pressure and zonal wind, with a negligible meridional wind component. Therefore, this disturbance is identified as a Kelvin wave with $m=1$ and periods of 18-25 days.

Given the zonal wavenumber and Doppler-shifted frequency $\hat{\omega}$, the latitudinal width Y_L and vertical wavelength L_z of the Kelvin wave may be computed as (Holton, 1979)

$$Y_L = \left| \frac{2 \hat{\omega}}{\beta m} \right|^{\frac{1}{2}}, \quad (5.1)$$

$$L_z = \frac{2 \pi \hat{\omega}}{m S^{\frac{1}{2}}}. \quad (5.2)$$

where $\beta = 2.28 \times 10^{-11} \text{ m}^{-1} \text{ s}^{-1}$, and $S = 4 \times 10^{-4} \text{ s}^{-2}$ is the square of the Brunt-Vaisala frequency. Estimated values of Y_L and L_z for the Kelvin waves are listed in Table 3. For example, the Kelvin wave with $m=1$ and period 18-25 days has a vertical wavelength of 5.9 km and a e-folding latitudinal width of 11° latitude, which is in agreement with the wave pattern shown in Figure 3.

Table 3. Characteristics of the equatorial planetary waves simulated by CCM1

Case	Season	Observed component at equator	m	n	Period (days)	Doppler-shifted phase speed (m/s)	Vertical wavelength (km)	Latitudinal width	Identification
Control	summer	z	1	-1	21	19	5.9	11°	Kelvin wave
		z	2	-1	5.5	39	12	16°	Kelvin wave
	v	5	0	13	-15	3.3	8°	mixed Rossby-gravity wave	
	winter	z	1	-1	17	20	6.3	12°	Kelvin wave
		z	3	1	24	-16	14	15° ^a	equatorially trapped Rossby wave
No-mountain	summer	z	1	-1	17	22	7	13°	Kelvin wave
	winter	z	1	-1	21	19	5.9	11°	Kelvin wave
No-cloud	winter	u	1	1	12	36	11	16°	Kelvin wave
		u	1	3	20	-28			free Rossby wave

^a The latitude of the maximum in pressure.

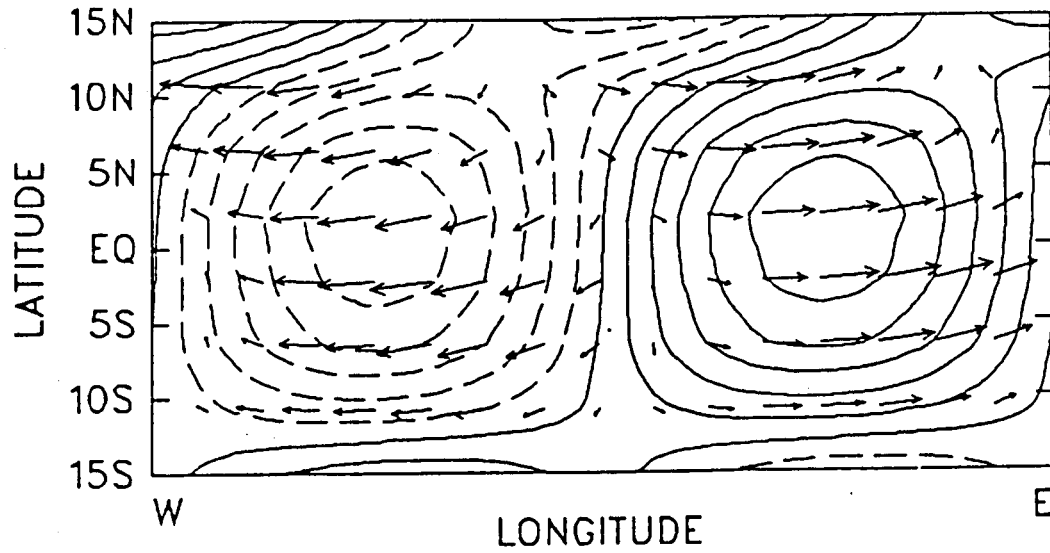
KELVIN WAVE ($m=1$) JUNE 28

Figure 4. Horizontal distributions of geopotential height and horizontal winds at 200 mb for Kelvin wave with $m=1$ and periods of 18-25 days in the control experiment over the northern summer. Contour interval is 1.5 m. Maximum wind at the equator is about 5 ms^{-1}

Zangvil and Yanai (1980) and Yanai and Lu (1983) presented spectral studies of 200 mb level winds in the latitude belt 25S-45N for June-August 1967 and June-August 1972. They found Kelvin waves at $m=1$ with periods of 30 days and 7 days, and $m=2$ with periods of 7 days in the summer 1967. However, the wave signals in the summer 1972 are much weaker than those in the summer 1967 and only Kelvin waves at $m=1$ with periods longer than 20 days and $m=2$ with periods near 15 days were observed. The great difference in equatorial wave activity in the two years is considered to be due to the interannual variation of the tropical general circulation during these two years. The year 1967 had near normal monsoonal rainfall, while 1972 was a well-known drought and El Nino year. It was pointed out by Arkin (1982) that the tropical easterly jet is weaker and farther south in the summer of the year when the anomalously warm sea surface water associated with the Southern Oscillation appears over the equatorial Pacific (Warm Event). Chen and van Loon (1987) further pointed out that the tropical divergent circulations, i.e., the east-west Walker and local Hadley circulations, during such summers are weakened and shifted eastward and that the changes in the tropical divergent circulations may cause a change in the energetic maintenance of the tropical easterly jet. Therefore, the change of wave activity between the two years suggests that the selection of the equatorial waves is related to global-scale forcing in the tropics.

Yanai and Lu (1983) also calculated the equivalent depth and latitudinal width of the Kelvin wave which they had identified from

the observations. Comparing with their results, we find the Kelvin wave simulated by the CCM1 agree well with the observed ones as far as the horizontal and vertical structures of the waves are concerned. The simulated Kelvin waves are all confined within 16° latitude and have vertical wavelength less than 12 km, which suggests that these waves are generated in the upper troposphere instead of being free modes such as those proposed by Matsuno (1966). In general, the observed Kelvin waves above the tropopause have larger vertical wavelengths than those of the upper tropospheric Kelvin waves (Wallace and Kousky, 1968; Hirota, 1978, 1979). Salby and Garcia (1987) demonstrated that Kelvin waves with shorter periods in the equatorial atmosphere become relatively more important at upper levels since shorter periods are associated with larger vertical wavelengths and group velocities, and are less subject to radiative damping. Therefore, it is not surprising to have Kelvin waves with smaller vertical wavelengths and longer periods in the upper troposphere.

Because of the distinct spectral character of the Kelvin wave signals it is possible to construct height-time cross sections for the time evolution of the Kelvin wave by band-filtering the eastward propagating features. Vertical structures of geopotential height and zonal velocity for $m=1$ with periods of 18-25 days at 2N are shown in Figure 5. The oscillations of both z and u are clearly detectable and the vertical structures show a vertical phase change at the 500 mb level, which differs markedly from the structure of midlatitude systems characterized by strong baroclinicity. In the tropical

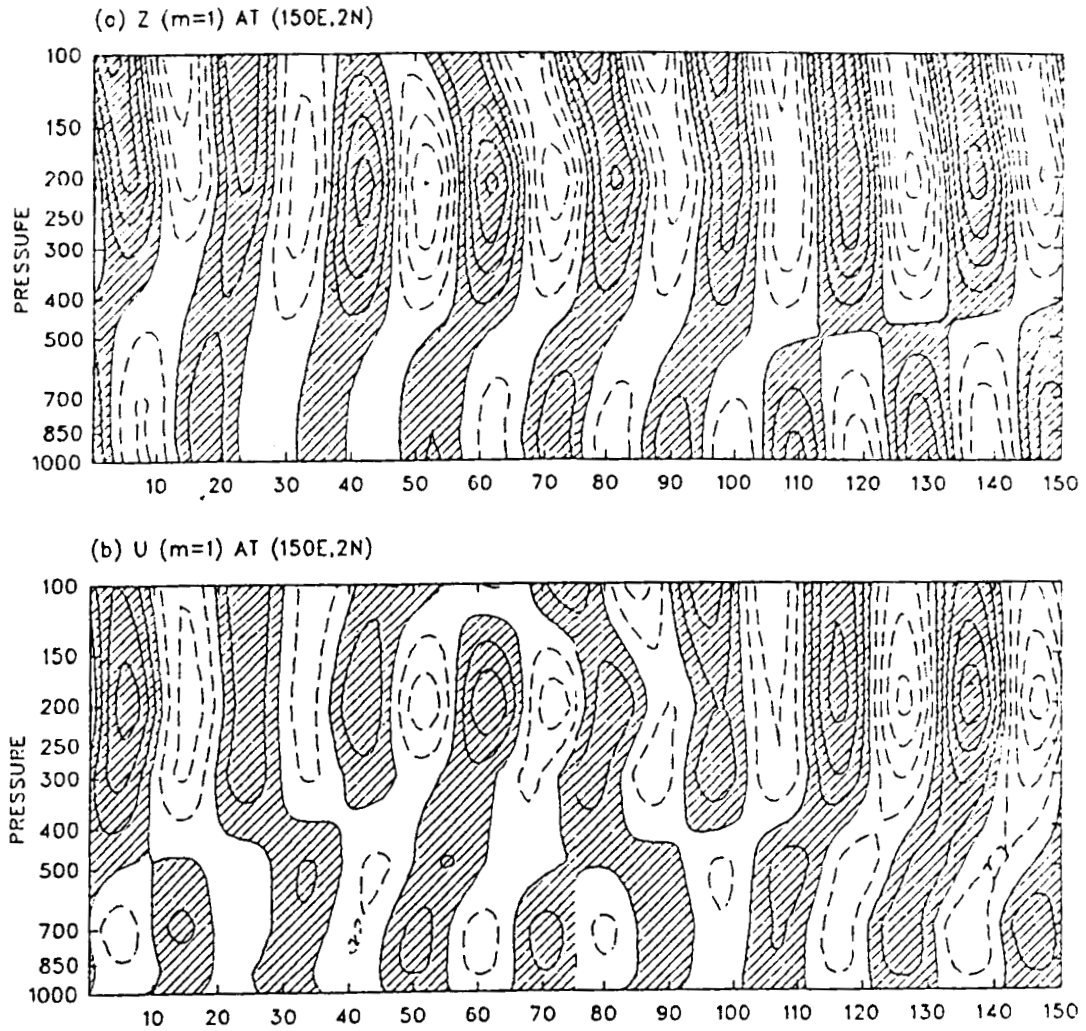


Figure 5. Height-time cross sections of geopotential height (a) and zonal wind (b) associated with $m=1$ and eastward moving periods of 18-25 days for the control experiment over the northern summer. Contour intervals are 2 m in (a), and 1 ms^{-1} in (b)

precipitation zone, convergence is not limited to low-level frictional inflow in the planetary boundary layer, but extends up to nearly 400 mb level which is the height where the hot towers achieve their maximum buoyancy, while divergence attains its maximum at the 200 mb level. These features are clearly shown in Figures 5a and 5b. The disturbance has little phase tilt but a phase change somewhere between the 400 mb and 500 mb over the entire sampling period. The maximum disturbance appears near 200 mb, where the maximum divergence occurs, implying the location of a possible energy source for Kelvin waves.

There are two episodes of Kelvin wave disturbances during the sampling period. In the first episode, which covers days 30 to 80, the vertical structure of the disturbance is barotropic with a maximum amplitude of about 4 m at the 200 mb level. As time increases, a vertical phase shift appears near 400 mb while the amplitude increases to 8 m and the height disturbance extends up to the lower stratosphere with a slight phase tilt above 200 mb. On the other hand, the zonal wind component attains its maximum amplitude at 200 mb at the beginning of the episode and then the disturbance propagates downward.

The second episode occurs during days 105-150. The disturbance of the geopotential height in this episode has a vertical phase change near the 500 mb level, which suggests that strong cumulus convection in the tropics occurs during this period. The amplitudes of z and u are about 8 m and 4 ms^{-1} , respectively. The fluctuations can be traced all the way up to the lower stratosphere. In the discussion of Figure 5, we also noted that the oscillations of the geopotential

height and the zonal wind are in phase.

c. Precipitation and forcing inference Although the structure of Kelvin waves is now quite well understood, the nature of the tropospheric source for those waves is still somewhat uncertain. A number of possible tropospheric sources might be responsible for generating the observed waves. For example, geostrophic adjustment processes, nonlinear interaction among tropical tropospheric disturbances and forcing from middle latitudes all might play a role. However, the most likely energy source appears to be in-situ cumulus convection organized by synoptic-scale disturbances in the equatorial region.

According to the satellite observations of cloud coverage compiled by Sadler (1970) and the satellite infrared effective temperature analyzed by Liebman and Hartmann (1981), intense convection is associated with the intertropical convergence zone (ITCZ), South Pacific Convergence Zone (SPCZ), and the three tropical continents. The three regions are Central America and the northern part of South America, equatorial west Africa, and the monsoonal areas during the northern summer. Chen (1985) pointed out that the stationary divergent modes, mainly the local Hadley and Walker circulations, are responsible for the local maintenance of the high water vapor content over these tropical areas. Thus a high precipitation rate must exist over these areas due to the intense convection supported by the high water vapor content.

Figures 6a and 6b present the model's mean-daily distribution of

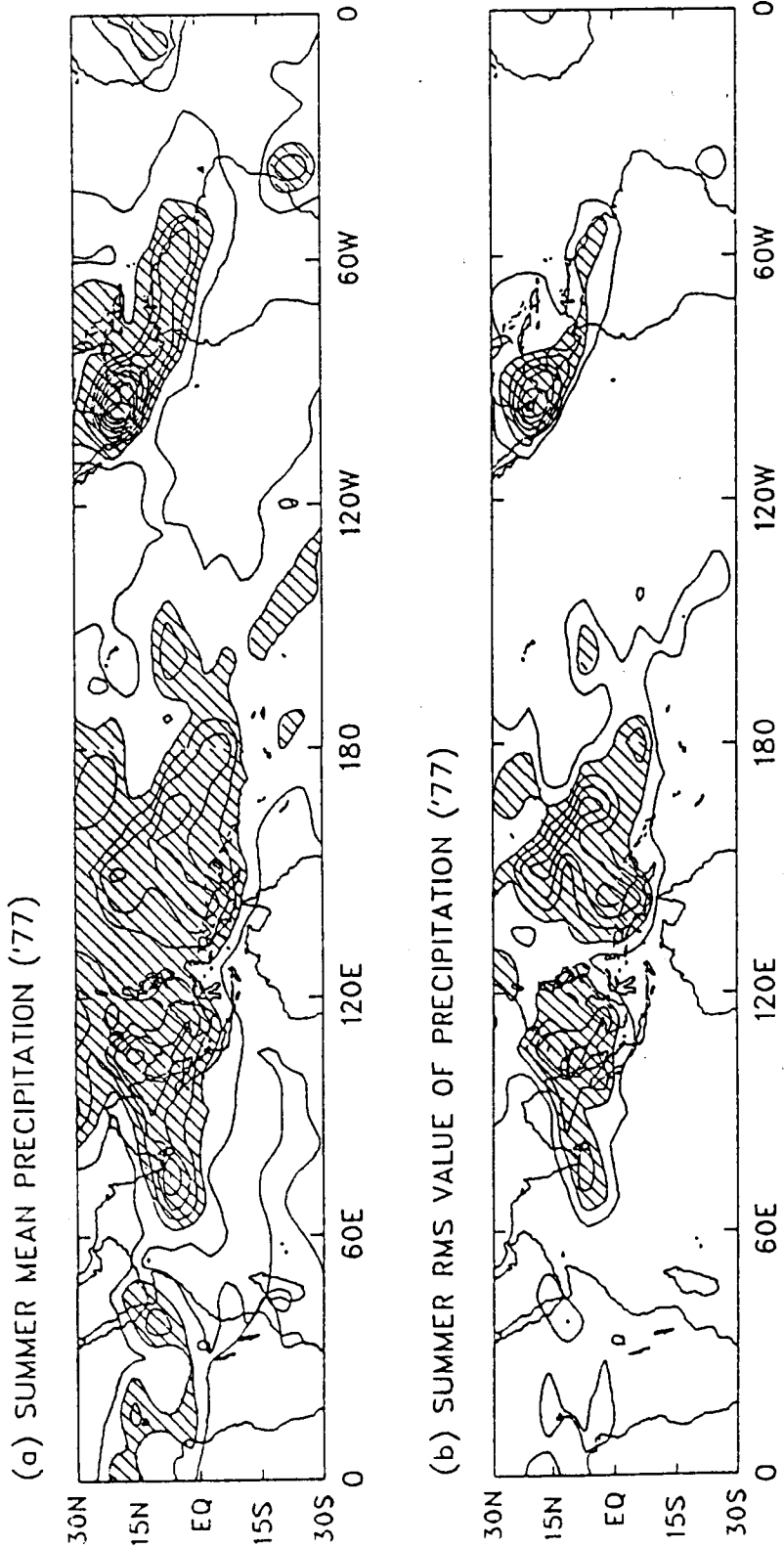
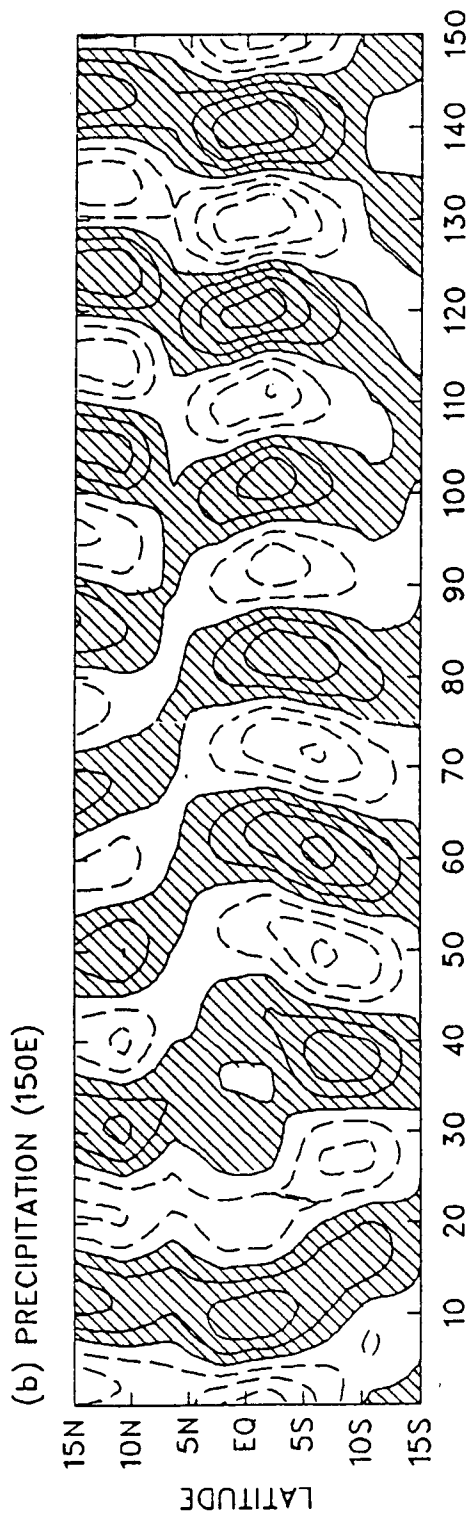
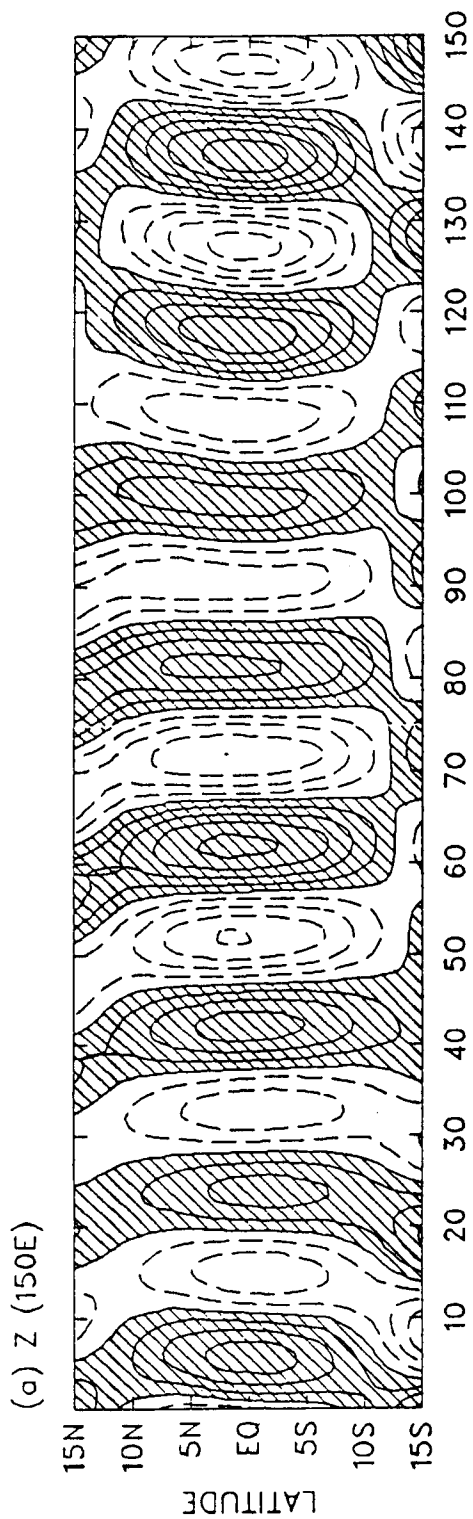


Figure 6. Northern summer mean of precipitation rate and root mean square of the precipitation for the control experiment. (a) Summer mean precipitation rate and (b) root mean square of the precipitation rate. Contour intervals are 2.5 mm day⁻¹ in (a), and 150 mm² day⁻² in (b). Values greater than 5 in (a) and 300 in (b) are hatched

Figure 7. Latitude-time cross sections of (a) geopotential height for $m=1$ at 200 mb and (b) precipitation rate for $m=1-15$ with eastward moving periods of 18-25 days for the control experiment in summer. Contour intervals are 2 m in (a), and 3 mm day^{-1} in (b). Values greater than zero are hatched



precipitation and the root mean square of precipitation in the summer 1977. Although the precipitation rate in the model (Figure 6a) generally tends to be somewhat larger than observed (i.e., Pitcher et al. 1983), the model successfully produces the general features of precipitation found in observations, except for the precipitation deficit over the equatorial Africa. For example, the intense equatorial rain belts, including an elongated maximum over India and the western Pacific in accordance with the Asian monsoon circulation, and a tongue of rainfall in the Central America, extending from the northeast Pacific to the north part of Central America, are reproduced in the model. It is evident that the daily rainfall fluctuates substantially over the three maximum precipitation centers (Figure 6b).

Figure 7a shows the latitude-time cross section of the 200 mb geopotential height for the Kelvin wave and the precipitation disturbances with periods of the Kelvin wave. The time evolution of the Kelvin wave associated with $m=1$ and periods of 18-25 day at 150E longitude can be seen clearly in Figure 7a. It is evident that the wave is confined within an equatorial belt between 10S to 10N during the entire sample period. The two episodes of the Kelvin wave, which were identified before, can also be observed.

As pointed out by Holton (1972), there is no convincing evidence to show that the field of diabatic heating in the tropical troposphere has a spectral peak at the frequency where Kelvin waves are observed. The spectral analysis of the model's precipitation rate (not shown)

gives a stochastic distribution in the wavenumber-frequency domain. Based on this argument, Figure 7b shows the precipitation perturbation associated with $m=1-15$ and eastward periods of 18-25 days. The interesting feature of the rainfall disturbance is the northward migration of its maximum center. For example, at day 26, the maximum center is located near 10S. As time progresses, it continuously moves northward until it approaches the equator at day 105. Recalling the vertical structures of the Kelvin wave shown in Figure 5, we find that the vertical phase change of the geopotential height after day 105 coincides with the precipitation disturbance near the equator. This finding strongly suggests that the atmosphere is more sensitive to forcing in the frequency band of Kelvin waves.

In order to understand the possible sources of excitation for wave disturbances in the tropics, Holton (1972, 1973) and Murakami (1972) studied the atmospheric response to prescribed tropospheric heat sources in linearized primitive equation models. Holton (1972) simulated the atmospheric response to the latent heat released in the ITCZ. In any linearized model, the atmospheric response to forcing in one hemisphere is equivalent to the sum of the responses that are symmetric and antisymmetric with respect to the equator. Therefore, Holton studied the atmospheric responses of symmetric and antisymmetric heating separately. He concluded that a heating oscillation which is symmetric about the equator will generate eastward moving Kelvin wave and the frequencies of the Kelvin waves are determined by the natural bandpass selectivity of the atmosphere

combined with a red noise forcing spectrum in time or space.

On the other hand, Murakami (1972) simulated a quite realistic Kelvin wave as the response to an eastward moving heat source with $m=1-2$ and a period of about 16 days at the latitude of the monsoon region (20N). This specification of heat source is partly supported by observational evidence, which shows that during the monsoon season the rainfall fluctuates substantially at that latitude with periods longer than 10 days, and a major portion of zonal rainfall asymmetry is presumably carried by wavenumbers 1 and 2.

As revealed in Figure 7, it does not matter whether the eastward propagating heat source is located south of the equator or straddles the equator; the Kelvin wave is observed in both cases. This finding is in agreement with both Holton's and Murakami's results.

An attempt was next made to determine the effect of a zonally asymmetric heat source on the generation of Kelvin waves. Figure 8 shows the amplitude of the Kelvin wave in geopotential height at 200 mb and the precipitation rate with $m=1-15$ and the period of the Kelvin wave at (90W, 2N), (105E, 2N) and (150E, 2N), respectively. The solid lines indicate geopotential height and the dashed lines precipitation rate. The Kelvin wave disturbance and precipitation in the eastern equatorial Pacific (90W, 2N) or in eastern Indian Ocean (105E, 2N) show little correlation. However, the two fields show a high correlation in the western Pacific Ocean (150E, 2N).

We also noted that there is a time lag between the geopotential height and precipitation oscillations at a given location. This time

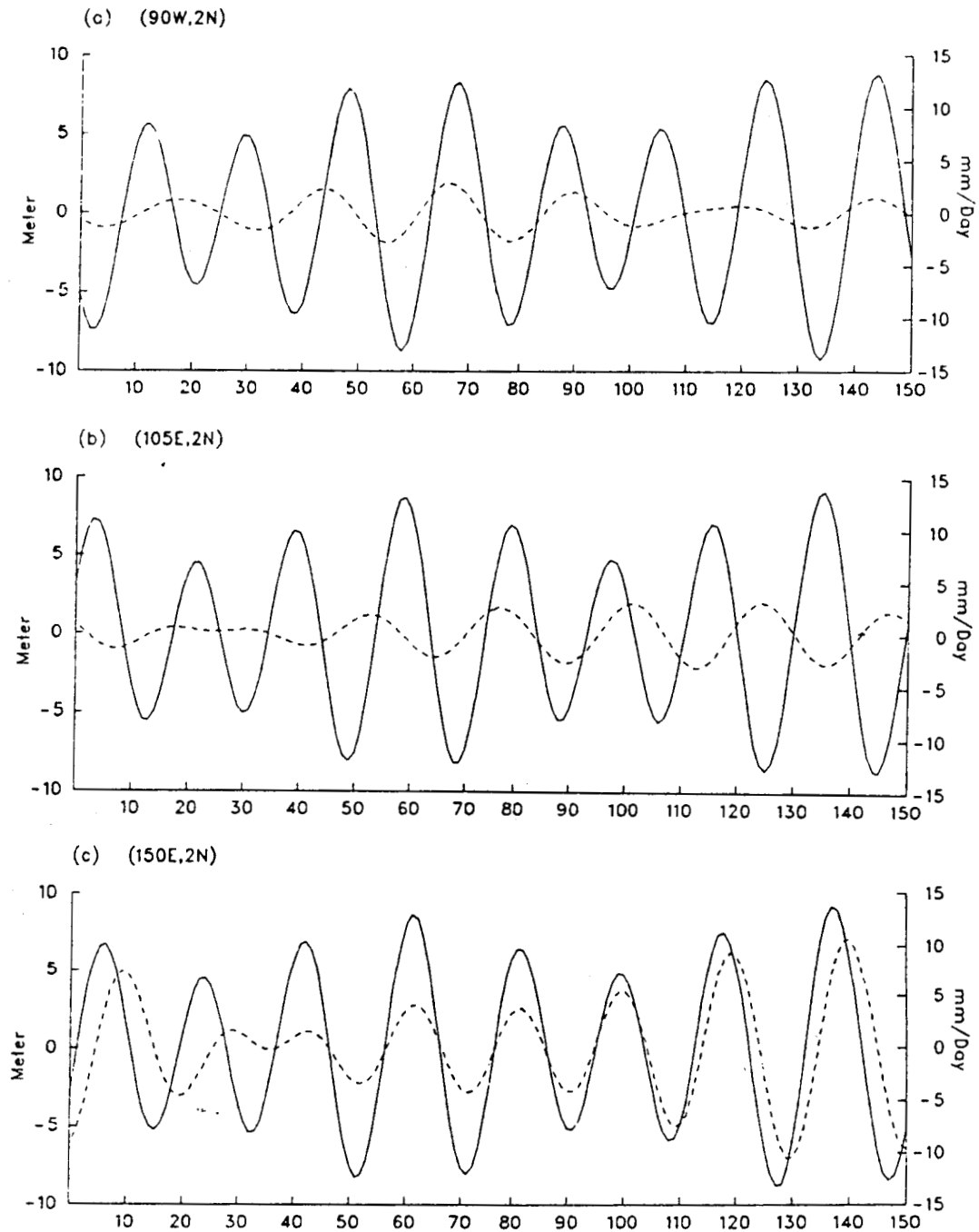


Figure 8. Time series of amplitudes of geopotential height for $m=1$ at 200 mb (solid lines) and precipitation rate for $m=1-15$ (dashed lines) with eastward moving periods of 18-25 days at (a) (90W, 2N), (b) (105E, 2N) and (c) (150E, 2N) for the control experiment over the northern summer

lag simply implies an eastward tilt of the wave structure with increasing height. From theoretical considerations, the axes of maximum upward motion and maximum zonal wind must be in phase in order to satisfy the continuity equation. Consequently, precipitation caused by vertical motion is also in phase with zonal wind oscillations. On the other hand, since the zonal wind component is geostrophically balanced by the meridional pressure gradient, it is expected that the maximum zonal winds and maximum pressure should coincide. Thus, at a given longitude, the pressure oscillation at upper levels will lead the lower level precipitation oscillation as long as the vertical structure of the Kelvin wave tilts eastward. Therefore, Figure 8 strongly suggests that the maritime region of Indonesia in the western Pacific may be a possible region where Kelvin waves originate.

d. Maintenance of the Kelvin wave Since the data output from CCM1 is interpolated to conventional meteorological levels, the maintenance of a particular wave disturbance can be gained by computing every term in the kinetic energy equation (4.17), which is proposed by Hayashi (1980), in the wavenumber-frequency domain. In general, the meridional wave energy flux due to the pressure work and the poleward momentum transport, which is included in the nonlinear term, have maxima at 200 mb, simply because this level has the maximum kinetic energy content of wave motion.

The first term on the right-hand side of the equation (4.17) represents transfer of kinetic energy from or to wavenumber n through

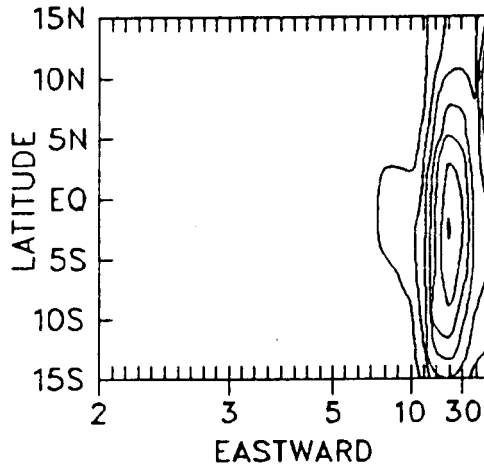
nonlinear dynamic interaction. The second term represents the conversion of eddy available potential energy to eddy kinetic energy. The third and fourth terms represent the meridional and vertical convergence of the potential energy flux associated with wave disturbances.

Figure 9 presents the energetic budget analysis of equation (4.17) as a function of latitude and frequency for $m=1$. It reveals that the kinetic energy (Figure 9a) associated with the Kelvin wave with a centered period of 20 days is dominant. However, the latitudinal structure of the kinetic energy is not symmetric with respect to the equator. The maximum kinetic energy is located at 2S. It suggests that the asymmetry of the basic zonal flow (Figure 2) may be responsible for the asymmetric distribution of Kelvin-wave kinetic energy.

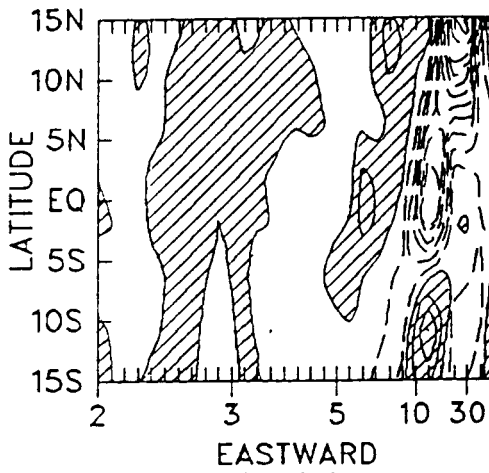
The conversion of eddy available potential energy to eddy kinetic energy is shown in Figure 9b. Two significant energy conversion peaks appear near 12-day and 6-day periods. It is seen that a positive energy conversion with a period about 12 days is located south of 5S and a negative energy conversion with the same period appears north of 5S. Using station data of upper air observation over the Marshall Islands area (165E, 5N) from April 15 to July 31, 1956, Nitta (1970) computed the vertical distribution of conversion of available potential energy into kinetic energy and found that a large energy conversion from eddy available potential energy to eddy kinetic energy is concentrated in two period ranges centered at 12 days and 5 days

Figure 9. Various energy conversions ($m=1$, eastward moving periods) at 200 mb for the control experiment over the northern summer: (a) K_1 , (b) $-P_1(\alpha, \omega)$, (c) $-\frac{\partial P_1(\phi, \omega)}{\partial p}$, (d) $-\frac{\partial P_1(\phi, v)}{\partial y}$, and (e) $N_1(k)$. Contour intervals are 2 J in (a); 0.5×10^{-5} W in (b), (c) and (e); and 10^{-5} W in (d). Values greater than zero are hatched

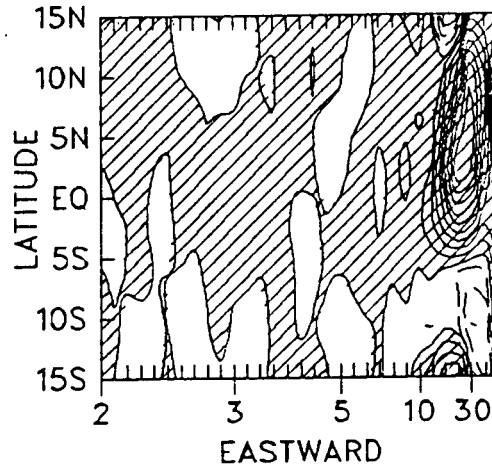
(a) $(u_1^2 + v_1^2)/2$



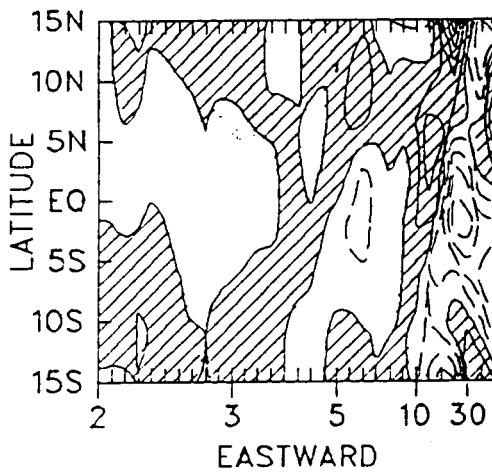
(b) $-P_1(\alpha, \omega)$



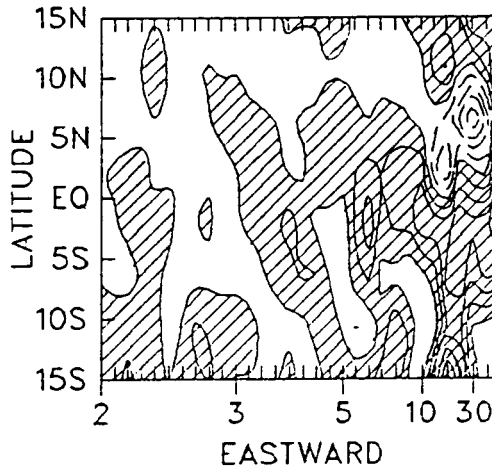
(c) $-\partial P_1(\omega, \Phi)/\partial P$



(d) $-\partial P_1(\gamma, \Phi)/\partial \gamma$



(e) $N_1(K)$



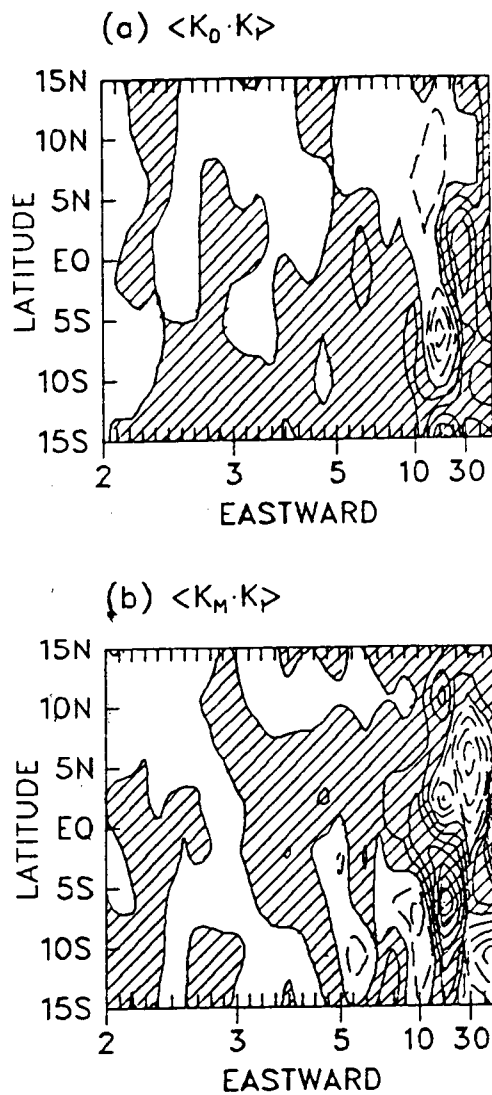


Figure 10. Nonlinear energy conversions ($m=1$, eastward moving periods) at 200 mb for the control experiment over the northern summer: (a) wave-mean flow interaction and (b) wave-wave interaction. Contour intervals are 0.5×10^{-5}

W

with the maximum energy conversion being located at the levels between 400 mb and 200 mb. Thus, he suggested that the conversion of available potential energy is the most important one for the maintenance of large-scale disturbances in the tropics. However, Nitta's argument does not seem to be the case for the Kelvin wave since the period of latter is longer than that of Nitta's waves.

Figure 9c shows the vertical convergence of potential energy flux. It is evident that the eastward component of this quantity is positive (convergence) for almost the entire period at this level. The maximum convergence occurs at 2N with a period range centered at 20 days, which coincides with the period of the Kelvin wave. Hayashi et al. (1984) showed that the eastward moving component of the vertical potential energy flux transports upward above 7km while below that level it transports downward. The reversal of the direction of energy flux at 7 km suggests that the wave energy source exists near this level. In Figure 9c, the most distinct convergence of potential energy flux appears north of the equator. From the discussion in the previous section, we can infer that the local divergent circulations, which are generated by deep penetrative convections in the tropics, are responsible for this vertical energy transport. Thus, cumulus convection in the tropics is important for the maintenance of the Kelvin wave.

Figure 9d shows the meridional convergence of energy flux. The negative area between 8S to 5N with periods 15-30 days indicates divergence of the meridional energy transport, while the positive area

poleward of the negative area implies convergence of the meridional energy flux. This result confirms the finding obtained by Yanai and Lu (1983), i.e., that there is a meridional divergence of energy flux associated with the Kelvin wave. From Figures 9c and 9d we may conclude that the energy source at the 200 mb level is primarily the convergence of vertical energy transport to the north of the equator. The net energy input is then transported away from the equator to maintain the Kelvin wave.

In order to understand the basic dynamics of equatorial waves, most of the previous studies of this subject were based upon the linear system. Since real atmospheric motions are not linear, it is of interest to see the importance of nonlinear interaction in the wave maintenance. Figure 9e shows the transfer of kinetic energy into EMWs with $m=1$ through nonlinear interaction. It is seen that the EMW associated with $m=1$ and periods of 12-30 days gains kinetic energy through nonlinear processes in the SH, while the wave loses kinetic energy in the Northern Hemisphere (NH) between the equator and 10N.

The nonlinear energy transfer can be further partitioned into wave-mean flow and wave-wave interactions, which are shown in Figures 10a and 10b, respectively. The transfer of kinetic energy through the wave-mean flow interaction is significant for those EMWs with periods longer than 12 days. It is evident that EMWs with periods longer than 18 days, in which the Kelvin wave is observed, gain kinetic energy from zonal flow within a latitudinal belt between 5S to 5N (Figure 10a) and loses kinetic energy in the NH through the wave-wave

interaction (Figure 10b). In addition, the EMW with a period of 15 days gains kinetic energy in the SH through the wave-wave interaction and then transfer the energy into zonal flow through the wave-mean flow interaction.

3. Kelvin wave in the winter season

In this section we shall briefly discuss the characteristics of the Kelvin wave simulated by the model in the winter season with emphasis on the differences between the Kelvin waves in the summer and those in the winter.

a. Spectral analysis The power spectrum of z at 2S and 200 mb is shown in Figure 11a as a function of wavenumber and frequency. It is evident that the power spectrum of z for EMWs has a spectral peak at $m=1$ and periods of about 15-20 days. A weak spectral peak associated with WMs occurs at $m=3$ and periods of 20-30 days. This signal is later identified as an equatorial trapped Rossby wave.

Figures 11b and 11c show the meridional structures of both z and u with $m=1$. In Figure 11b, both WMW and EMW are dominant in the extratropical area. A weak spectral peak is confined in the tropics between 8S-5N with eastward periods of 15-20 days. This spectral peak corresponds to the one at $m=1$ and periods of 15-20 days in Figure 11a. The power spectrum of u with $m=1$ (Figure 11b) has larger power concentrated in the low frequency part of the spectrum, while appreciable power of EMWs appears near the equator with periods of 15-20 days.

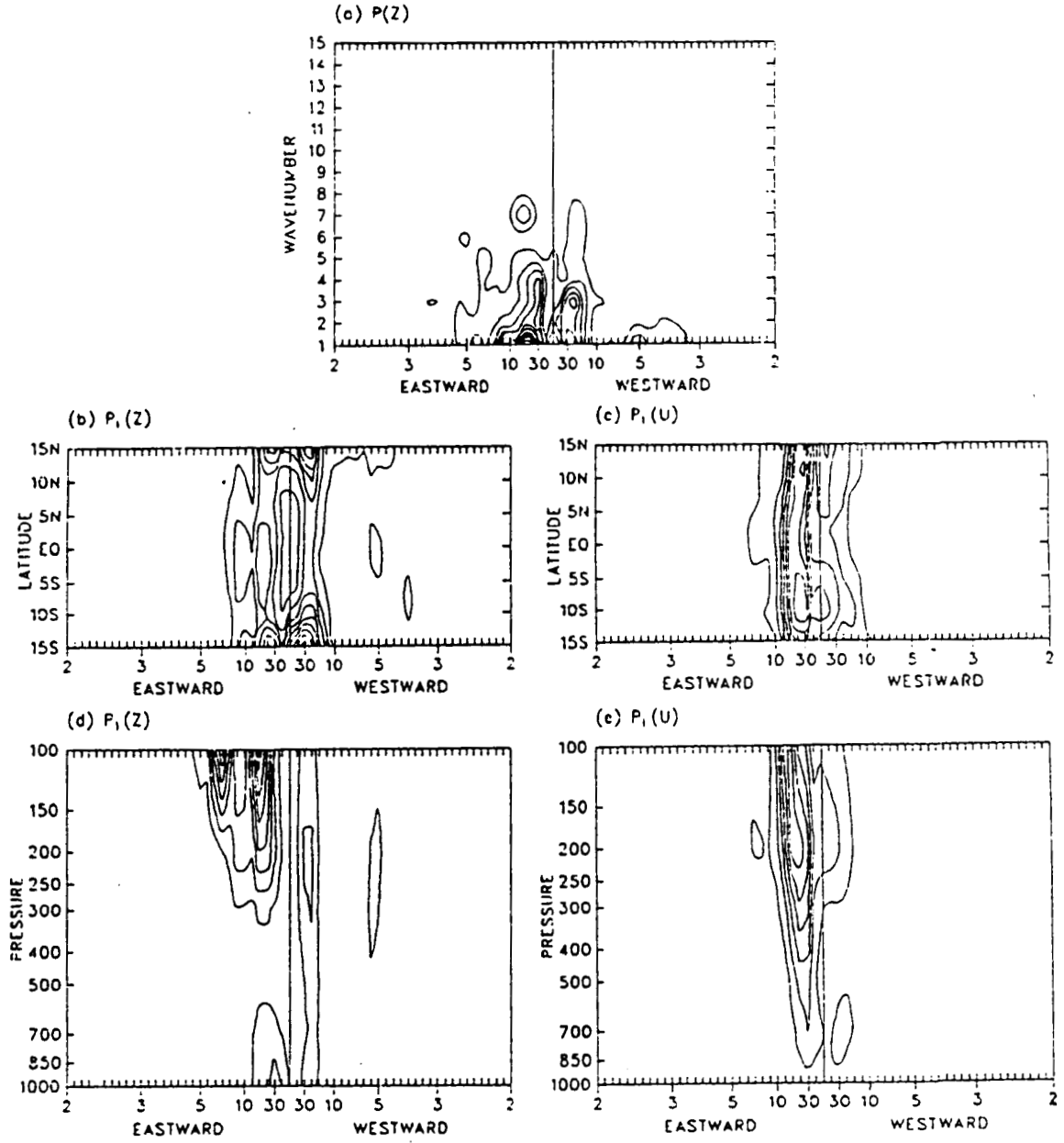


Figure 11. Same as Figure 3, except for the northern winter

ORIGINAL PAGE IS
OF POOR QUALITY

Figures 5d and 5e show the vertical structures of $P(z)$ and $P(u)$ associated with $m=1$ at 2S. Both eastward variances of z and u are significant at the period range of 15-20 days. Appreciable powers are evident from 300 mb up to 100 mb and from 850 mb up to 100 mb in Figures 11d and 11e, respectively.

b. Propagation characteristics The power spectrum of wavenumber 1 exhibits distinct spectral features corresponding to eastward propagation with periods of 15-20 days, consistently over a band of tropical latitudes and several pressure levels. Figure 12 shows that the disturbance at 200 mb has a horizontal structure strongly resembling that of atmospheric Kelvin waves. From linear wave theory, the vertical wavelength and latitudinal width of the wave are estimated to be 6.3 km and 12° latitude, respectively (Table 3). Comparing with the Kelvin wave in the summer season, we find the propagation characteristics of the Kelvin waves in both seasons are essentially the same, except for the difference in periods associated with the waves, which might be due to the seasonal change of the heating field organized by large-scale motions.

Tsay (1974) examined the characteristics of the equatorial waves identified in a perpetual January run with NCAR global circulation model. The Kelvin waves simulated by the model were found at $m=1$ with an eastward traveling period of about 24 days and $m=2$ with an eastward period of about 12 days. The vertical wavelength and latitudinal width of the Kelvin wave with $m=1$ were 8 km and 14° latitude, which agreed reasonably well with those of observed waves (Wallace and

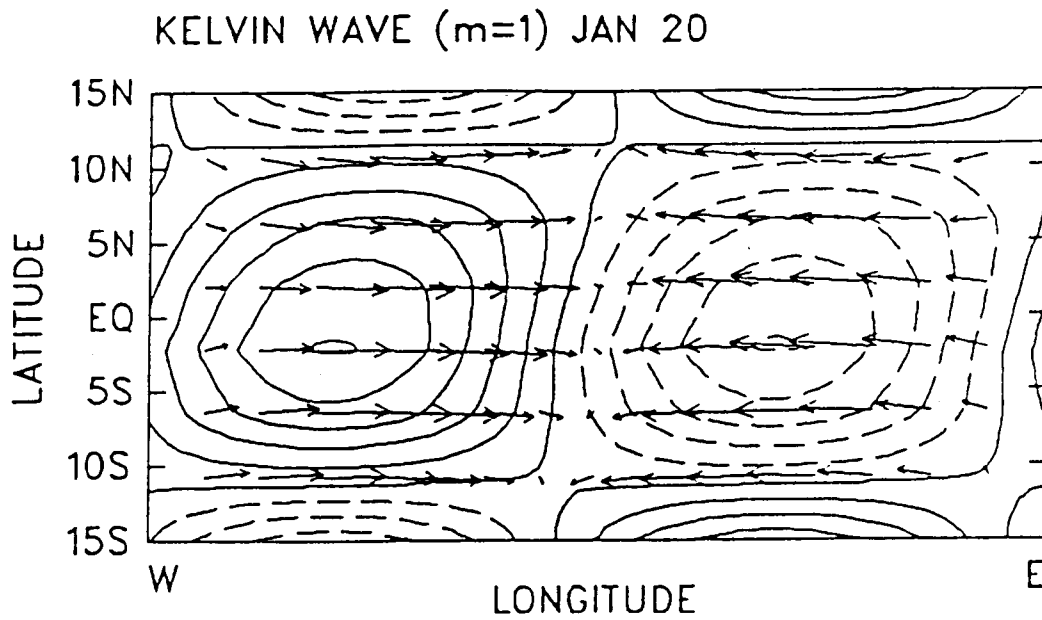


Figure 12. Same as Figure 4, except for the Kelvin wave with $m=1$ and periods of 15-20 days over the northern winter

Kousky, 1968; Kousky and Wallace, 1971). However, the observed oscillation with $m=1$ has a significantly shorter period (15 days). Furthermore, no response at wavenumber 2 at one-half the wavenumber 1 period was detected in the observations. On the other hand, the Kelvin wave simulated by the CCMI is even closer to the observed wave, comparing to Tsay's study, as far as the latitudinal width, period and vertical wavelength are concerned.

The forcing of the Kelvin wave in the winter season can be inferred from Figures A1-A4.

c. Maintenance of the Kelvin wave Figure 13 shows the maintenance of the Kelvin wave at 200 mb in the winter season. The most distinct feature is that the conversion of available potential energy into kinetic energy plays an important role in maintaining Kelvin wave (Figure 13b). The maximum conversion occurs at periods of about 15-20 days and near 3S, while the convergence of the vertical energy flux exhibits less importance in the wave maintenance (Figure 13c). This result agrees with the conclusion obtained by Manabe et al. (1970) that the conversion of available potential energy generated by the heat of condensation is most important for the maintenance of large-scale disturbances in the tropics.

The meridional wave energy flux associated with the Kelvin wave is characterized by convergence in the SH and divergence in the NH (Figure 13d). The former probably results from the conversion of available potential energy into kinetic energy near 3S. This outcome is contrary to the conclusion obtained by Tsay (1974) who found that

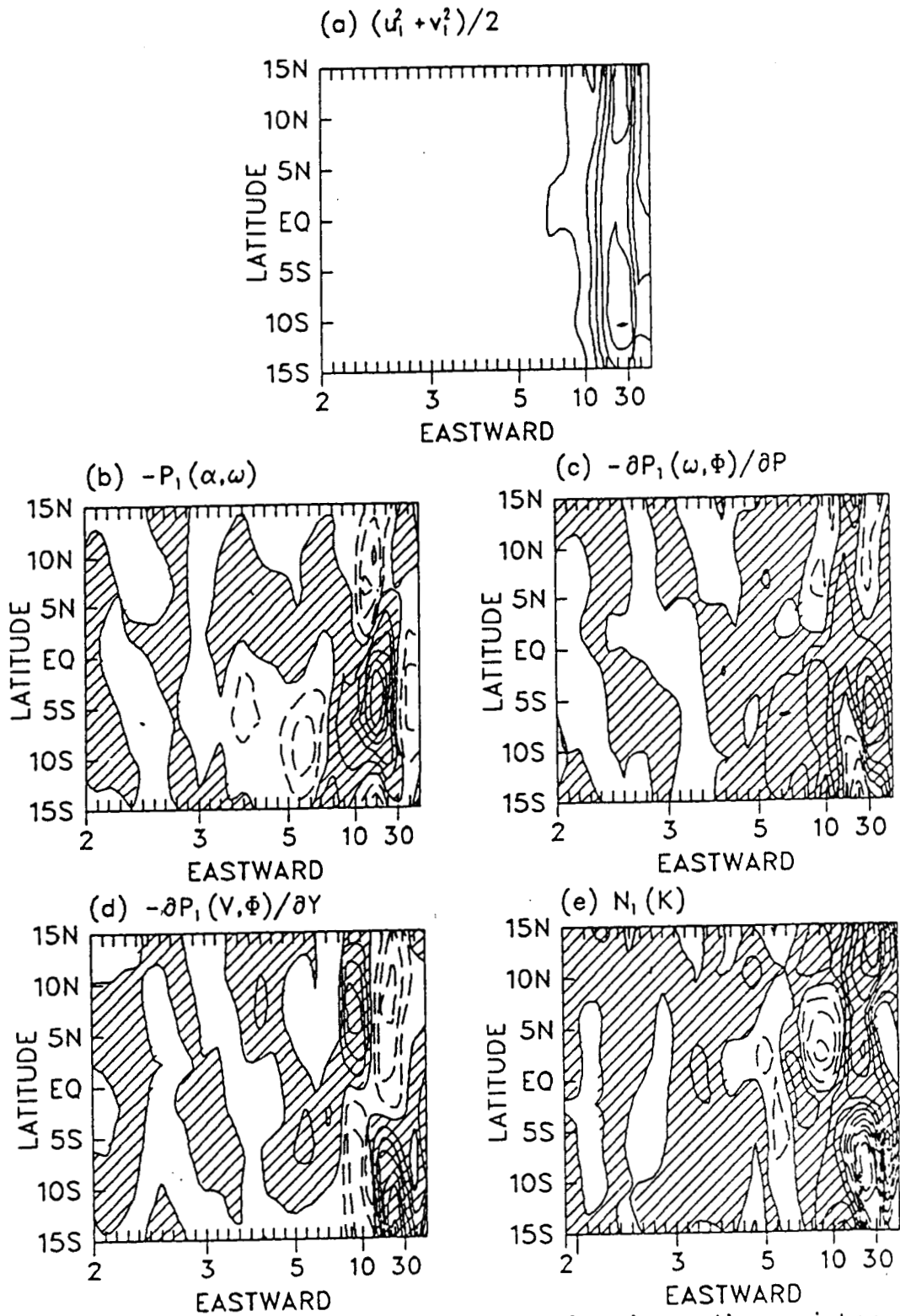


Figure 13. Same as Figure 9, except for the northern winter

the energy source of Kelvin wave in the layer 12-18 km is due primarily to convergence of equatorward energy transport.

Nonlinear kinetic energy transfer associated with EMWs at $m=1$ is shown in Figure 11e. It is evident that a large energy transfer takes place in the period range of 12-30 days, in which the Kelvin wave is observed. In contrast to the summer case, there is positive energy transfer in the NH and negative energy transfer in the SH.

We have seen that the maintenance of the Kelvin wave in the winter is somewhat different from that in the summer. The difference might be caused by the seasonal change in the heating field and the mean zonal wind distribution. The former may alter the global divergent circulation and the latter affects the wave-mean flow interaction.

4. Mixed Rossby-gravity wave in the summer season

a. Spectral analysis The spectrum of the meridional wind component at 2N and 200 mb as a function of wavenumber and frequency is shown in Figure 14a. There are several spectral peaks at $m=5$, among which the most distinct spectral peak is associated with westward moving periods of 12-15 days and characterized by a unique spectral peak in the zonal wind component at the equator (Figure 3a). Shown in Figures 14b and 14c are the latitudinal distributions of $P(z)$ and $P(v)$ associated with $m=5$. $P(z)$ is dominated by both EMWs and WMWs in extratropical area, while the WMWs at periods of 12-30 days show a very clear equatorward decay. On the other hand, $P(v)$ attains a maximum near the equator, especially for the WMWs with periods of 12-

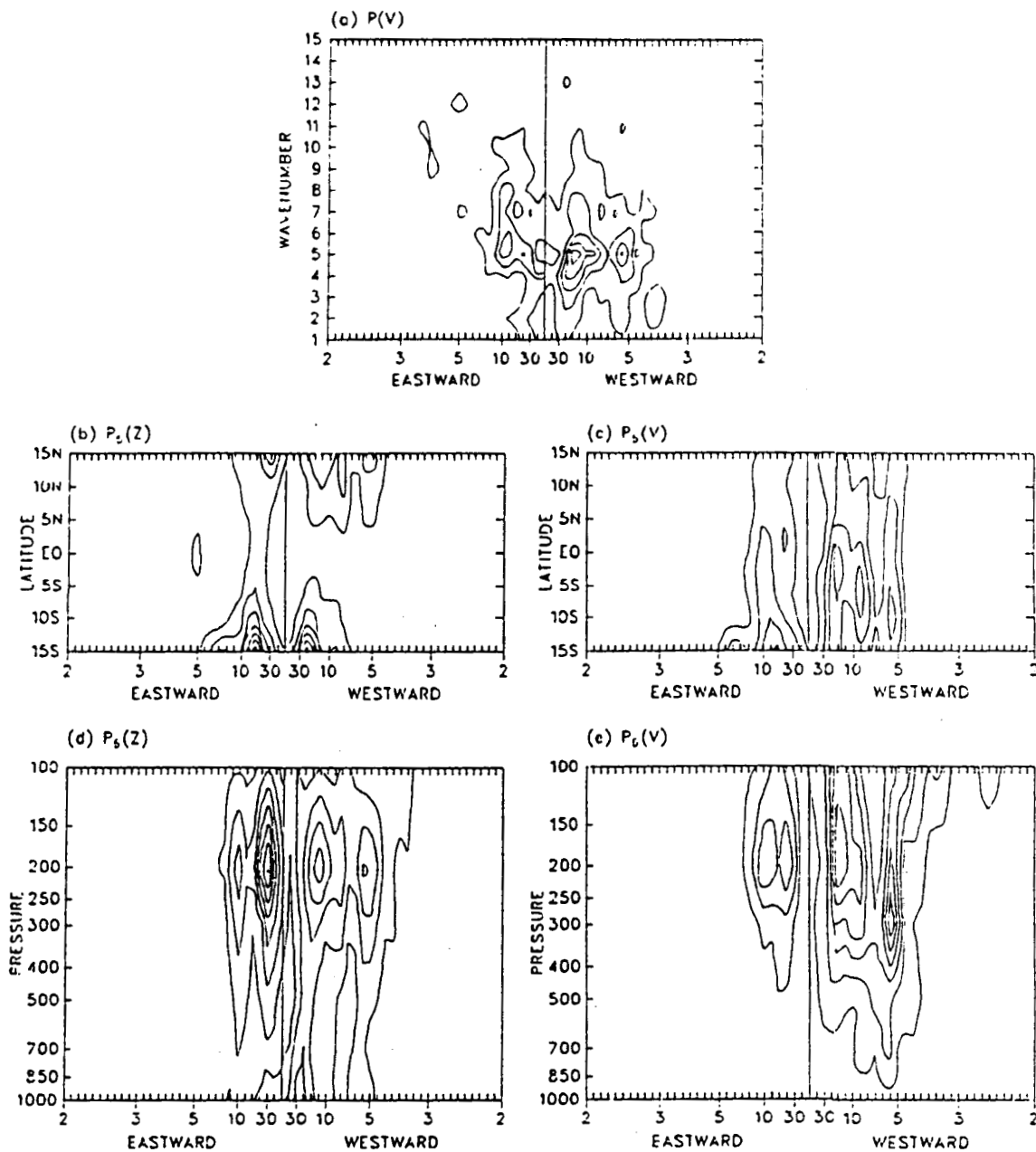


Figure 14. Power spectral analyses of (a) meridional wind (2N, 200 mb), (b) wavenumber 5 geopotential height (200 mb), (c) wavenumber 5 meridional wind, (d) wavenumber 5 geopotential height (15N) and (e) wavenumber 5 meridional wind (2N) for the control experiment over the northern summer. Contour intervals are $1 \text{ m}^2 \text{ s}^{-2} \text{ day}$ in (a), $15 \text{ m}^2 \text{ day}$ in (b), $1.5 \text{ m}^2 \text{ s}^{-2} \text{ day}$ in (c), $8 \text{ m}^2 \text{ day}$ in (d) and $0.8 \text{ m}^2 \text{ s}^{-2} \text{ day}$ in (e)

15 days (Figure 14c). Figures 14d and 14e demonstrate the vertical distributions of $P(z)$ and $P(v)$ associated with $m=5$ at 15N and 2N, respectively. It is evident that almost all the spectral peaks occur near 200 mb.

Knowing the horizontal and vertical structures of these spectral peaks, we infer that the the spectral peaks with eastward periods are eastward moving inertial-gravity waves which might be generated by the model. The nature of the spectral peak associated with westward periods of 5.5 days is not clear since the horizontal structure of the disturbance does not fit into any wave structure predicted by the linear wave theory. All the features associated with the spectral peak at $m=5$ and periods of 12-15 days are indications of a mixed Rossby-gravity wave.

b. Propagation characteristics The horizontal distributions of geopotential height and horizontal wind components associated with $m=5$ and periods of 12-15 days at 200 mb are shown in Figure 15. The geopotential height distribution exhibits approximate antisymmetry about the equator with high and low centers located around 13N and 6S. The horizontal wind is clockwise around the pressure system of the NH low and the SH high. The estimated amplitude of the meridional wind at the equator is about 0.6 ms^{-1} . The amplitude of the mixed Rossby-gravity wave observed by Zangvil and Yanai (1980) is about 0.8 ms^{-1} . Yanai and Murakami (1970) obtained an amplitude for meridional velocity of about 2.5 ms^{-1} (this includes contributions from all wavenumbers of EMW and WMW) at 200 mb. Thus the amplitude of the

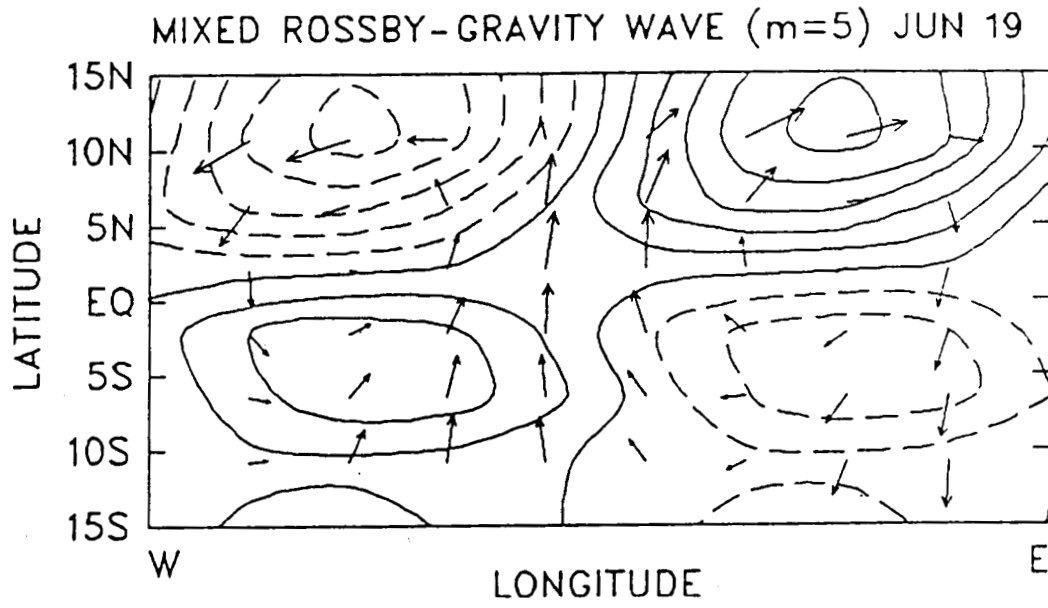


Figure 15. Same as Figure 4, except for the mixed Rossby-gravity wave with $m=5$ and periods of 12-15 days

mixed Rossby-gravity wave in the present study is very close to those observed.

For mixed Rossby-gravity waves, the latitudinal width Y_L and the vertical wavelength L_z may be computed from (Holton, 1979)

$$Y_L = \left| \frac{2\hat{\omega}/m}{\beta(\beta/\hat{\omega}m - 1)} \right|^{\frac{1}{2}}, \quad (5.3)$$

and

$$L_z = \frac{2\pi\hat{\omega}/m}{S^{\frac{1}{2}}(\beta/\hat{\omega}m - 1)}. \quad (5.4)$$

The estimated values of Y_L and L_z are given in Table 3. For example, from Figure 2, if we take the Doppler-shifted phase speed to be 5 ms^{-1} in the SH, then the latitudinal width is about 8° latitude and the vertical wavelength is about 3 km.

Figure 16 shows a height-time section of meridional wind with $m=5$ and periods of 12-15 days at 2N during the period in which the mixed Rossby-gravity wave is significant. It reveals a regular oscillation in v associated with the mixed Rossby-gravity wave and exhibits a little tendency of downward propagating phase in the upper troposphere, which is in agreement with the result obtained by Tsay (1974) who showed that the mixed Rossby-gravity wave ($m=2$, period=4.6 days) simulated by the NCAR stratospheric GCM have a downward propagating phase.

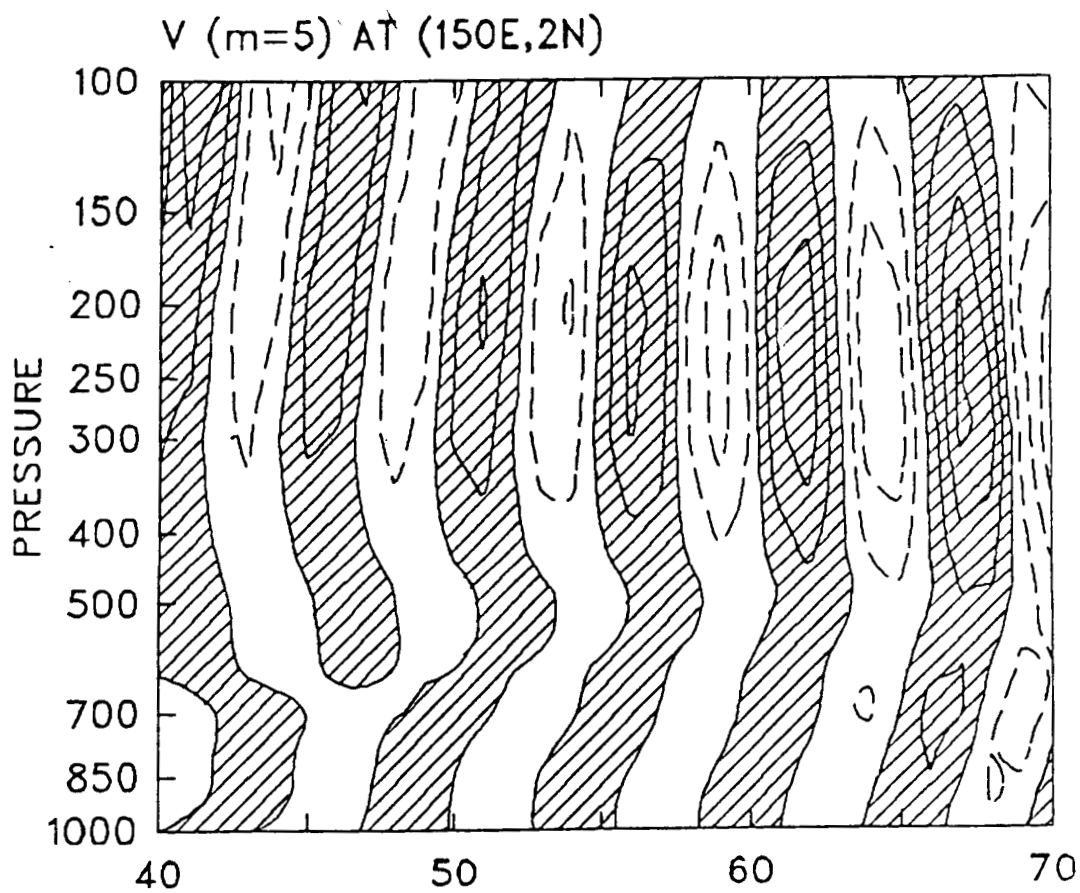


Figure 16. Height-time cross section of meridional wind with $m=1$ and westward moving periods of 12-15 days for the control experiment over the northern summer. Contour interval is 0.5 ms^{-1} . Values greater than zero are hatched

c. Precipitation and forcing inference As mentioned in Chapter II, there are two important hypotheses on the generation of mixed Rossby-gravity waves. One is the lateral forcing theory proposed by Mak (1969), who assumed that the vertical wavelength of the wave coincides with the vertical wavelength of lateral forcing through linear resonance. Thus, the westward moving resonant waves have a large response at $m=3$ and periods of 4 days. However, Hayashi (1976) noted that by imposing midlatitude forcing as a lateral boundary forcing, the resonant waves are spurious "westward Kelvin waves" having a horizontal structure completely different from mixed Rossby-gravity waves.

The other hypothesis is called wave-CISK theory. This theory proposes that the interaction between equatorial waves and cumulus convection is unstable and that it can produce mixed Rossby-gravity waves. However, this theory predicts sharp spectral peaks in the heating field, which is not detected in the real atmosphere. Very recently, however, it has been shown by two studies (Hayashi and Sumi, 1986; Lau and Peng, 1987) that if a nonlinear effect is taken into account in wave-CISK, results concerning the wavenumber and period selection change completely. Therefore, it would be interesting to investigate whether a nonlinear model with wave-cumulus interaction produces mixed Rossby-gravity waves with the same spectral peak in wavenumber and frequency as observed waves.

Figure 17 shows latitude-time sections of the oscillations of z associated with the mixed Rossby-gravity wave and precipitation with

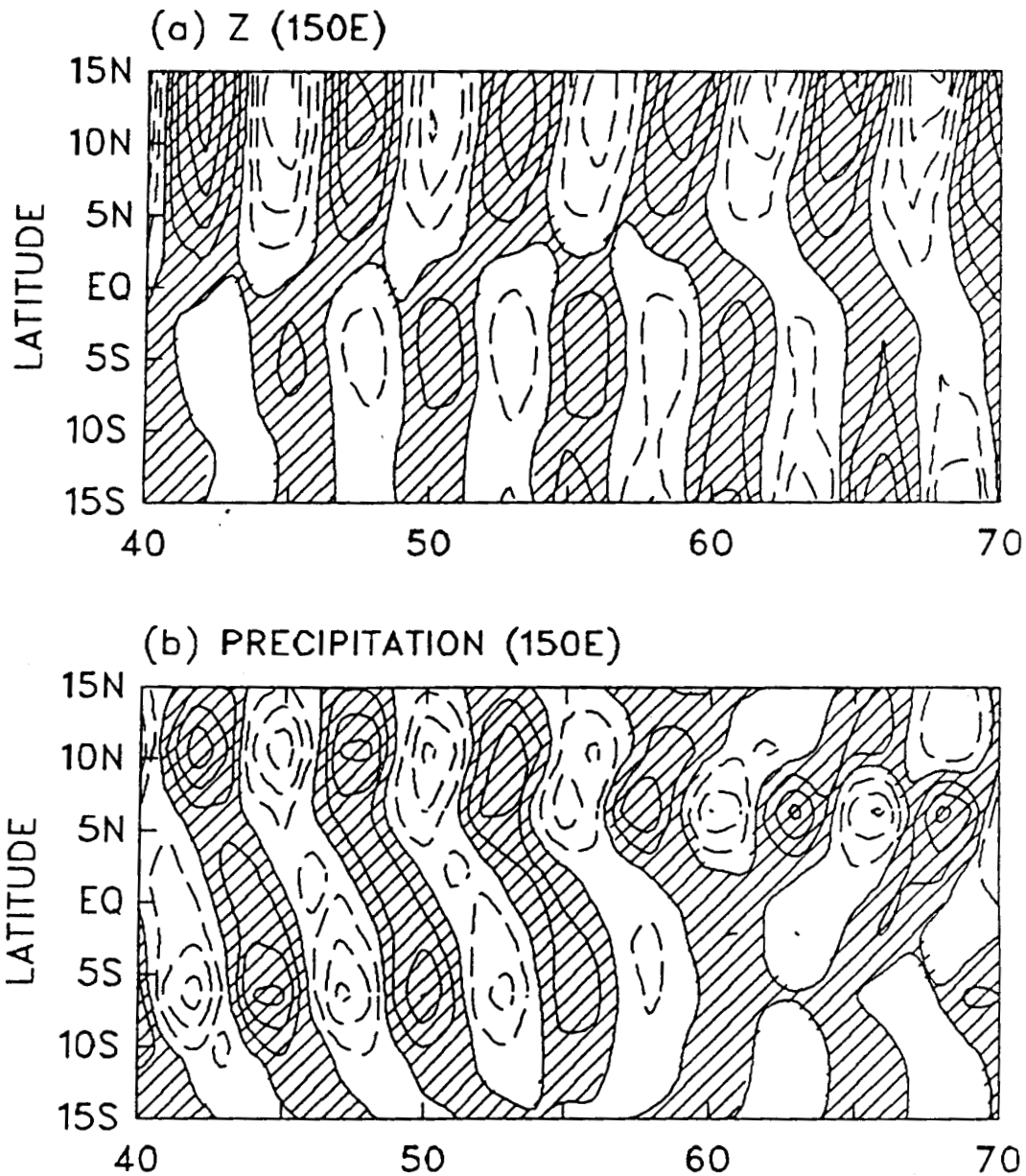


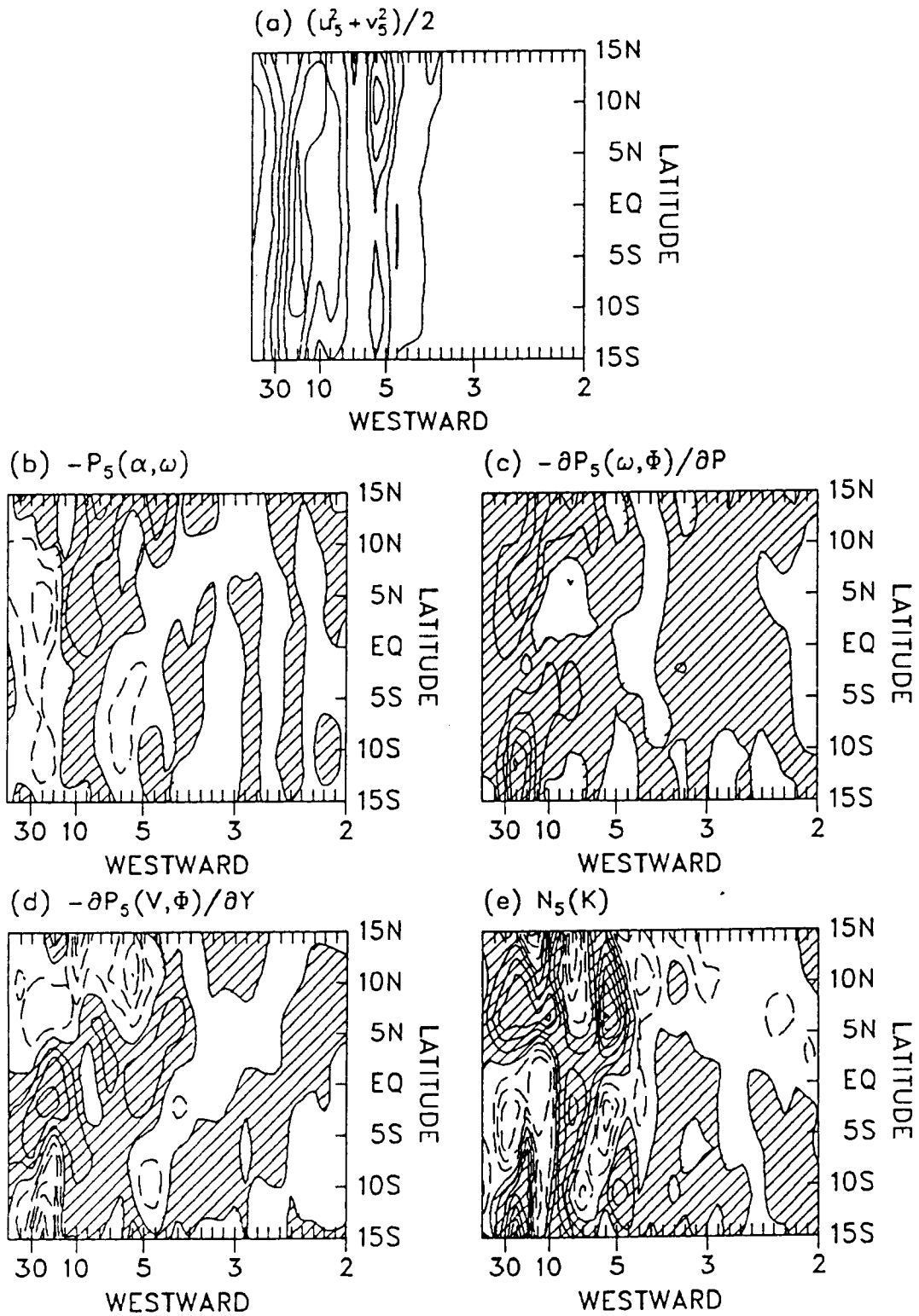
Figure 17. Latitude-time cross sections of geopotential height with $m=1$ at 200 mb (a) and precipitation rate with $m=1-15$ (b) associated with westward moving periods of 12-15 days for the control experiment over the northern summer. Contour intervals are 1 meter in (a), and 2 mm day^{-1} in (b). Values greater than zero are hatched

$m=1-15$ and periods of 12-15 days. Figure 17a reveals clearly the oscillation of the mixed Rossby-gravity wave with the maximum pressure at 6S and 12N, especially during the period of days 45-57 (May 14-26). The precipitation (Figure 17b) exhibits an antisymmetric structure with respect to the equator, while the maximum precipitation in both hemispheres migrates equatorward. From the two figures, it is evident that the oscillations of the two fields are in phase during days 45-57.

The significant coherence between the mixed Rossby-gravity wave and precipitation indicates that latent heat release from cumulus convection might be the energy source for the mixed Rossby-gravity wave. This confirms the results obtained by Itoh and Ghil (1988), who recently performed a numerical experiment to investigate the excitation mechanism of the mixed Rossby-gravity waves in the tropical troposphere. They found the coherence between lateral forcing and low-level convergence, on one hand, and between the mixed Rossby-gravity wave and convergence, on the other, are very high. Therefore, the lateral forcing, highly correlated with low-level convergence and precipitation, appears to influence mixed Rossby-gravity waves via low-level convergence and ensuing precipitation, but exhibits only a low direct correlation with the waves.

d. Maintenance of the mixed Rossby-gravity wave Figure 18 presents the energetic budget analysis of equation (4.17) for the mixed Rossby-gravity wave. It is evident that the WMs with $m=5$ have appreciable kinetic energy in the period range of 5-60 days. The

Figure 18. Same as Figure 9, except for wavenumber 5 and westward moving periods. Contour intervals are 0.8 J in (a); 0.5×10^{-5} W in (b), (c) and (e); and 10^{-5} W in (d). Values greater than zero are hatched



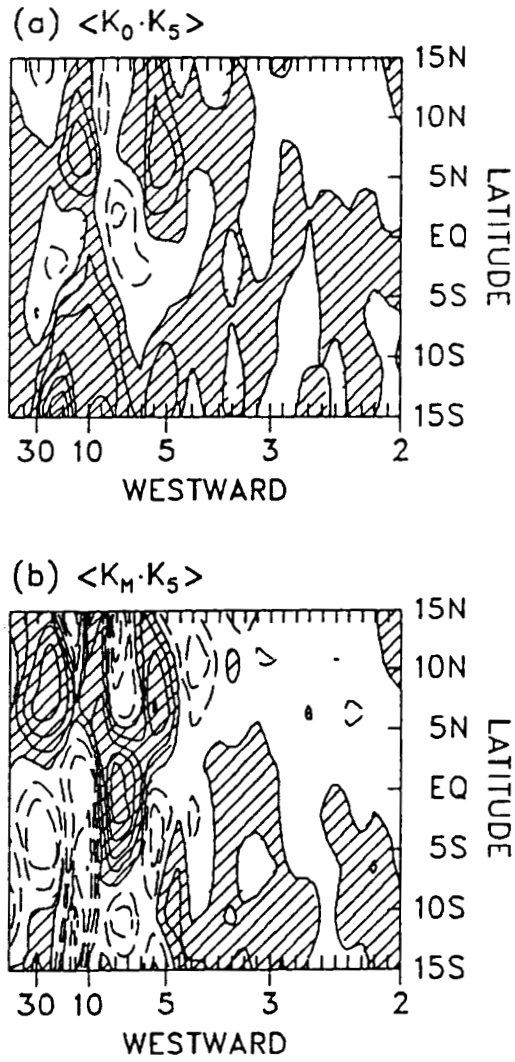


Figure 19. Same as Figure 10, except for wavenumber 5 and westward moving periods

kinetic energy associated with the mixed Rossby-gravity wave is almost constant from 15S to 15N.

The conversion of available potential energy into kinetic energy is displayed in Figure 18b. Although this quantity becomes significant toward the low frequency regime, the contribution from this quantity to the mixed Rossby-gravity wave over the period of 12-15 days can be almost neglected. This indicates that the wave has a somewhat barotropic nature as shown in Figure 16.

Figure 18c shows the vertical convergence of wave energy flux. There are two convergence centers with periods of 12-30 days lying at 12S and 6N, which imply two ascending branches of the Hadley cells associated with cumulus convection during Northern Summer. Again, it demonstrates that the mixed Rossby-gravity wave is maintained, to some extent, by latent heat release in the tropics (Hayashi and Golder, 1978).

The meridional convergence of wave energy flux shown in Figure 18d is characterized by two convergence centers near the equator at periods of 5-6 days and 12-30 days, respectively. In agreement with previous studies by Zangvil and Yanai (1980) and Yanai and Lu (1983), there is appreciable equatorward wave energy flux associated with the WMW at period range of 12-30 days, in which the mixed Rossby-gravity wave is observed. Although the resonant wave theory of Mak (1969) proved to be unrealistic, the previous studies mentioned above still show that the mixed Rossby-gravity waves are closely related to the energy flux from midlatitudes.

Figure 18e presents the kinetic energy transfer into the WMWs with $m=5$ through nonlinear processes. It is evident that the nonlinear effects become significant for these waves with periods longer than 5 days. The nonlinear energy transfer associated with the mixed Rossby-gravity wave is positive north of 3N and negative south of 3N.

Figure 19 shows the nonlinear transfer due to the wave-mean and wave-wave interactions. In Figure 19a, it is evident that the WMWs at periods of 12-15 days gain kinetic energy from the mean flow north of 2N and south of 4S. However, based upon linear wave theory, Zangvil and Yanai (1980) showed that the mixed Rossby-gravity wave with $m=4$ and a period of 5 days is accompanied by a conversion of eddy kinetic energy to kinetic energy of the mean flow.

The energy transfer due to the wave-wave interaction is displayed in Figure 19b. The energy transfer for those WMWs with periods longer than 5 days is significant, while the WMWs with periods of 12-15 days, for which the mixed Rossby-gravity wave is observed, lose kinetic energy between 15S and 5N.

5. Rossby wave in the winter season

a. Spectral analysis Figure 20 presents the power spectral analysis of the Rossby wave. The top figure shows the power spectrum of z at the 200 mb level and 15N in the wavenumber-frequency domain. There is a spectral peak at $m=3$ and period range of 20-30 days. A similar pattern is also exhibited in $P(u)$ at 2N (not shown). The vertical structure of $P(z)$ with $m=3$ at 15N reveals a significant peak

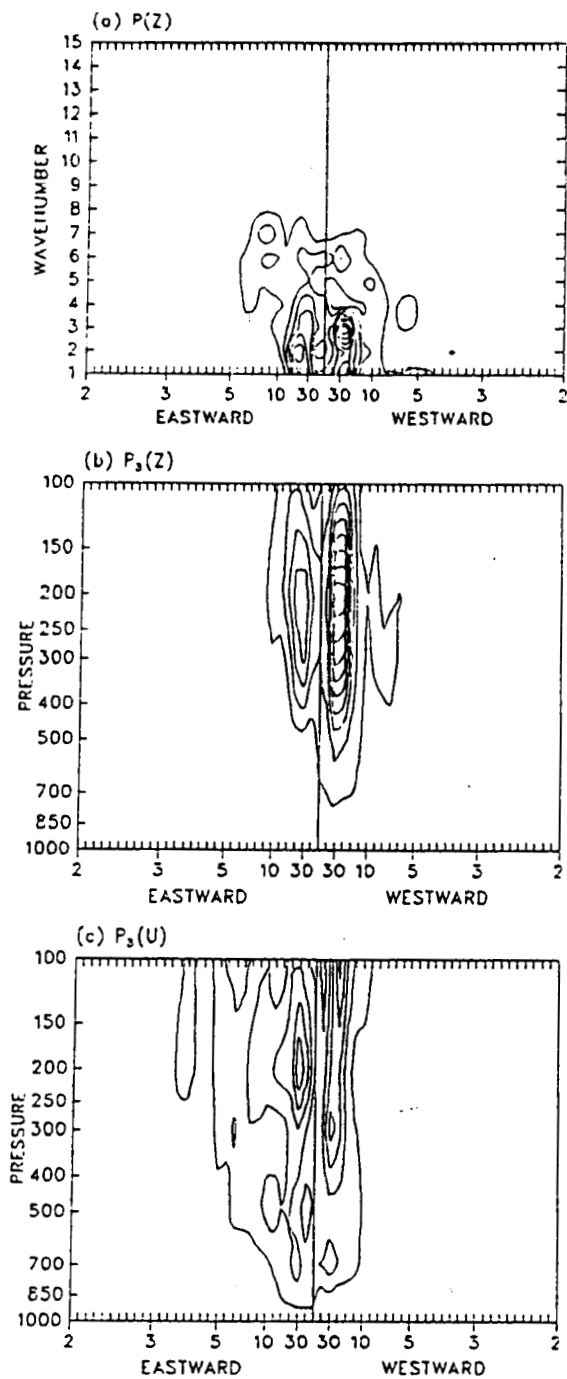


Figure 20. Power spectral analyses of (a) geopotential height (15N, 200 mb), (b) wavenumber 3 geopotential height (15N), and (c) wavenumber 3 zonal wind (2N) for the control experiment over northern winter. Contour intervals are $25 \text{ m}^2 \text{ day}$ in (a) and (b), and $1.5 \text{ m}^2 \text{ s}^{-2} \text{ day}$ in (c)

c-2

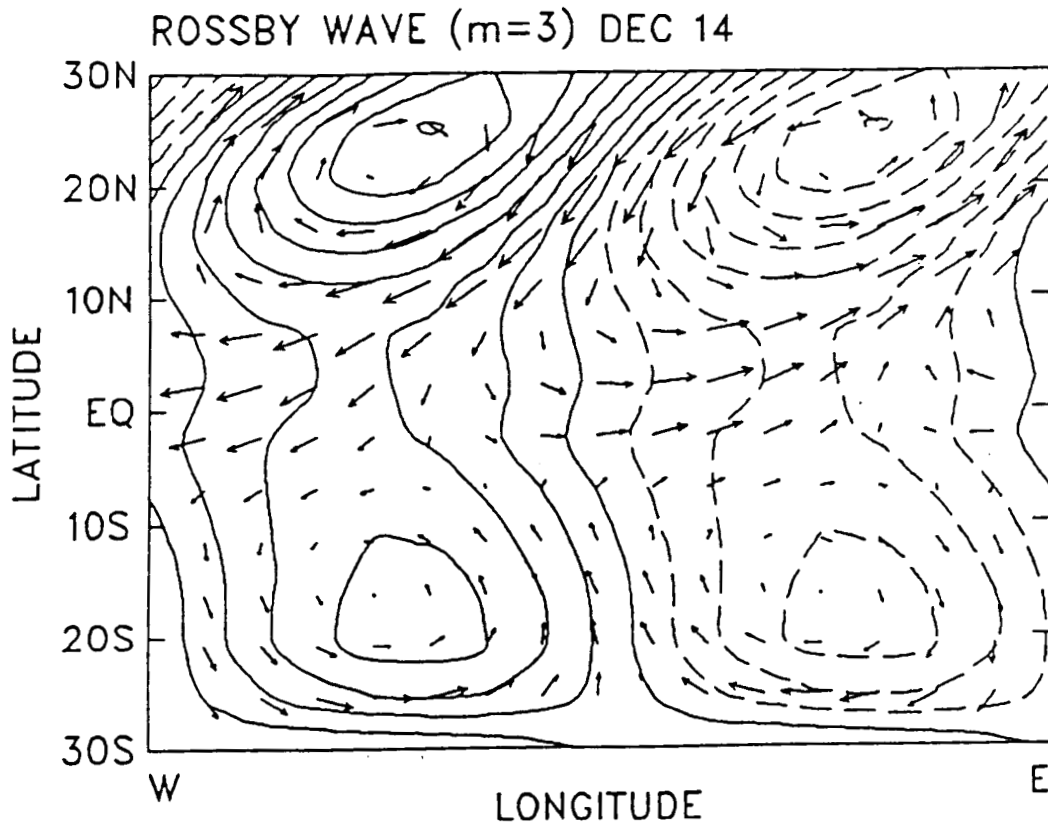


Figure 21. Same as Figure 4, except for the Rossby wave with $m=3$ and westward moving periods of 20-30 days in the control experiment over the northern winter. Contour interval is 2 m

with westward periods of 20-30 days at 200 mb. $P(z)$ at this period is significant. A weaker spectral peak with eastward periods of 20-30 days is also observed. The vertical distribution of $P(u)$ with $m=3$ at 2N behaves the same way as $P(z)$. A significant spectral peak with westward periods of 20-30 days occurs from 400 mb all the way up to 100 mb, while another spectral peak corresponding to the one with eastward period in $P(z)$ is also noticed. The spectral analysis indicates that $P(z)$ attains its maximum somewhere away from the equator, and that $P(u)$ has its maximum on the equator. It strongly suggests that the spectral peak with westward period is a signal of the existence of a Rossby wave with $m=3$ and periods of 20-30 days. The nature of the spectral peak associated with eastward period is not clear.

b. Propagation characteristics Figure 21 shows the latitudinal structures of geopotential height and horizontal wind of the Rossby wave for $m=1$ and periods of 20-30 days. It is evident that z and u have symmetric structures and v has antisymmetric structure with respect to the equator, which corresponds to the Rossby wave with latitudinal nodal wavenumber $n=1$ depicted by Matsuno (1966).

Following the correction method used by Diky and Golitsyn (1968) and Walkerscheid (1980), we calculate the vertical wavelength and latitudinal width by taking into account the effects of mean zonal flow. From Figure 2, if we take the mean zonal flow to be 10 ms^{-1} in the tropics, then the effective rotation rate of the earth is $\Omega_e = 1.02\Omega_0$, Ω_0 is the rotation rate of the earth and the Doppler-shifted

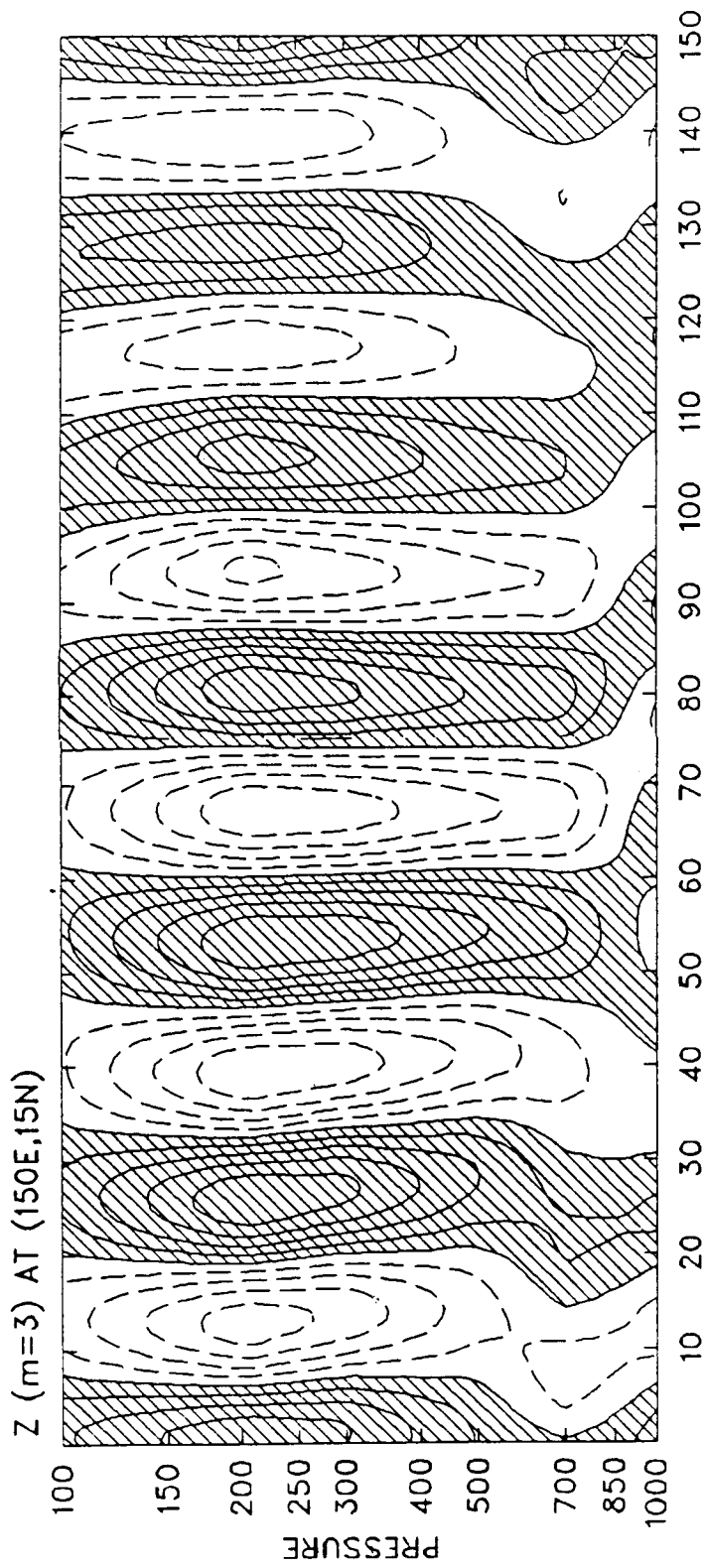


Figure 22. Height-time cross section of geopotential height with $m=3$ and westward moving periods of 20-30 days for the control experiment over the northern winter. Contour interval is 2 m. Values greater than zero are hatched

ORIGINAL PAGE IS
OF POOR QUALITY

angular frequency of the Rossby wave $\hat{\omega} = 0.11\Omega_0$. Thus the vertical wavelength of the Rossby wave estimated from the dispersion curves of Longuet-Higgins (1968) is about 16 km and the maximum pressure is located at 15° latitude. Comparing with the Figure 21, we find that the location of the maximum pressure in the SH is consistent with that obtained from linear wave equation, while the one in the NH is not well predicted theoretically. This wave is identified as an equatorially trapped Rossby wave with zonal wavenumber $m=3$, latitudinal wavenumber $n=1$ and a period of 20-30 days.

Although Rossby-type waves in the upper troposphere have been noted by synoptic analysis (Yanai, 1963) and by spectrum analysis (e.g., Yanai and Murakami, 1970; Nitta, 1972), the evidence from time-spectrum analysis was not strong. Gruber (1975) presented some evidence suggesting the existence of a Rossby wave with $m=5-6$ and a period of about 7 days. Yanai and Lu (1983) identified an equatorially trapped Rossby wave with $m=2$ and a period of 10 days, and with $m=2$ and a period of 30 days from observational data at 200 mb during 1967 and 1972, respectively. The amplitudes in u of both waves are about $3-4 \text{ ms}^{-1}$ at the equator, which is close to 2.7 ms^{-1} of the present study.

Figure 22 shows the height-time section of the oscillation in z associated with the Rossby wave at 150E longitude and 15N. It reveals a regular oscillation of the Rossby wave with maximum amplitude near the 200 mb level.

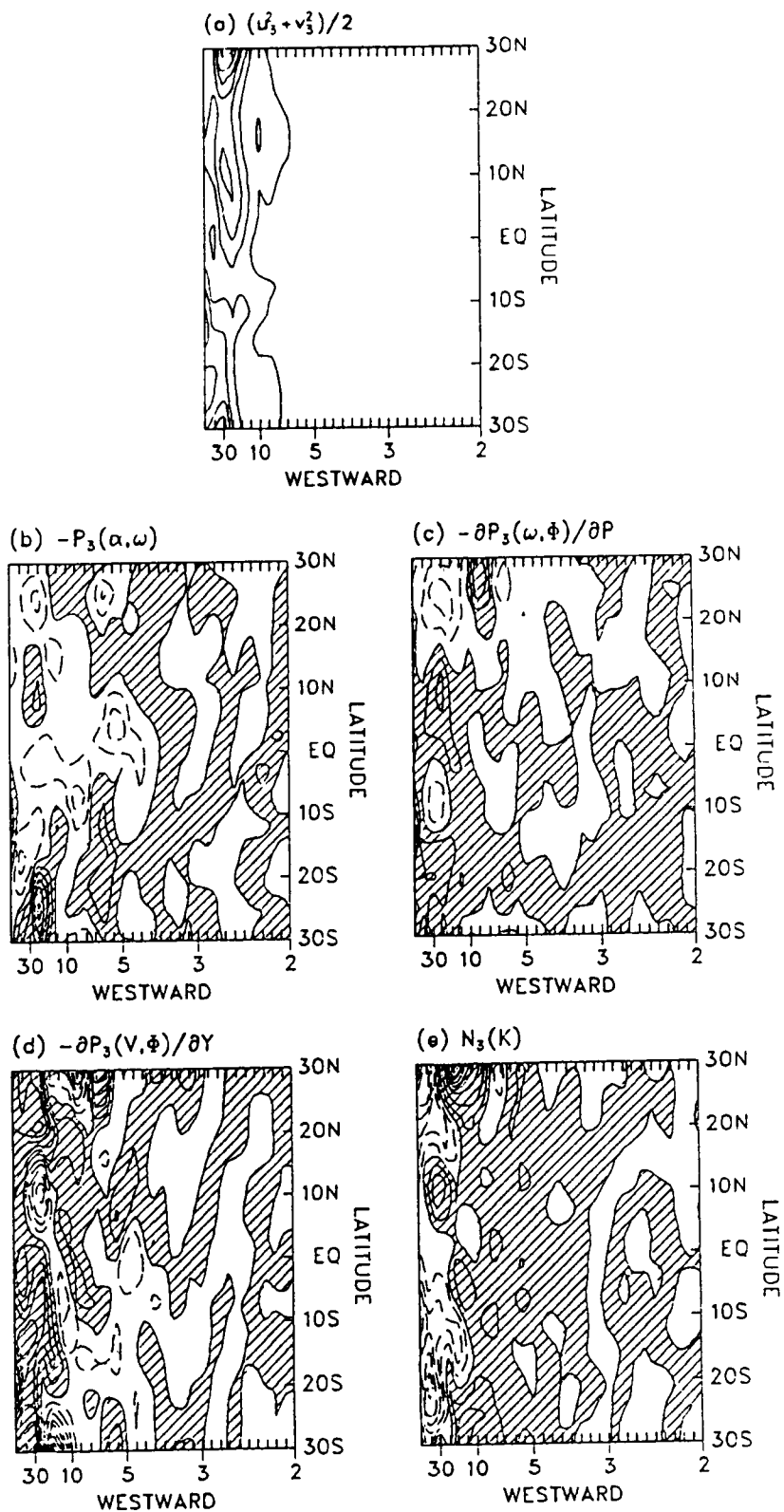
c. Maintenance of the Rossby wave Figure 23 presents the energetic budget analysis of equation (4.17) for the Rossby wave. The kinetic energy with $m=3$ is shown in Figure 23a. Large kinetic energy is concentrated in the long-period part of the spectrum. This kinetic energy with periods of 20-30 days, at which the Rossby wave is observed, is significant from 30S to 30N with a maximum at 10N. Midlatitude systems with a period of about 30 days are also observed at 30S and 30N.

Figure 23b shows the conversion of available potential energy into kinetic energy. Significant conversions take place in two period ranges: 5-7 days and 15-30 days. We note that the period range of 15-30 days corresponds to that of the Rossby wave. The vertical convergence of wave energy flux in this period range is also significant (Figure 23c). Over this period range, there are two convergence centers lying at 20S and 10N, where ascending branches of winter Hadley cells are located. Therefore the thermal effect is one of the important factors for the maintenance of equatorially trapped Rossby waves.

Figure 23d presents the meridional convergence of wave energy flux. It is evident that the convergence associated with WMs with periods less than 5 days is very weak. However, the meridional convergence of wave energy flux for those WMs with periods of 20-30 days, including the Rossby wave, is significant between the equator and 20S, and north of 15N. Between the two regions of convergence, wave energy flux diverges at 10N transporting out the energy

Figure 23. Same as Figure 9, except for wavenumber 3 and westward moving periods. Contour intervals are 1.5 J in (a); 0.5×10^{-5} W in (b); 10^{-5} W in (c), (d) and (e)

ORIGINAL PAGE IS
OF POOR QUALITY



ORIGINAL PAGE IS
OF POOR QUALITY

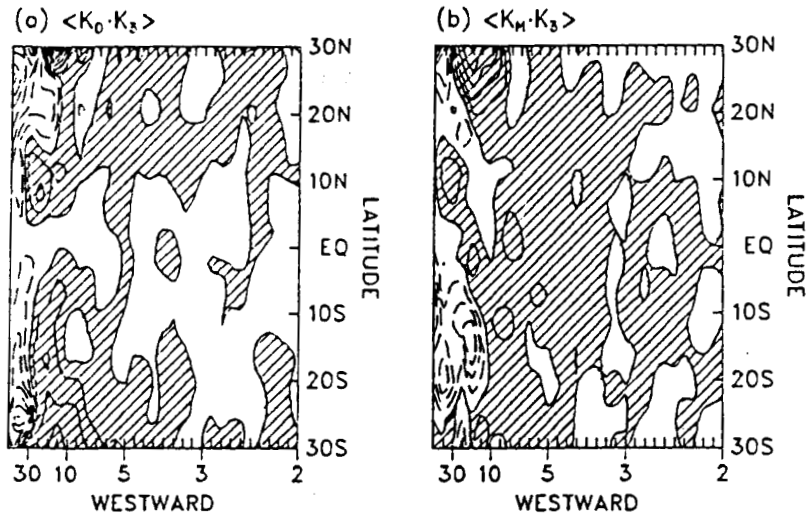


Figure 24. Same as Figure 10, except for wavenumber 3 and westward moving periods. Contour intervals are 0.5×10^{-5} W in (a), and 10^{-5} W in (b)

accumulated by the thermal field at this latitude. We also notice that a divergence of wave energy flux with periods of 12-30 days is located at 30S. This divergence indicates disturbances from the midlatitude of the SH can freely propagate into the tropics as discussed by Charney (1969) and Bennett and Young (1971).

The kinetic energy transfer into WMs with $m=3$ through nonlinear processes is displayed in Figure 23e. Similarly, appreciable energy transfer takes place only in the period range of 12-30 days, in which the Rossby wave is identified. It is evident that the Rossby wave loses kinetic energy at all the latitudes except near 10N, where the wave gains energy through nonlinear processes.

Separating the nonlinear energy transfer into wave-mean flow and wave-wave interactions (Figure 24), we find that kinetic energy is transferred into the Rossby wave near 10N in both nonlinear interactions, while the Rossby wave gains kinetic energy between 20S and 5S in the wave-mean flow interaction and then the kinetic energy is transferred into other waves in the wave-wave interaction.

B. The No-mountain Experiment

From the above analysis of the control experiment, we have seen that the NCAR CCMI is able to simulate equatorial planetary waves which compare reasonably well to observations. In order to evaluate the role of the earth's orography in the excitation of these waves, we analyzed a numerical experiment with CCMI by eliminating mountains from the model. As the result, only Kelvin waves are identified in both winter and summer seasons. Since the Kelvin waves in both

seasons have similar propagation characteristics, we shall only discuss the Kelvin wave in the summer season in this section.

1. Spectral analysis

Figure 25a shows the power spectrum of z at 200 mb and 2N in the wavenumber-frequency domain. A striking feature of this figure is the concentration of $P(z)$ in the low-wavenumber and long-period regime. Examining the effect of the equatorial Pacific sea surface temperature anomaly on the atmospheric circulation using the NCAR CCM0 with and without mountains, Blackmon et al. (1987) found that removing the mountains in the model produces a more zonally uniform flow and the stationary waves have smaller amplitudes than those in the mountain case, especially for zonal wavenumbers 2 and 3. Comparing with Figure 25a and Figure 3a, we find the power of z associated with wavenumber 2 and 3 is reduced significantly. It is evident that EMWs are dominant, especially the disturbance with $m=1$ and periods of 15-20 days.

Shown in Figures 25b and 25c are $P(z)$ and $P(u)$ with $m=1$ at 200 mb as a function of latitude and frequency. Both spectra are dominated by EMWs, which are symmetric with respect to the equator and decay away from the equator, while the power spectrum of the meridional wind at $m=1$ is extremely small (not shown). We also note that the extratropical disturbances, especially stationary disturbances, are reduced markedly in the no-mountain experiment. Therefore, the possible interaction between midlatitude and tropics may be reduced.

Figures 25d and 25e show height-frequency sections of zonal wave 1 geopotential height and zonal wind component at 2N. The vertically

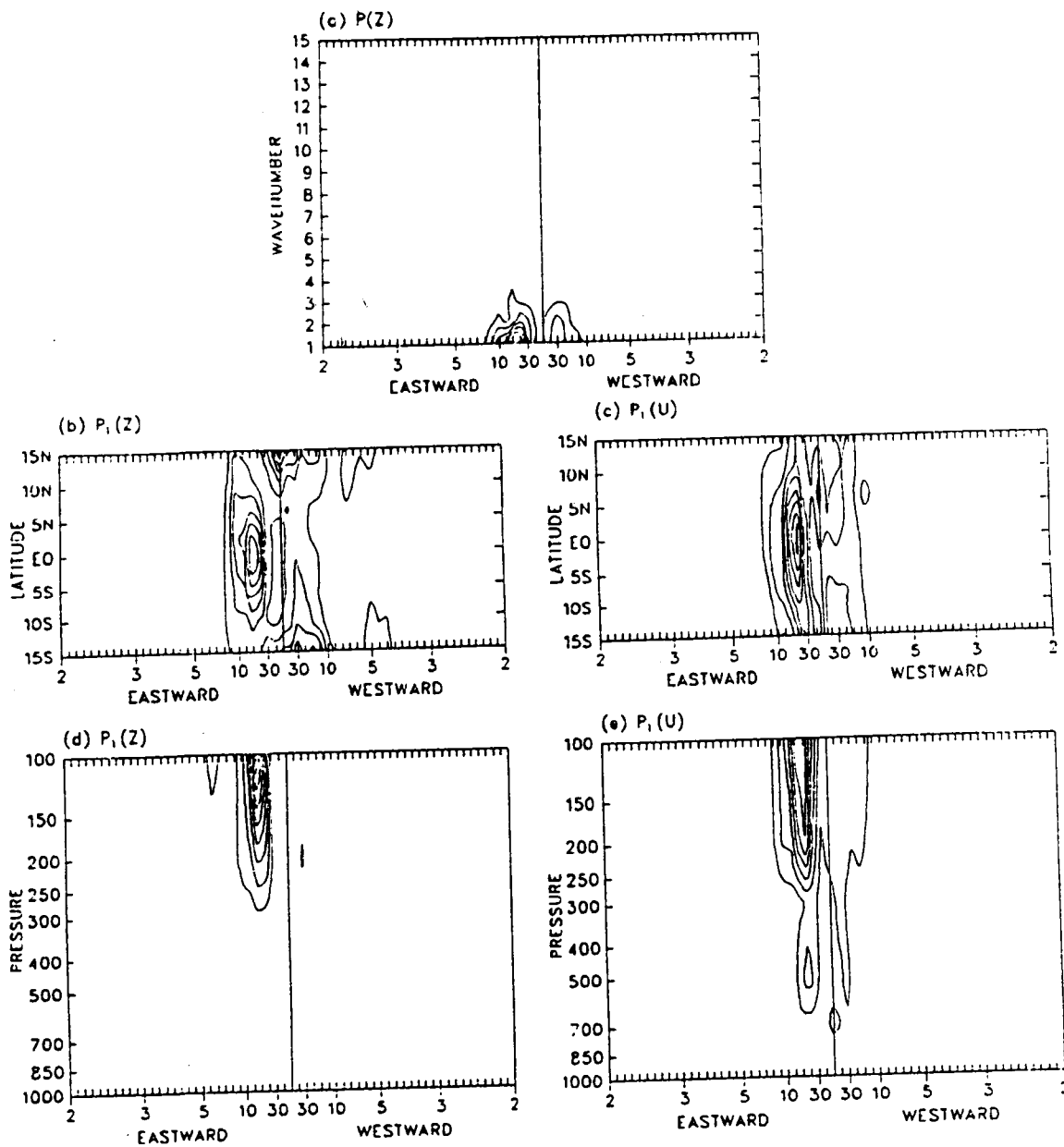


Figure 25. Same as Figure 3, except for the no-mountain experiment

ORIGINAL PAGE IS
OF POOR QUALITY

coherent structures of the EMWs at the period identified above are evident.

2. Propagation characteristics

The above spectral analysis strongly suggests the possible existence of the Kelvin wave at $m=1$ and periods of 15-20 days. Figure 26 shows the horizontal distributions of geopotential height and winds at 200 mb for periods of 15-20 days with $m=1$. From equations (5.1) and (5.2), the latitudinal width and vertical wavelength in this case are estimated to be 13° latitude and 7 km, respectively. In Figure 26, the amplitudes of fluctuations of zonal wind are $1-3 \text{ ms}^{-1}$, and the fluctuations of z are 10-14 m at the equator. It is evident that the characteristics of the Kelvin wave in this case are similar to those in the control case except with a smaller period. This suggests that the topography, with which the stationary wave and midlatitude disturbances are associated, has little effect on the propagation characteristics of Kelvin waves in the tropics.

Figure 27 shows the oscillations of the Kelvin wave in z and u at $2N$. It reveals that there are two episodes of the Kelvin wave in this sample period: days 0-50 and 95-130. In contrast to those in the control run, the eastward propagating modes in this case exhibit downward phase progression over the entire sample period, with the maximum amplitudes occurring in the lower stratosphere. The two features mentioned above indicate the effect of topography on large-scale motions. As pointed out by Held (1983), thermally forced eddies and mountain forced eddies have rather different structures. The

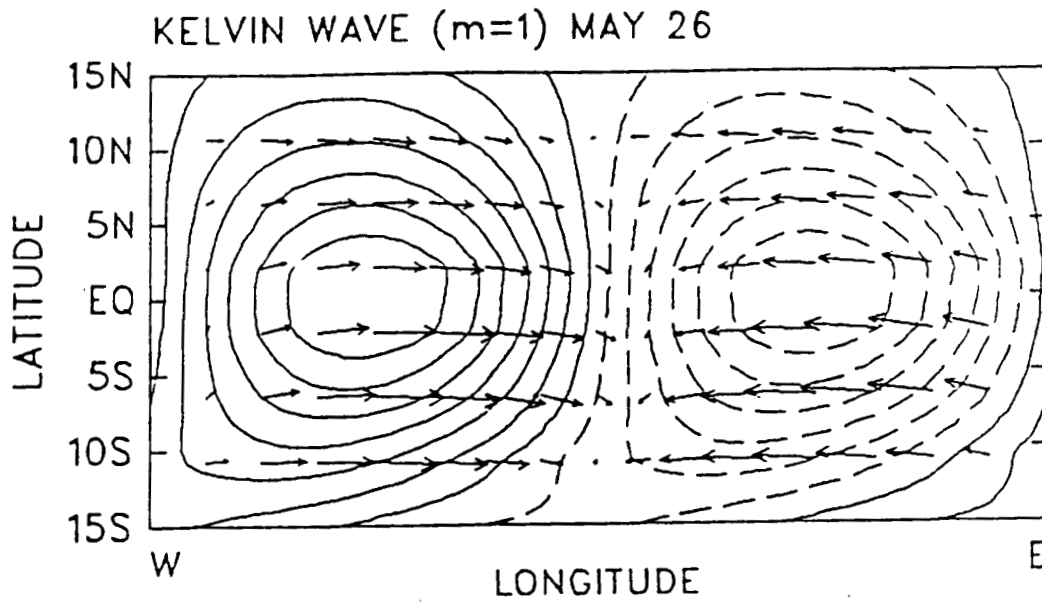


Figure 26. Same as Figure 4, except for the Kelvin wave with $m=1$ and periods of 15-20 days for the no-mountain experiment. Contour interval is 2 m

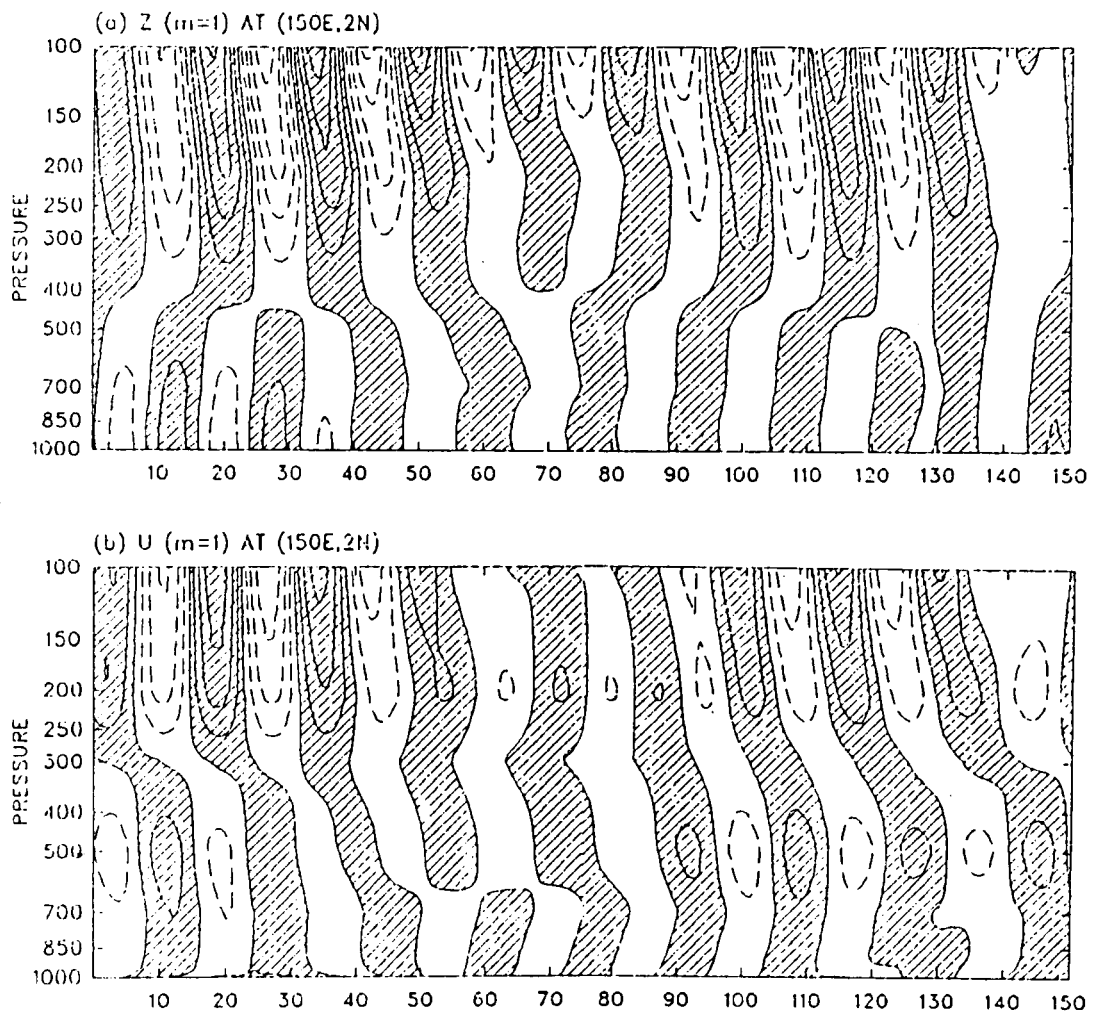


Figure 27. Same as Figure 5, except for eastward moving periods of 15-20 days. Contour intervals are 4 m in (a), and 1.5 ms^{-1} in (b). Values greater than zero are hatched

former are of larger scale than the latter, particularly in the upper troposphere. They also have a larger and more systematic westward phase shift with height and show somewhat less of a tendency toward maximum amplitude at the tropopause. The mountain forced eddies, on the other hand, tend to reach their maximum amplitudes near 200 mb and exhibit less westward phase tilt with height.

Vertical phase change of the zonal wind oscillation during the episodes of the Kelvin wave (Figure 27b) indicates that the vertical structure of low-level convergence and upper-level divergence accompanies the Kelvin wave. Corresponding features can also be observed in Figure 27a.

3. Precipitation and forcing inference

Mountains have a considerable effect on the longitudinal distribution of tropical precipitation. Figures 28a and 28b show time averaged precipitation rate and the precipitation variance for the no-mountain case. Removing mountains from the model produces a more zonally uniform distribution of tropical rainfall, which agrees with the results obtained by Manabe and Terpstra (1974) and Blackmon et al. (1987). Tzeng and Chen (1988) showed that the divergent center over the western Pacific Ocean at 200 mb shifted northeastward in response to the removal of the mountains, while the northward shift of precipitation variance associated with the divergent center is also evident in Figure 28b.

Blackmon et al. (1987) noted substantial differences between the precipitation simulated with and without mountains in several areas of

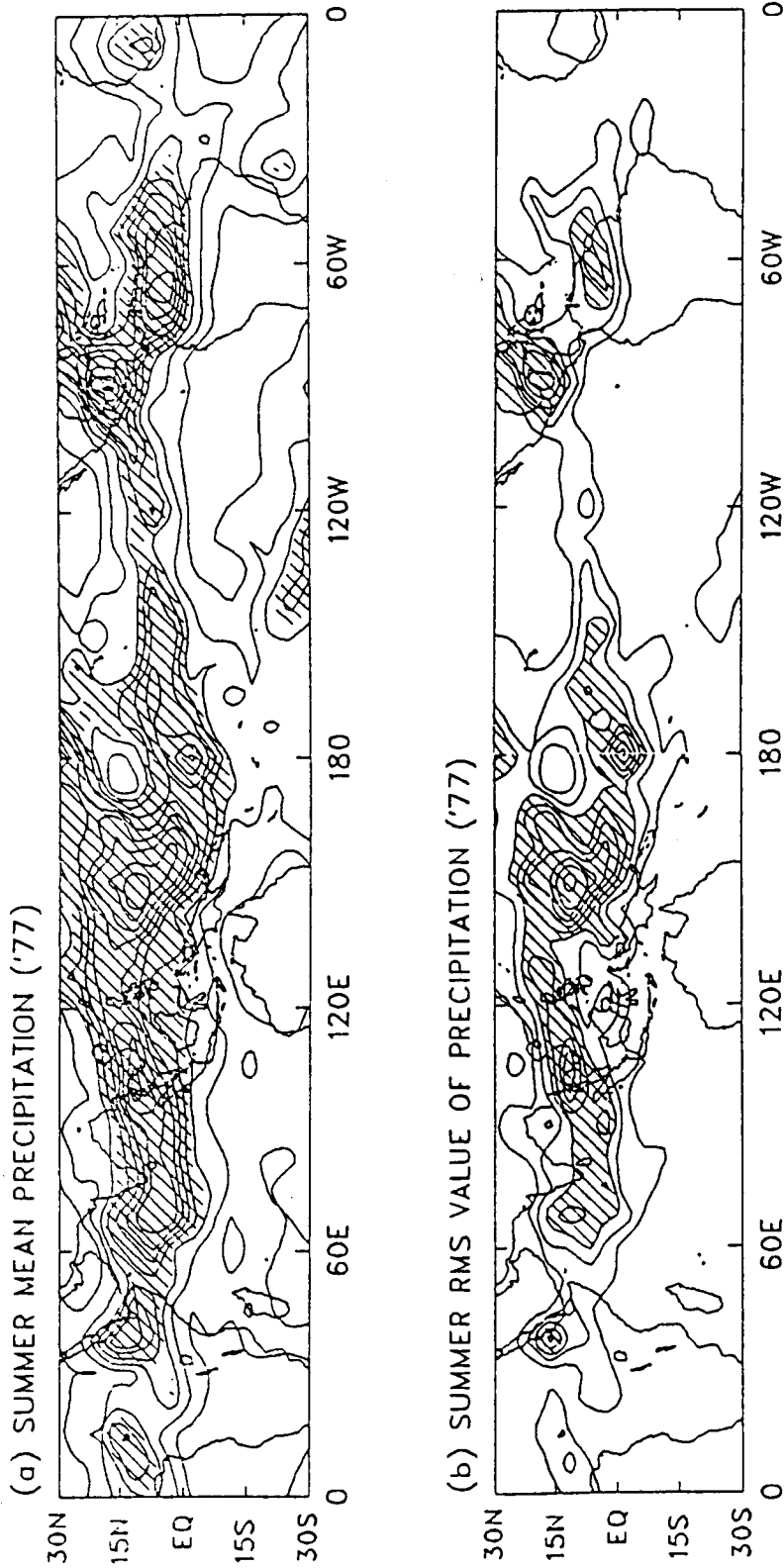


Figure 28. Same as Figure 6, except for the no-mountain experiment. Contour intervals are 1.5 mm day⁻¹ in (a), and 100 mm² day⁻² in (b). Values greater than 4.5 and 300 are hatched in (a) and (b), respectively

the tropics; e.g., east of the Andes, over the Atlantic and Indian Oceans and, most notably, near the East Indies. This is also true in the present study when we compare the precipitation rate of the control run (Figure 6a) with the no-mountain run (Figure 28a). If one views this as an anomaly experiment, the mountain minus no-mountain precipitation difference gives marked heating anomalies throughout the tropics. Therefore, the no-mountain climates can not be interpreted as simply due to the lack of orographic effect on the atmospheric flow, since the insertion of the mountains has some effect on the distribution of diabatic heating as well.

Figures 29a and 29b show latitude-time sections of z with $m=1$ and eastward periods of 15-20 days at 200 mb and precipitation rate with $m=1-15$ and the period of the Kelvin wave. The two episodes of the Kelvin wave are evident in Figure 29a. It is seen that the latitudinal width of the Kelvin wave agrees well with that calculated from the linear wave theory. Hayashi and Golder (1978) conducted several experiments with a GFDL GCM from which topography, midlatitude disturbances and condensational heating were eliminated one by one. Based upon space-time spectral analysis of the simulations, they found that Kelvin waves are hardly affected by the topography and the midlatitude disturbances.

Similar to that in the control experiment, the band-filtered precipitation rate (Figure 29b) oscillates nearly in phase with the geopotential height. Comparing these two figures, we find that well-defined Kelvin wave is accompanied by the occurrence of the band-

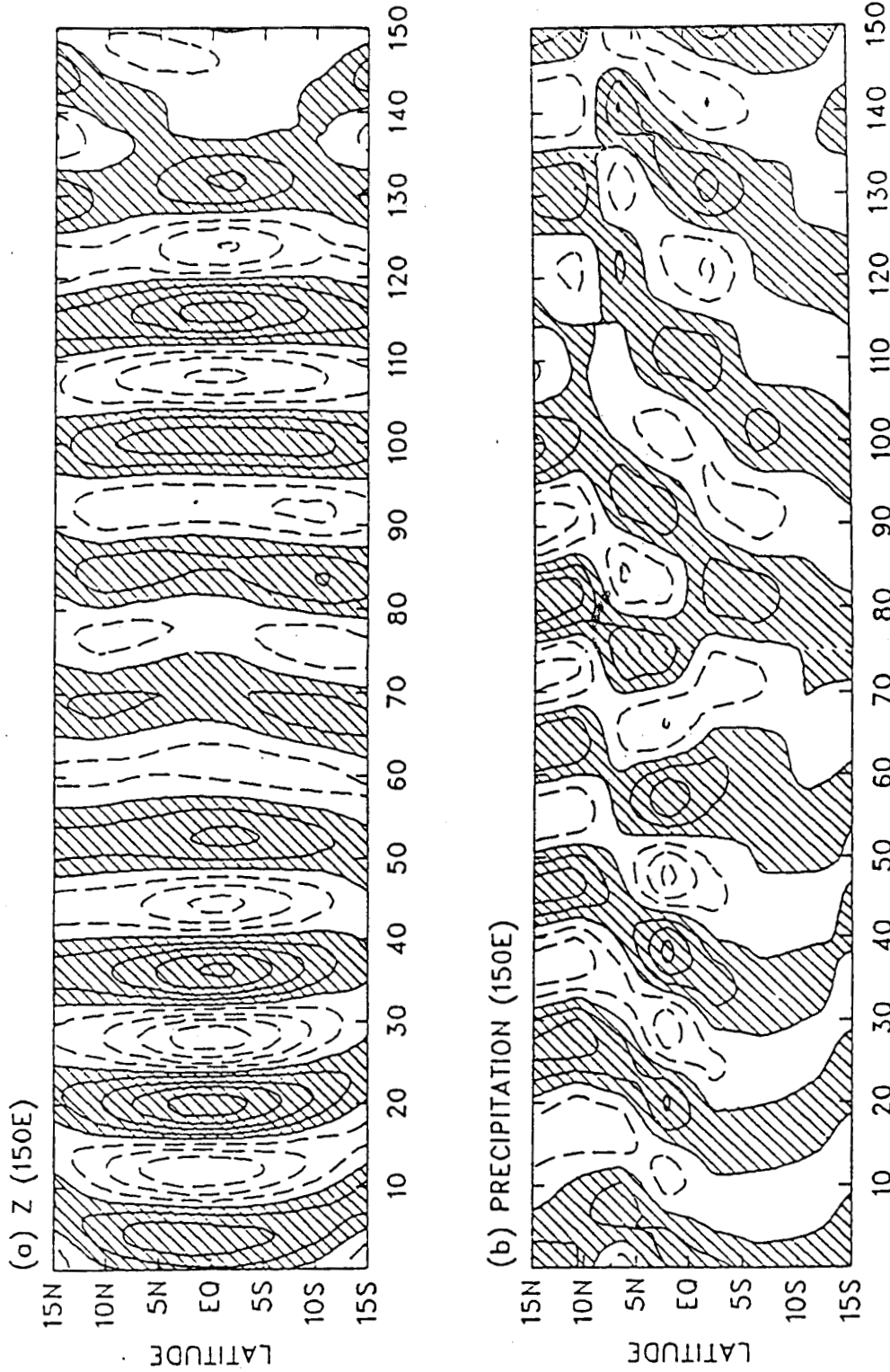


Figure 29. Same as Figure 7, except for the eastward moving periods of 15-20 days in the no-mountain experiment. Contour intervals is 3 m in (a), and 3 mm day⁻¹ in (b)

filtered precipitation peak near the equator. Therefore we conclude that removing mountains from the model has little effect on the generation of the Kelvin wave.

4. Maintenance of the Kelvin wave

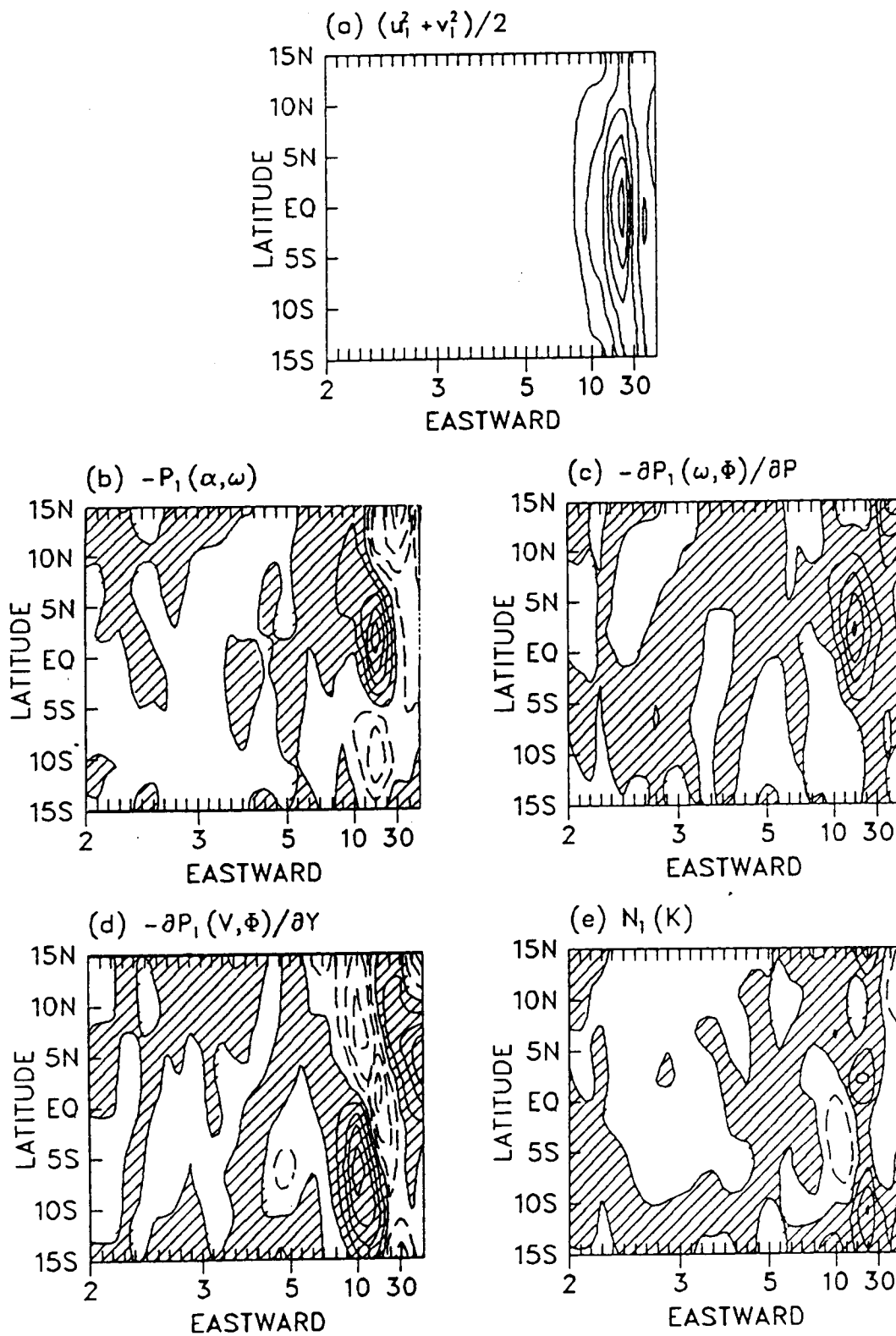
Figure 30 presents the energetic budget analysis for EMWs with $m=1$ at 200 mb. The kinetic energy of the EMWs is shown in Figure 30a. Clearly, there is a concentration of the kinetic energy in the period range of 10-60 days, while the maximum kinetic energy with a period of 20 days has a symmetric structure about the equator and decays away from the equator.

The conversion of available potential energy into kinetic energy (Figure 30b) for the EMWs with a period of about 12-30 days is significant, while appreciable positive conversion taking place between 5S to 7N indicates that the conversion of available potential energy generated by the latent heat release is an energy source for the maintenance of the Kelvin wave.

Similar to the conversion term, the vertical convergence of energy flux (Figure 30c) for the EMWs with a period of 12-30 days is significant between 5S and 8N.

Figure 30d shows the meridional convergence of wave energy flux. It is evident that the wave energy flux associated with the EMW in the period range of 12-30 days is transported poleward near the equator (diverges) and converges somewhere near 10° latitude away from the equator. This feature is consistent with that of the Kelvin wave in the control experiment.

Figure 30. Same as Figure 9, except for the no-mountain experiment. Contour intervals are 2 J in (a); and 10^{-5} W in (b), (c), (d) and (e)



ORIGINAL PAGE IS
OF POOR QUALITY

The nonlinear kinetic energy transfer is very weak over the whole spectrum except for the period band 15-20 days, with which the Kelvin wave gains kinetic energy between 15S and 15N through nonlinear interaction.

From the previous discussion, we find that eliminating mountains from the model hardly changes the maintenance of the Kelvin wave, except for the conversion of available potential energy into kinetic energy, which becomes important in the wave maintenance due to the elimination of mountains.

C. The No-cloud Experiment

The above analysis suggests that latent heat release associated with cumulus convection may be responsible for the generation of the Kelvin wave, since this wave appears even in the absence of mountains. In order to confirm this possibility, cumulus convection was eliminated from the model. As a result, a weakened Kelvin wave and a free Rossby wave were identified in the winter season.

1. Winter zonal-mean wind

Convective storm systems can transport meteorological properties vertically between the lower and upper troposphere and are important in maintaining the large-scale balance of angular momentum, energy, and moisture in midlatitudes. Ninomiya (1971) suggested that release of latent heat in convection systems is the primary factor that intensifies the upper-level large-scale flow through strengthening the horizontal temperature gradient. Since cumulus convective does not

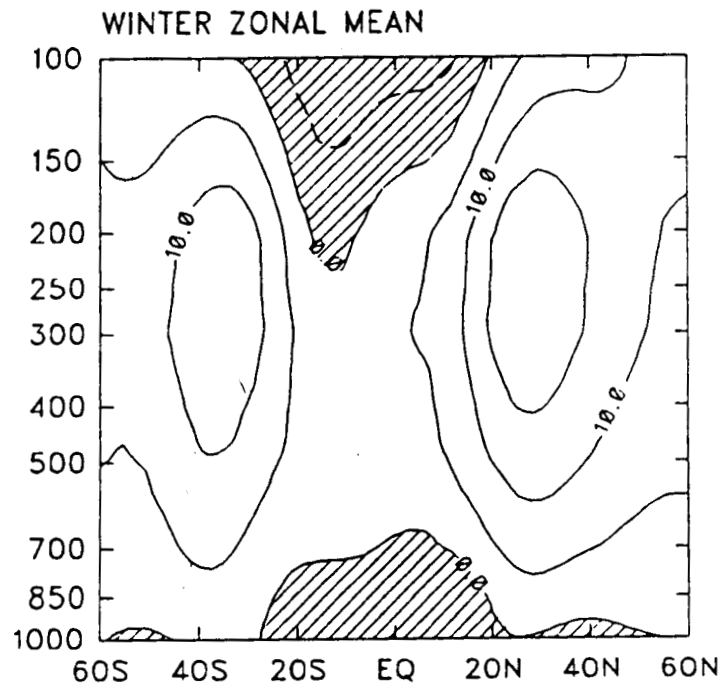


Figure 31. Same as Figure 2, except for the no-cloud experiment over the northern winter

exist in the no-cloud experiment, the vertical exchange of energy and moisture is significantly reduced. Figure 31 presents a height-latitude section of zonal mean wind averaged over the winter season. As expected, due to the restraint of latent heat release, radiative effects, surface and other energy balances, the intensity of the jet streams is decreased markedly and the jet cores are located more than 2 km lower than the height where they were situated in the control experiment.

2. Spectral analysis

Figure 32a shows power spectrum of u at 200 mb and 2S as a function of wavenumber and frequency. It is seen that $P(u)$ is more spread out in the wavenumber-frequency domain than in the control experiment. There are two spectral peaks at $m=1$ and eastward periods of 10-15 days and westward periods of 17-24 days.

Figures 31b and 31c display $P(z)$ and $P(u)$ associated with $m=1$ at 200 mb. It is evident that the power spectra EMWs are dominated by disturbances which are symmetric with respect to the equator and decay away from the equator. On the other hand, $P(z)$ for the WMWs is dominated by disturbances from extratropical areas in both hemispheres, while $P(u)$ for the WMWs has an appreciable peak at periods of 20-30 days on the equator. We also notice that the latitude-frequency power spectrum of v with $m=1$ does not have appreciable spectral peaks in the frequency bands corresponding to where spectral peaks of $P(u)$ are observed (not shown).

Shown in Figures 31d and 31e are the vertical structures of $P(z)$

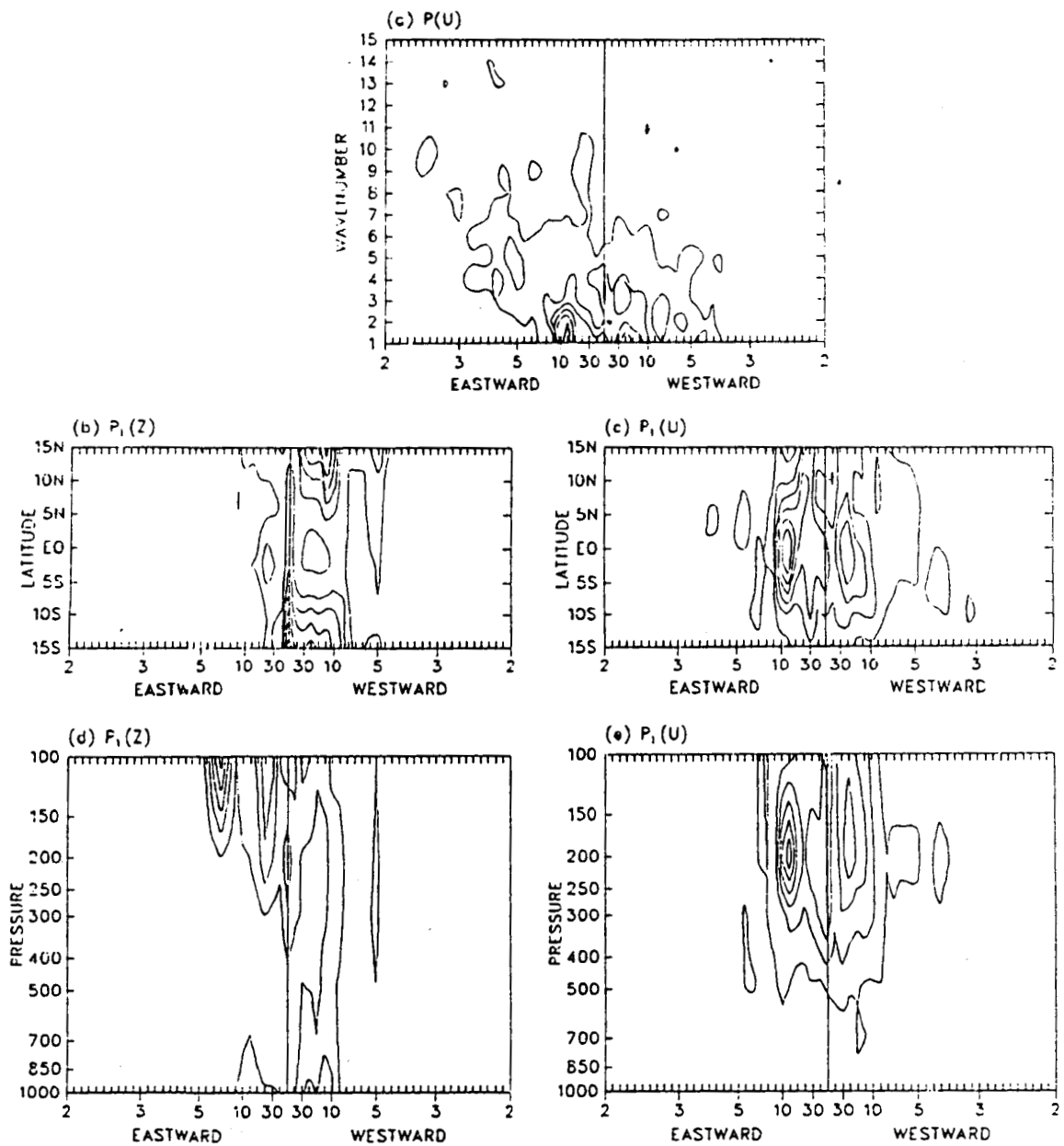


Figure 32. Same as Figure 3, except for the no-cloud experiment over the northern winter. Contour intervals are $1.5 \text{ m}^2 \text{ s}^{-2} \text{ day}$ in (a); $12 \text{ m}^2 \text{ day}$ in (b) and (d); and $1.5 \text{ m}^2 \text{ s}^{-2} \text{ day}$ in (c) and (e)

ORIGINAL PAGE IS
OF POOR QUALITY

and $P(u)$ with $m=1$ at 2S, respectively. It is evident that $P(z)$ is essentially dominated by EMWs. There are two spectral peaks with eastward periods of 6 days and 20 days locate above the 200 mb level. No significant spectral peak occurs at the period range of 10-15 days. However, $P(u)$ is dominated by the two spectral peaks which are observed in Figure 3lc at 200 mb.

3. Propagation characteristics

From the dispersion diagram associated with $m=1$ of the Laplace's tidal equation (Longuet-Higgins, 1968), we can estimate the equivalent depth of the spectral peak associated with the WMW with $m=1$ and a period of 17-24 days. For this peak, there are two possible locations on the dispersion diagram. The location may be either on the $n=1$ or the $n=3$ curve, where n is the latitudinal nodal number. Thus the wave associated with this peak can be interpreted as either 1) an equatorially trapped Rossby wave with $n=1$, or 2) a free Rossby wave with $n=3$. If the first interpretation is correct, the meridional velocity associated with the wave should reach a maximum at some latitude, which is estimated to be 17° , according to the dispersion diagram. However, the latitudinal distribution of $P(v)$ (not shown) increases poleward without showing a clear indication of the v maximum.

If we adopt the second interpretation, the estimated equivalent depth (8.4 km) is very close to the equivalent depth of free oscillations, and the gradual poleward decrease of $P(u)$ and the monotonic increase of $P(v)$ from the equator to 17° latitude are more

consistent with the theoretically predicted structure of the wave (Longuet-Higgins, 1968). The existence of the second gravest symmetric free Rossby mode with a period of 16-18 days has been reported by many authors [see Madden (1979) and Walkerscheid (1980) for reviews]. Therefore, this peak is identified as the second gravest symmetric free Rossby mode with $n=3$. In the following discussion we shall focus on the spectral peak associated with $m=1$ and periods of 10-15 days.

The spectral analysis indicates that the disturbance associated with $m=1$ and eastward moving periods of 10-15 days is a Kelvin wave. Figure 33 shows the horizontal distributions of geopotential height and wind components of the disturbance at 200 mb. The most striking feature is the reduction of both the wave amplitude and latitudinal extent, compared to those in the control experiment. The amplitude of geopotential height and zonal wind are about 3 m and 3 ms^{-1} , respectively. The latitudinal width is about 5° latitude. However, based upon linear wave theory which assumes the atmospheric Kelvin wave is a free wave, the latitudinal width and the vertical wavelength are estimated to be 16° latitude and 11 km (Table 3), respectively. The discrepancy between the model simulation and the linear theory predication for latitudinal width strongly suggests that the atmospheric Kelvin waves are forced waves instead of free wave modes.

Figure 34 shows a latitude-time section and a height-time section of the geopotential height oscillations with $m=1$ and periods of 10-15 days, respectively. In Figure 34a, the Kelvin wave with reduced

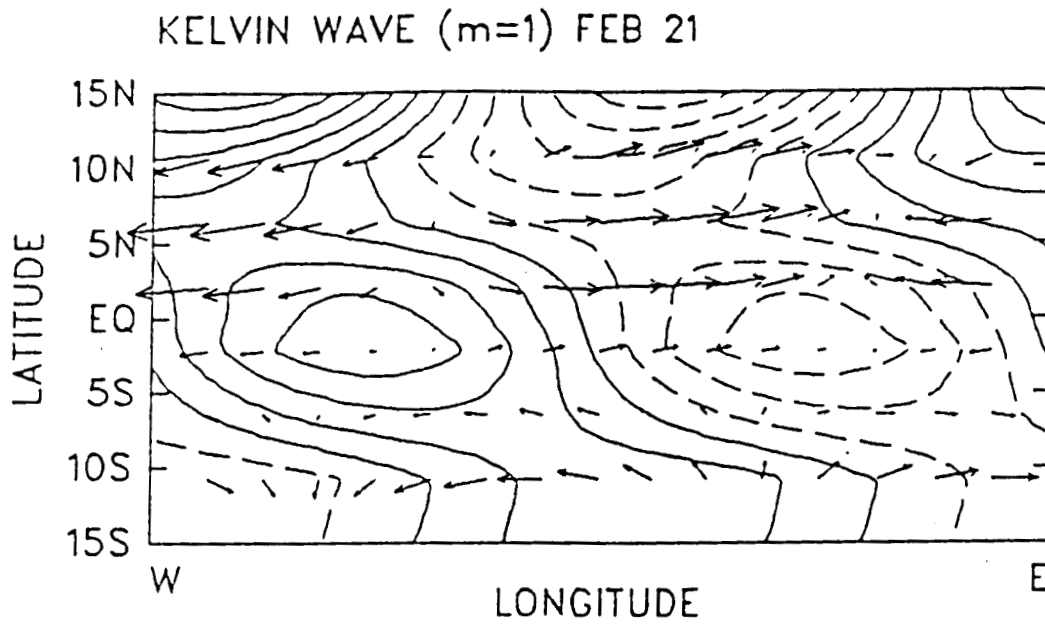
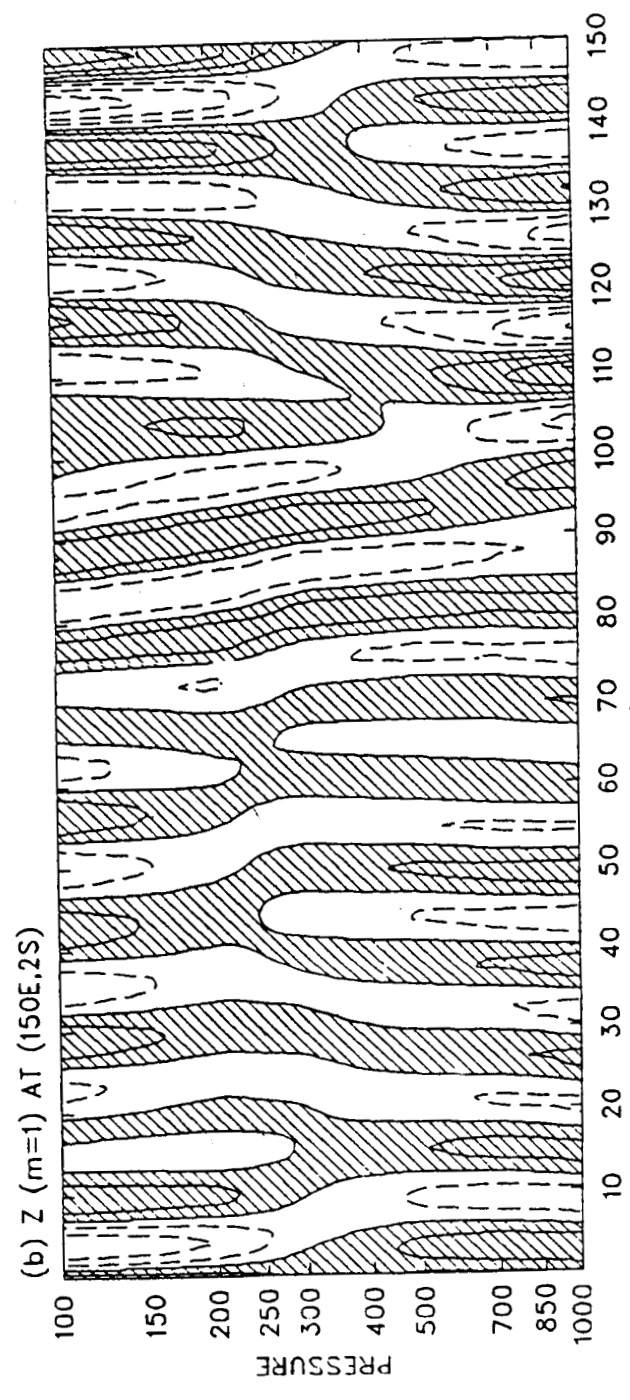
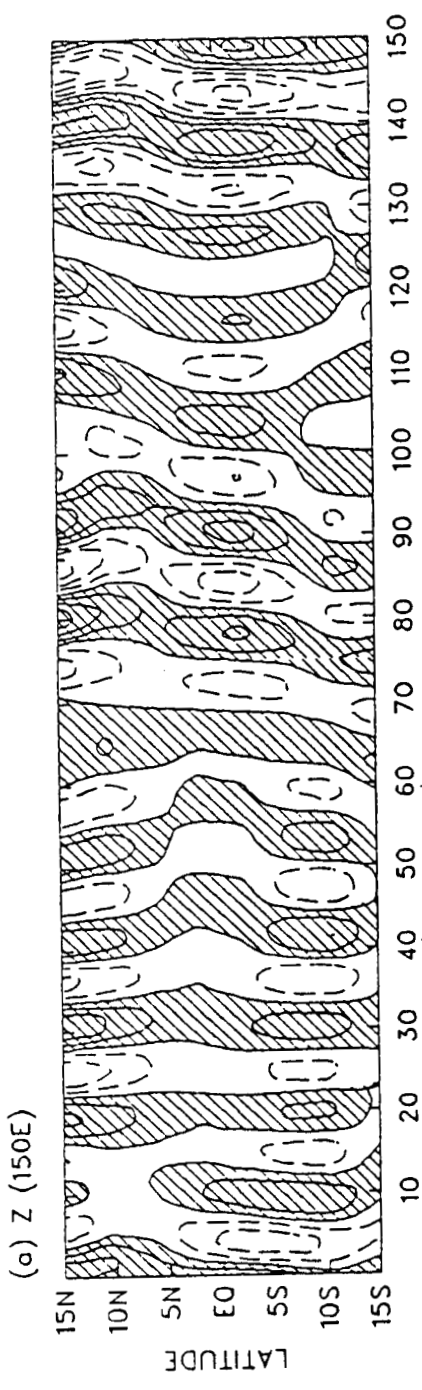


Figure 33. Same as Figure 4, except for the Kelvin wave with $m=1$ and periods of 10-15 days in no-cloud experiment. Contour interval is 1 m

Figure 34. Time evolutions of the Kelvin wave in the no-cloud experiment over the northern winter. (a) Latitude-time and (b) height-time cross sections of geopotential height with $m=1$ and eastward periods of 10-15 days. Contour intervals are 1.5 m and 2 m in (a) and (b), respectively



latitudinal extent is evident during days 70-110 and after day 135. Our results confirm that obtained by Hayashi and Golder (1978) who showed that the power of the Kelvin wave diminished drastically after condensational heat as well as midlatitude disturbances, was eliminated from the GCM they used. Thus, it is revealed that Kelvin waves may be generated due to the effect of latent heat release produced by cumulus convection in the troposphere.

The vertical structure of z at 150E longitude and 2S (Figure 34b) reveals a markedly downward phase progression accompanied by the appearance of the Kelvin wave (days 70-120). A noticeably reduced amplitude is clear, implying weaker upward energy propagation. Since clouds are not formed in this experiment, the solar radiation can reach the earth surface without being reflected back to space by the clouds. Therefore, the atmospheric circulations will be modified by the incoming solar radiation. Tzeng and Chen (1988) noted that three pronounced divergent centers in the no-cloud experiment appear at about 10S over the three tropical continents (the American, African, and maritime continents) in response to the landmass heating. However, thermally direct convections associated with the three divergent centers are not able to transport sufficient energy upward to stimulate the Kelvin wave in the absence of the cumulus convective process.

4. Maintenance of the Kelvin wave

Figure 35 presents energetic budget analysis for EMWs with $m=1$ at 200 mb. It is evident that the kinetic energy (Figure 35a) for those

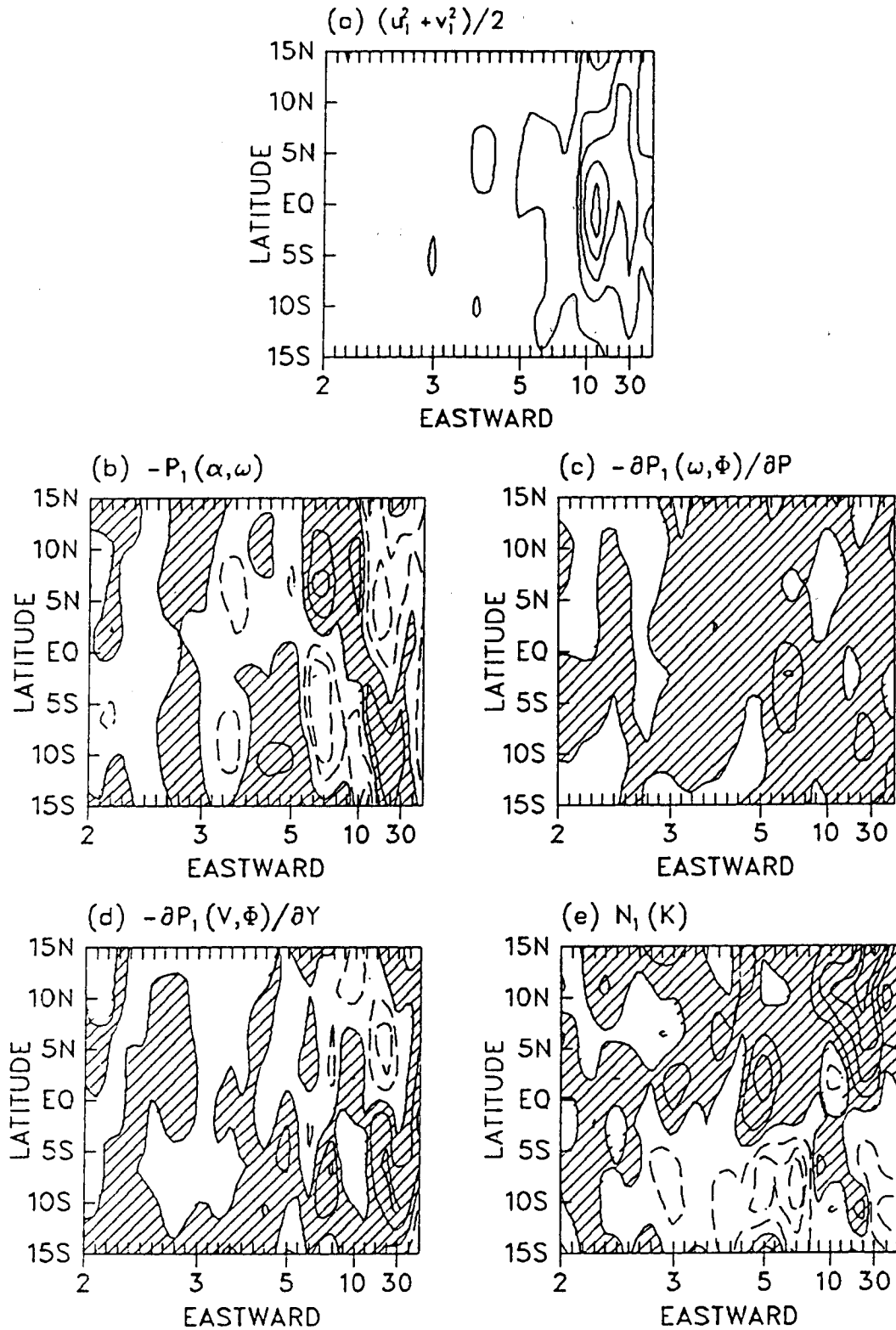
EMWs with periods of 10-30 days is significant. The maximum kinetic energy with a period of 10-15 days appears on the equator with an even structure about the equator.

The conversion of available potential energy to kinetic energy shown in Figure 35b is significant for the EMW with a period of about 6 days. However, over the period band of 10-15 days, with which the Kelvin wave is observed, the conversion is of less importance for the maintenance of the Kelvin wave. Only a weak positive conversion lying between the equator and 5S indicates less energy input into the Kelvin wave than that in the control experiment.

As expected, eliminating cumulus convection from the model will drastically suppress vertical transport of energy and moisture. It is not surprising to see that the vertical convergence of wave energy flux (Figure 35c) is almost negligible due to the reduction of vertical energy flux. Therefore, it reveals that the two primary energy sources of the Kelvin wave in the control experiment, the conversion of available potential energy to kinetic energy and the vertical convergence of wave energy flux generated by the cumulus convections in the tropics, are no longer able to provide sufficient energy to the Kelvin wave in this case.

In contrast to that in the control experiment, the Kelvin wave in the no-cloud case is not accompanied by meridional divergence of the wave energy flux due to the pressure work (Figure 35d). Weak divergence and convergence with a period of 12-15 days located on either side of the equator indicate that there is a weakly southward

Figure 35. Same as Figure 9, except for the no-cloud experiment over the northern winter. Contour intervals are 1 J in (a); and 10^{-5} w in (b), (c), (d) and (e)



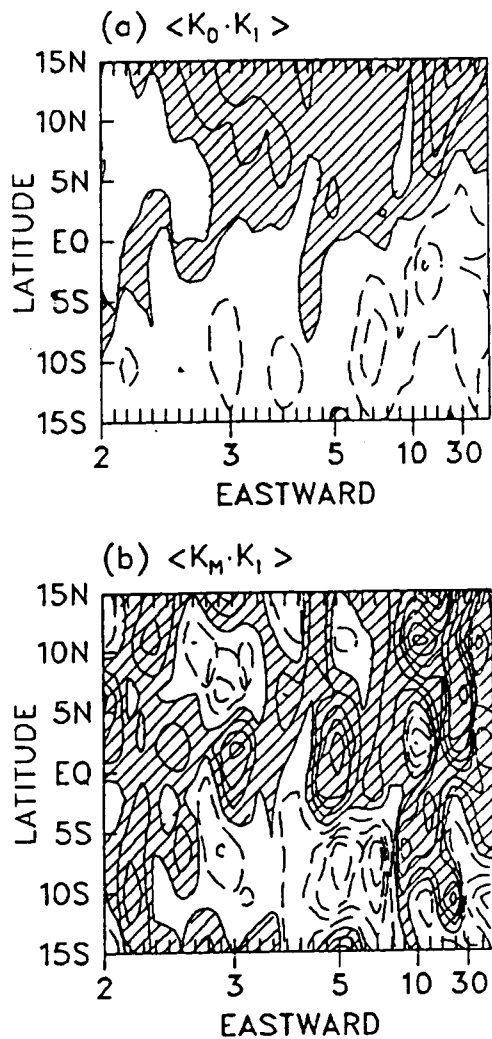


Figure 36. Same as Figure 10, except for the no-cloud experiment over the northern winter. Contour interval is 0.5×10^{-5}

W

ORIGINAL PAGE IS
OF POOR QUALITY

energy flux near the equator associated with the Kelvin wave.

As shown in Figure 35e, the nonlinear energy transfer is significant for the EMWs with periods of 4-6 days and 8-30 days. Separating the nonlinear energy transfer into wave-mean flow and wave-wave interaction, we find that the suppressed zonal flow weakens the wave-mean flow interaction as shown in Figure 36a. It is noteworthy that there is a weak kinetic energy input into EMWs with periods of 10-30 days north of 5N. On the other hand, enhanced energy transfer due to the wave-wave interaction is evident over the whole spectrum (Figure 36b). It is noted that EMWs with periods of 8-15 days, in which the Kelvin wave is observed, gain energy north of 5N and between the equator and 10S.

VI. CONCLUDING REMARKS

The equatorial planetary waves simulated by the NCAR CCM1 general circulation model have been investigated in terms of space-time spectral analysis (Kao, 1968; Hayashi, 1971, 1973) and energetic analysis (Hayashi, 1980). These analyses are particularly applied to grid-point data on latitude circles. In order to test some physical factors which may affect the generation of tropical transient planetary waves, three different model simulations with the CCM1 (the control, the no-mountain and the no-cloud experiments) have been analyzed.

A. Summary and Discussion

On the basis of the analyses of the three experiments, the identified equatorial planetary waves can be summarized as following:

1. Two Kelvin waves are identified in the summer of the control experiment, one at $m=1$ and an eastward propagating period of 18-25 days with a vertical wavelength of about 5.9 km, and the other at $m=2$ with an eastward moving period of 5-6 days and a vertical wavelength of 12 km. On the other hand, in the winter of the control experiment, the Kelvin wave with $m=2$ is absent and only the Kelvin wave with $m=1$ and a period of 15-20 days is found. The characteristics of these Kelvin waves are in agreement with observations by Zangvil and Yanai (1980) and Yanai and Lu (1983).
2. Kelvin waves at $m=1$ and with a period of 15-20 days, and at

$m=1$ and a period of 18-25 days are clearly identified in the summer and winter of the no-mountain experiment, respectively. The amplitudes and propagation characteristics of the Kelvin waves are hardly affected by the removal of mountains, compared to those in the control experiment.

3. The Kelvin wave at $m=1$ and with a period of 10-15 days is detected only in the winter of the no-cloud experiment. However, the amplitude and the north-south extent of the wave are significantly reduced, in agreement with the results obtained by Hayashi and Golder (1978).
4. A mixed Rossby-gravity wave is found with periods of 12-15 days for $m=5$ in the summer of the control experiment and has a vertical wavelength of about 3.3 km. The amplitude of the meridional wind associated with the wave is about 1 ms^{-1} . However, observations (Zangvil and Yanai, 1980; Yanai and Lu, 1983) reported the existence of a mixed Rossby-gravity wave with $m=4$ and a period of 5 days at 200 mb. On the other hand, this wave disappears completely in both the no-mountain and the no-cloud experiments.
5. A equatorially trapped Rossby wave associated with a 20-30 day period for $m=3$ and a vertical wavelength of about 14 km is observed in the winter of the control experiment. However, observed equatorially trapped Rossby waves are found at $m=2$ and with periods of 10 days and 30 days, respectively. This wave is absent in both the no-mountain and the no-cloud

experiments.

6. In addition, the next gravest symmetric free Rossby wave at $m=1$ and with westward period of 17-24 days is detected in the no-cloud experiment.

Based upon the energetic analyses, the physical processes which are important in maintaining the identified equatorial waves in the present study are showed in Table 4. The maintenance of the waves can be summarized as following:

1. The two primary energy sources for maintenance of the Kelvin waves, the mixed Rossby-gravity wave and the equatorially trapped Rossby wave wave modes at 200 mb are the conversion of available potential energy to kinetic energy and the vertical convergence of wave energy flux. The Kelvin waves are accompanied by a meridional divergence of wave energy flux near the equator, while the mixed Rossby-gravity wave and the equatorially trapped Rossby wave are associated with meridional convergence of wave energy flux. The latter finding suggests that these westward moving waves may be excited by the pressure work due to midlatitude disturbances, i.e., the lateral forcing.
2. The two primary energy sources in both the control and the no-mountain experiments are weakened markedly in the no-cloud experiment. The vertical energy flux is especially negligible, while the meridional wave energy flux associated with the Kelvin wave is weakly southward instead of converging

Table 4. Various physical processes associated with wave maintenance

Case	Season	Wave	m	$-P(\alpha, \omega)$	$-\frac{\partial P(\phi, \omega)}{\partial p}$	$-\frac{\partial P(\phi, v)}{\partial y}$	N(k)
Control	summer	Kelvin wave	1		*	*	
		Kelvin wave	2		*	*	
	mixed Rossby-gravity wave	5		*	*	*	
	winter	Kelvin wave	1	*	*	*	*
		Rosby wave	3	*	*	*	*
No-mountain	summer	Kelvin wave	1	*	*	*	
	winter	Kelvin wave	1	*	*	*	*
No-cloud	winter	Kelvin wave	1				*
		Free Rossby wave	1				

^aThe corresponding physical process which is important in maintaining the wave.

on the equator.

3. The nonlinear energy transfer associated with the Kelvin waves is of less importance compared to that associated with the mixed Rossby-gravity wave and the Rossby wave. The kinetic energy transfer through the nonlinear interaction appears to be more important in the winter than in the summer.
4. Our results indicate that the linear waves theory is still valid even though the nonlinear effect may slightly change the frequencies and the structures of the equatorial waves.

Tsay (1974) showed that the Kelvin wave in the NCAR GCM is accompanied by meridional energy convergence between 12 km and 18 km over the equator. However, our results show that the Kelvin waves in the CCM1 are associated with meridional energy divergence near 200 mb, which is in agreement with observation by Yanai and Lu (1983).

The spectral analysis of the model precipitation rate gives a stochastic distribution in the wavenumber-frequency domain. On the other hand, there are high correlations between Kelvin waves and the band-filtered precipitation rate that is symmetric about the equator, and between the mixed Rossby-gravity wave and the band-filtered precipitation rate that exhibits an antisymmetric structure with respect to the equator. This finding confirms Holton's random thermal forcing theory, which states that the frequencies of the Kelvin wave and the mixed Rossby-gravity wave are determined by a certain filtering effect of the atmosphere and not by the wavenumber-frequency

distribution of the heating function. In the same sense, the fluctuations of the Kelvin waves and the mixed Rossby-gravity waves in the present study are more accurately characterized as episodic, rather than steady oscillations (Salby et al., 1984). This can be interpreted as both waves originating in the stochastic latent heat release of troposphere cloud ensembles.

The band-filtered precipitation rate is highly correlated with the Kelvin waves and the mixed Rossby-gravity wave at 150E longitude, at which the strongest divergent center is located (Tzeng and Chen, 1988), indicating that the cumulus convective process in this region is responsible for transporting energy from lower levels to upper levels in order to maintain the waves.

B. Deficiencies of the Model Simulations

In view of these model simulations, we find that the NCAR CCM1 can simulate equatorial planetary waves well to a certain extent; in particular, the Kelvin waves have been simulated successfully. We believe the reasons for this success are rooted the treatment of cumulus convection and the different parameterization schemes.

The difference between the model simulations and observations is that the simulated WWs tends to have smaller horizontal wavelenghts. A possible factor causing the defect could be the coarse resolution of the model ($m=15$).

Comparing with the vertical propagation behavior of Kelvin waves above the tropopause (Salby et al., 1984; Hayashi et al., 1984), we note that the vertical structures of the Kelvin waves exhibit little

vertical phase tilt in the troposphere, but a vertical phase change of 180 near 500 mb. This discrepancy can be explained in terms of the near-field behavior of Kelvin waves as discussed by Salby and Garcia (1987). Based upon a set of linearized primitive equations in spherical geometry, they showed that the Kelvin response arising from a heating centered on the equator in the upper troposphere is characterized by a 180° phase change in the vertical before radiating entirely out of the troposphere.

On the other hand, the model's top boundary may affect Kelvin waves significantly. Comparing two model simulations by the CCM with different top levels (at 0.1 mb and 10 mb), Boville and Cheng (1988) found that Kelvin waves in the model with the top level at 10 mb are reflected by the top boundary and become vertically standing oscillations which retain approximately their original zonal phase speed.

C. Suggestions for Future Study

In the present study, we treated equatorial transient waves as the fundamental solutions of a zonally symmetric basic state predicted by linear wave theory. However, the consideration of waves in a nonzero, zonally asymmetric basic state has been proven to be important to climate dynamics. Webster and Chang (1988) proposed that the longitudinal asymmetry of the basic flow in the tropics so alters the characteristics of equatorially trapped modes that their Doppler-shifted group speed becomes locally zero, producing a local convergence of energy to the east of the equatorial westerlies. We

plan to extend our study by taking into account zonally asymmetric states. By doing this, we may be able to investigate the wave transition between the region of easterlies and westerlies along the equator, and test whether or not the transition occurs as an evolution of the latitudinal modal structure of the equatorial modes as the modes propagate from an ostensibly easterly regime to a energy accumulation point within the westerlies.

VII. REFERENCES

- Alexander, R. C., and R. L. Mobley. 1976. Monthly average sea-surface temperature and ice-pack limits on a 1° global grid. *Mon. Wea. Rev.* 104: 143-148.
- Arkin, P. A. 1982. The relationship between interannual variability in the 200mb tropical wind field and Southern Oscillation. *Mon. Wea. Rev.* 110: 1393-1404.
- Asselin, R. 1972. Frequency filter for time integrations. *Mon. Wea. Rev.* 100: 487-490.
- Bath, M. 1974. Spectral analysis in geophysics. Elsevier Scientific Publishing Company, New York.
- Bendat, J. S., and A. G. Piersol. 1971. Random data: Analysis and measurement procedures. Wiley-Interscience, New York.
- Bennett, J. R., and J. A. Young. 1971. The influence of latitudinal wind shear upon large-scale wave propagation into the tropics. *Mon. Wea. Rev.* 99: 202-214.
- Blackmon, M. L., G. W. Branstator, and G. T. Bates. 1987. An analysis of equatorial Pacific sea surface temperature anomaly experiments in general circulation model with and without mountains. *J. Atmos. Sci.* 44: 1828-1824.
- Bourke, W. 1974. A multi-level spectral model. I. Formulation and hemispheric integrations. *Mon. Wea. Rev.* 102: 687-701.
- Bourke, W., B. McAvaney, K. Puri, and R. Thurling. 1977. Global modeling of atmospheric flow by spectral methods. Pp. 267-324 in *Methods of Computational Physics*. Vol. 17. General Circulation Models of the Atmosphere. Academic Press, New York.
- Boville, B. A., and X. Cheng. 1988. Upper boundary effects in a general circulation model. *J. Atmos. Sci.* (to be published)
- Bretherton, F. P. 1964. Low frequency oscillations trapped near the equator. *Tellus* 16: 181-185.
- Burridge, D. M., and J. Haseler. 1977. A model for medium range weather forecasting - adiabatic formulation. ECMWF Technical Report No. 4.
- Chang, C. P. 1977. Viscous internal gravity waves and low-frequency oscillations in the tropics. *J. Atmos. Sci.* 34:

901-910.

- Charney, J. G. 1969. A further note on large-scale motions in the tropics. *J. Atmos. Sci.* 26: 182-185.
- Chen, T. -C. 1985. Global water vapor flux and maintenance during FGGE. *Mon. Wea. Rev.* 113: 1801-1819.
- Chen, T. -C. and W. E. Baker. 1986. Global diabatic heating during FGGE SOP-1 and SOP-2. *Mon. Wea. Rev.* 114: 2578-2589.
- Chen, T. -C. and H. van Loon. 1987. Interannual variation of the tropical easterly jet. *Mon. Wea. Rev.* 115: 1739-1759.
- Daley, R. C., C. Girard, J. Henderson, and I. Simmonds. 1976. Short-term forecasting with a multi-level spectral primitive equation model. Part I-Model Formulation. *Atmosphere* 14: 98-116.
- Diky, L. A., and G. S. Golitsyn. 1968. Calculation of the Rossby wave velocities in the earth's atmosphere. *Tellus* 20: 314-317.
- Donner, L. J., H. -L. Kuo, and E. J. Pitcher. 1982. The significance of thermodynamic forcing by cumulus convection in a general circulation model. *J. Atmos. Sci.* 39: 2159-2181.
- Dunkerton, T. 1979. On the role of the Kelvin waves in the westerly phase of the semiannual zonal wind oscillation. *J. Atmos. Sci.* 36: 32-41.
- Dunkerton, T. 1982. Theory of the mesopause semiannual oscillation. *J. Atmos. Sci.* 39: 2681-2690.
- Gruber, A. 1975. The wavenumber-frequency spectra of the 200mb wind field in the tropics. *J. Atmos. Sci.* 32: 1615-1625.
- Hahn, D. G., and S. Manabe. 1975. The role of maintains in the South Asian monsoon circulation. *J. Atmos. Sci.* 32: 1515-1541.
- Hayashi, Y. 1970. A theory of large-scale equatorial waves generated by condensation heat and accelerating the zonal wind. *J. Meteorol. Soc. Japan* 48: 140-160.
- Hayashi, Y. 1971. A generalized method of resolving disturbances into progressive and retrogressive wave by space Fourier and time cross-spectral analyses. *J. Meteorol. Soc. Japan* 49: 125-128.

- Hayashi, Y. 1973. A method of analyzing transient waves by space-time cross spectra. *J. Appl. Meteorol.* 12: 404-408.
- Hayashi, Y. 1974. Spectral analysis of tropical disturbances appearing in a GFDL general circulation model. *J. Atmos. Sci.* 31: 180-218.
- Hayashi, Y. 1976. Non-singular resonance of equatorial waves under the radiation condition. *J. Atmos. Sci.* 33: 183-201.
- Hayashi, Y. 1980. Estimation of nonlinear energy transfer spectra by the cross-spectral method. *J. Atmos. Sci.* 37: 299-307.
- Hayashi, Y., and D. G. Golder. 1978. The generation of equatorial transient planetary waves: Control experiments with a GFDL general circulation model. *J. Atmos. Sci.* 35: 2068-2082.
- Hayashi, Y., D. G. Golder, and J. D. Mahlman. 1984. Stratospheric and Mesospheric Kelvin waves simulated by the GFDL "SKYHI" general circulation model. *J. Atmos. Sci.* 41: 1971-1984.
- Hayashi, Y. and A. Sumi. 1986. The 30-40 day oscillations simulated in an "aqua planet" model. *J. Meteorol. Soc. Japan* 64: 451-467.
- Held, I. M. 1983. Stationary and quasi-stationary eddies in the extratropical troposphere: Theory. Pp. 127-168 in *Large-Scale Dynamical Processes in the Atmosphere*. Academic Press, London.
- Hirota, I. 1978. Equatorial waves in the upper stratosphere and mesosphere in relation to the semiannual oscillation of the zonal wind. *J. Atmos. Sci.* 35: 714-722.
- Hirota, I. 1979. Kelvin waves in the equatorial middle atmosphere observed by the Nimbus 5-SCR. *J. Atmos. Sci.* 36: 217-222.
- Holton, J. R. 1972. Waves in the equatorial stratosphere generated by tropospheric heat sources. *J. Atmos. Sci.* 29: 368-375.
- Holton, J. R. 1973. On the frequency distribution of atmospheric Kelvin wave. *J. Atmos. Sci.* 30: 499-501.
- Holton, J. R. 1975. The dynamic meteorology of stratosphere and

- mesosphere. Am. Meteorol. Soc., Boston.
- Holton, J. R. 1979. An introduction to dynamic meteorology. Academic Press, New York.
- Holton, J. R., and R. S. Lindzen. 1968. A note on "Kelvin" waves in the atmosphere. Mon. Wea. Rev. 96: 385-386.
- Hoskins, B. J., and A. J. Simmons. 1975. A multi-layer spectral model and the semi-implicit method. Q. J. Roy. Meteorol. Soc. 101: 637-655.
- Itoh, H., and M. Ghil. 1988. The generation mechanism of mixed Rossby-gravity waves in the equatorial troposphere. J. Atmos. Sci. 45: 585-601.
- Kao, S. K. 1968. Governing equations and spectra for atmospheric motion and transports in frequency-wavenumber space. J. Atmos. Sci. 25: 32-38.
- Kasahara, A., T. Sasamori, and W. M. Washington. 1973. Simulation experiments with a 12-layer stratospheric global circulation model. I. Dynamical effect of the earth's orography and thermal influence of continentality. J. Atmos. Sci. 30: 1229-1250.
- Kousky, V. E., and J. M. Wallace. 1971. On the interaction between Kelvin waves and the mean zonal flow. J. Atmos. Sci. 28: 162-169.
- Kuo, H. K. 1975. Instability theory of large-scale disturbances in the tropics. J. Atmos. Sci. 32: 2229-2245.
- Lau, K. -M., and L. Peng. 1987. Origin of low-frequency (Intraseasonal) oscillations in the tropical Atmosphere. Part I: Basic theory. J. Atmos. Sci. 44: 950-972.
- Liebman, B., and K. L. Hartman. 1981. Interannual variation of outgoing IR association with tropical circulation changes during 1974-78. J. Atmos. Sci. 28: 1158-1162.
- Lindzen, R. 1967. Planetary waves on beta-plaves. Mon. Wea. Rev. 95: 441-451.
- Lindzen, R., and J. R. Holton. 1968. A theory of the quasi-biennial oscillation. J. Atmos. Sci. 25: 1095-1107.
- Lindzen, R., and T. Matsuno. 1968. On the nature of large-scale wave disturbances in the equatorial lower stratosphere. J. Meteorol. Soc. Japan 46: 215-221.

- Longuet-Higgins, M. S. 1968. The eigenfunctions of Laplace's tidal equations over a sphere. *Phil. Trans. Roy. Soc. London*, A262: 511-607.
- Machenbauer, B. 1979. The spectral method. Pp. 121-275 in *Numerical Methods Used in Atmospheric Models*. GARP Publication Series 17. WMO, Geneva, Switzerland.
- Madden, R. A. 1979. Observations of large-scale travelling Rossby-wave. *Rev. Geophys. Space Phys.* 17: 1935-1949.
- Madden, R. A., and P. R. Julian. 1971. Detection of a 40-50 day oscillation in the zonal wind in the tropical Pacific. *J. Atmos. Sci.* 28: 702-708.
- Madden, R. A., and P. R. Julian. 1972. Description of global scale circulation cells in the tropics with 40-50 day period. *J. Atmos. Sci.* 29: 1109-1123.
- Mak, M. K. 1969. Laterally driver stochastic motions in the tropics. *J. Atmos. Sci.* 26: 41-64.
- Manabe, S., and T. B. Terpstra. 1974. The effects of mountains on the general circulation of the atmosphere as identified by numerical experiments. *J. Atmos. Sci.* 31: 3-41.
- Manabe, S., J. L. Holloway, Jr., and H. M. Stone. 1970. Tropical circulation in a time-integrate of a global model of the atmosphere. *J. Atmos. Sci.* 27: 580-613.
- Manabe, S., J. S. Samagorinsky, and R. F. Strickler. 1965. Simulated climatology of a general circulation model with hydrological cycle. *Mon. Wea. Rev.* 93: 769-798.
- Maruyama, T. 1967. Large scale disturbances in the equatorial lower stratosphere. *J. Meteorol. Soc. Japan* 45: 391-408.
- Maruyama, T. 1968a. Time sequences of power spectra of disturbances in the equatorial lower stratosphere in relation to the quasi-biennial oscillation. *J. Meteorol. Soc. Japan* 46: 327-342.
- Maruyama, T. 1968b. Upward transport of westerly momentum due to large-scale disturbances in the equatorial lower stratosphere. *J. Meteorol. Soc. Japan* 46: 404-417.
- Maruyama, T., and M. Yanai. 1967. Evidence of large scale wave disturbances in the equatorial lower stratosphere. *J. Meteorol. Soc. Japan* 45: 195-196.

- Matsuno, T. 1966. Quasi-Geostrophic motions in the equatorial area. *J. Meteorol. Soc. Japan* 44: 25-42.
- McAvaney, B. J., W. Bourke and K. Puri. 1978. A global spectral model for simulation of the general circulation. *J. Atmos. Sci.* 35: 1557-1583.
- Mintz, Y. 1965. Very long-term global integration of the primitive equations of atmospheric motion. *WMO Tech. Note* No. 66: 141-167.
- Murakami, J. 1972. Equatorial Stratospheric waves induced by diabatic heat sources. *J. Atmos. Sci.* 29: 1129-1137.
- Murakami, M. 1974. Influence of mid-latitude planetary waves on the tropics under the existence of critical latitude. *J. Meteorol. Soc. Japan* 52: 261-272.
- Newell, R. E., J. W. Kidson, D. G. Vincent and G. J. Boer. 1972. The general circulation of the tropical atmosphere and interactions with extratropical. Vol. 2. The MIT Press, Cambridge, Mass.
- Ninomiya, K. 1971. Dynamical analysis of outflow from tornado producing thunderstorms as revealed by ATS III pictures. *J. Appl. Meteorol.* 10: 275-294.
- Nitta, T. 1970. A study of generation and conversion of eddy available potential energy in the tropics. *J. Meteorol. Soc. Japan* 48: 524-528.
- Nitta, T. 1972. Structure of wave disturbances over the Marshall Islands during the years of 1956 and 1958. *J. Meteorol. Soc. Japan* 50: 85-103.
- Phillips, N. A. 1957. A coordinate system having some special advantage for numerical forecasting. *J. Meteorol.* 14: 184-185.
- Pitcher, E., R. C. Malone, V. Ramanathan, M.L. Blackmon, K. Puri, and W. Bourke. 1983. January and July simulation with a spectral general circulation mode. *J. Atmos. Sci.* 40: 580-604.
- Ramanathan, V., E. J. Pitcher, R. C. Malone, and M. L. Blackmon. 1983. The response of a spectral general circulation model to refinements in radiative processes. *J. Atmos. Sci.* 40:605-630.

- Reed, R. J. 1960. The circulation of the stratosphere. Paper presented at the 40th anniversary meeting of the Am. Meteorol. Soc., Boston, January 1960.
- Robert, A. J. 1966. The integration of a low order spectral form of the primitive meteorological equations. J. Meteorol. Soc. Japan 44:237-245.
- Rosenthal, S. L. 1960. Some estimates of the power spectra of large-scale disturbances in low latitudes. J. Meteorol. 17: 259-263.
- Sadler, J. C. 1970. Mean cloudiness and gradient level wind chart over the tropics. Six Weather Service Tech. Rep. 215. Vol. 2, 60pp.
- Salby, M. L. and R. R. Garcia. 1987. Transient response to localized episodic heating in the tropics, Part I: Excitation and short-time near-field behavior. J. Atmos. Sci. 44: 458-498.
- Salby, M., D. L. Hartmann, P. L. Bailey, and J. C. Gille. 1984. Evidence for equatorial Kelvin modes in Nimbus-7 LIMS. J. Atmos. Sci. 41: 220-235.
- Smagorinsky, J., S. Manabe, and J. L. Holloway, Jr. 1965. Numerical results from a nine-level general circulation model of the atmosphere. Mon. Wea. Rev. 93: 727-768.
- Stern, M. E. 1963. Trapping of low frequency oscillations in an equatorial boundary layer. Tellus 15: 246-250.
- Tsay, C. 1974. Analysis of large-scale wave disturbances in the tropics simulated by an NCAR global circulation model. J. Atmos. Sci. 31: 330-339.
- Tzeng, R. -Y., and T. -C., Chen. 1988. A study of the maintenance and annual variation of subtropical jet streams with the NCAR community climate model: Effects of mountain, cumulus convection and parameterization scheme of cumulus convection. Iowa State University Technical Report.
- Walkerscheid, R. L. 1980. Traveling planetary wave in the stratosphere. Pure Appl. Geophys. 18: 240-265.
- Wallace, J. M. 1973. General circulation of the tropical lower stratosphere. Rev. Geophys. Space Phys. 11: 191-222.
- Wallace, J. M., and V. E. Rousky. 1968. Observation evidence of Kelvin waves in the tropical stratosphere. J. Atmos. Sci.

5: 900-907.

- Webster, J. W., and H. -R., Chang. 1988. Equatorial energy accumulation and emanation regions: impacts of a zonally varying basic state. *J. Atmos. Sci.* 45: 803-828.
- Williamson, D. L., J. T. Kiehl, V. Ramanathan, R. E. Dickinson, and J. J. Hack. 1987. Description of NCAR Community Climate Model (CCML). NCAR/TN-285+STR, NCAR, Boulder, Colorado.
- Yanai, M. 1963. A preliminary survey of large-scale disturbances over the tropical Pacific region. *Geofits. Int.* 3: 73-84.
- Yanai, M., and T. Hayashi. 1969. Large-scale equatorial waves penetrating from the upper troposphere into the lower stratosphere. *J. Meteorol. Soc. Japan* 47: 167-182.
- Yanai, M., and M. Lu. 1983. Equatorially trapped waves at 200mb level and their association with meridional convergence of wave energy flux. *J. Atmos. Sci.* 40: 2785-2803.
- Yanai, M., and T. Maruyama. 1966. Stratospheric wave disturbances propagating over the equatorial Pacific. *J. Meteorol. Soc. Japan* 44: 291-294.
- Yanai, M., and M. Murakami. 1970. Spectrum analysis of symmetric and antisymmetric equatorial waves. *J. Meteorol. Soc. Japan* 48: 331-347.
- Yanai, M., T. Maruyama, Tsuyoshi Nitta and Y. Hayashi. 1968. Power spectra of large-scale disturbances over the tropical Pacific. *J. Meteorol. Soc. Japan* 46: 308-323.
- Zangvil, A., and M. Yanai. 1980. Upper tropospheric waves in the tropics. Part I: Dynamical analysis in the wavenumber frequency domain. *J. Atmos. Sci.* 37: 283-298.
- Zangvil, A., and M. Yanai. 1981. Upper tropospheric waves in the tropics. Part II: Association with clouds in the wavenumber-frequency domain. *J. Atmos. Sci.* 38: 939-953.

VIII. ACKNOWLEDGMENTS

Thanks go to Dr. Yen-Huei Lee who made the history tapes of the CCM1 experiments available for this study at the National Center for Atmospheric Research, to Ms. Cathryn L. Bronakowski and Ms. Gloria Manney for editing and proofreading. This study was jointly supported by the National Science Foundation under Grant ATM-8611476 and the National Aeronautics and Space Administration under Grant NAG5-355. The computations were performed on the CRAY-1 and CRAY-XMP computers of the National Center for Atmospheric Research, which is sponsored by the National Science Foundation.

APPENDIX

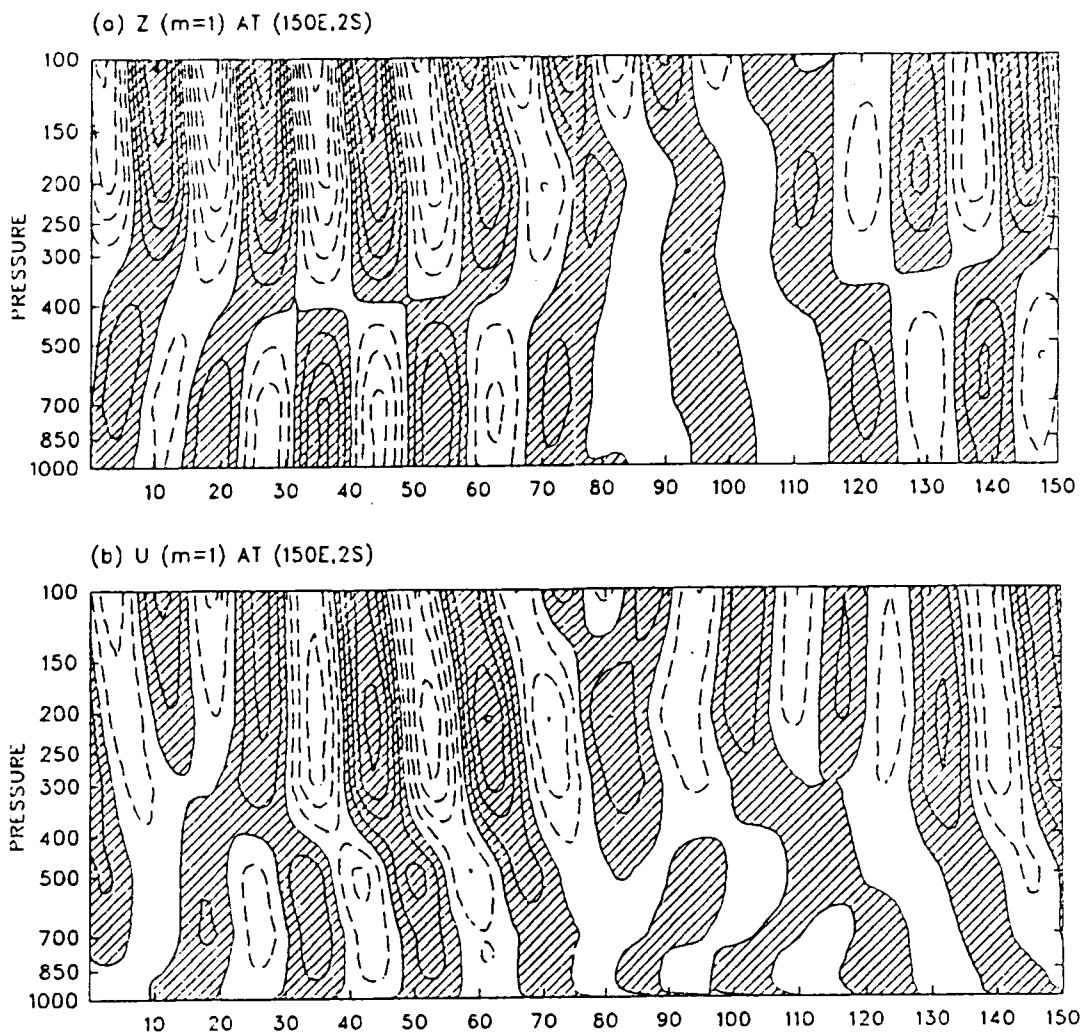


Figure A1. Same as Figure 5, except for the Kelvin wave with $m=1$ and periods of 15–20 days over the northern winter

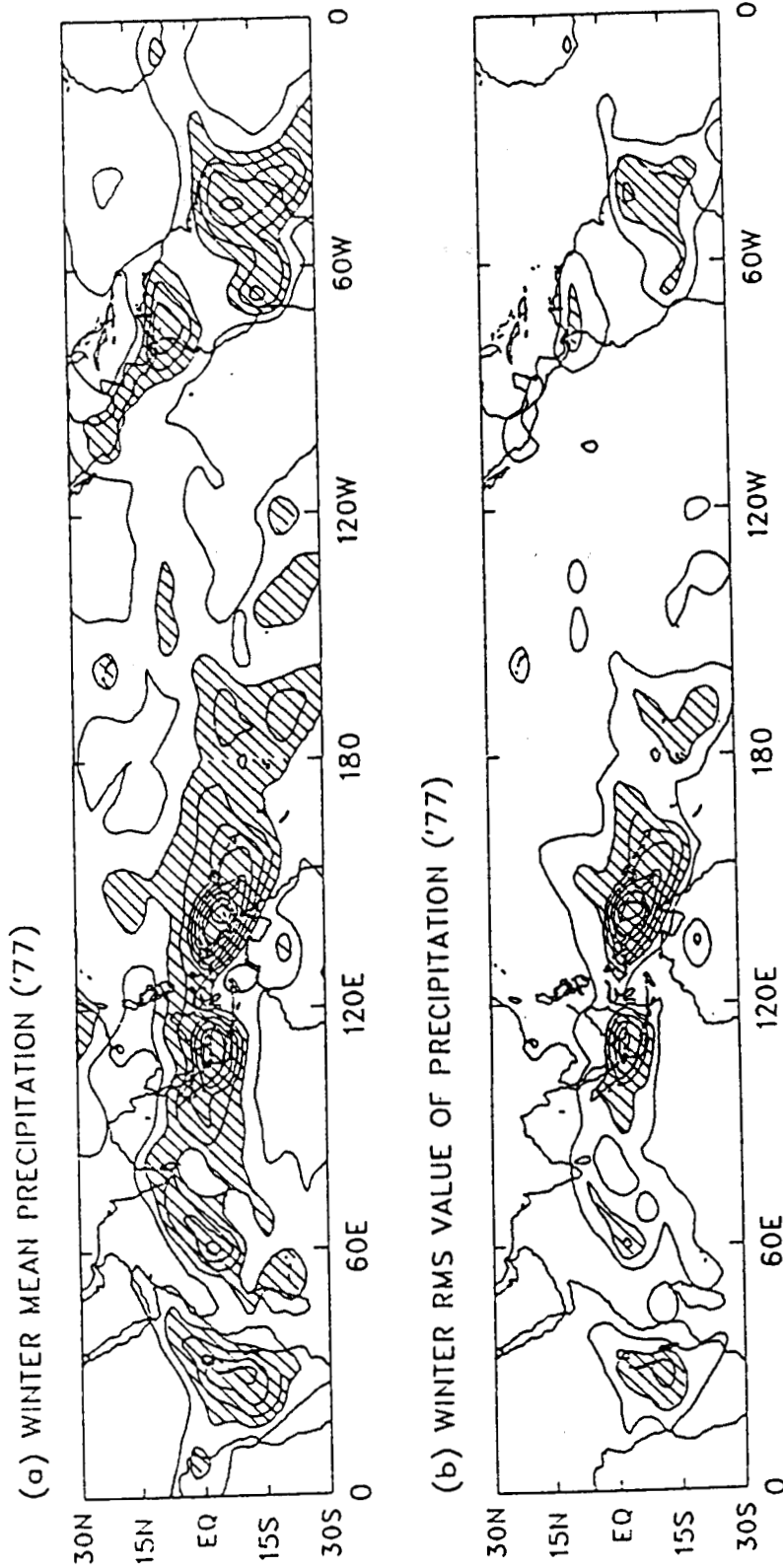


Figure 12. Same as Figure 6, except for the northern winter

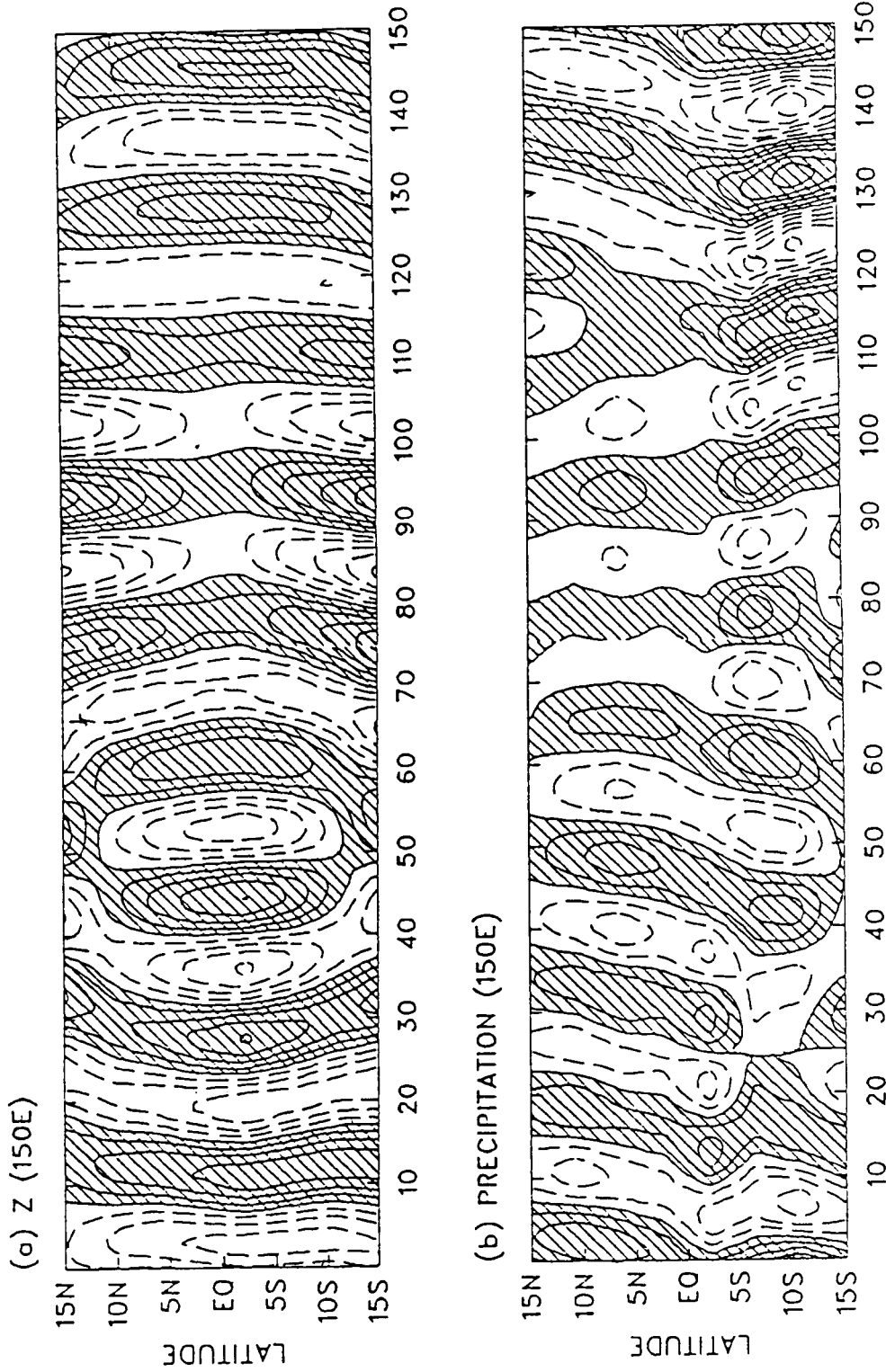


Figure A3. Same as Figure 7, except for the eastward moving periods of 15-20 days over the northern winter

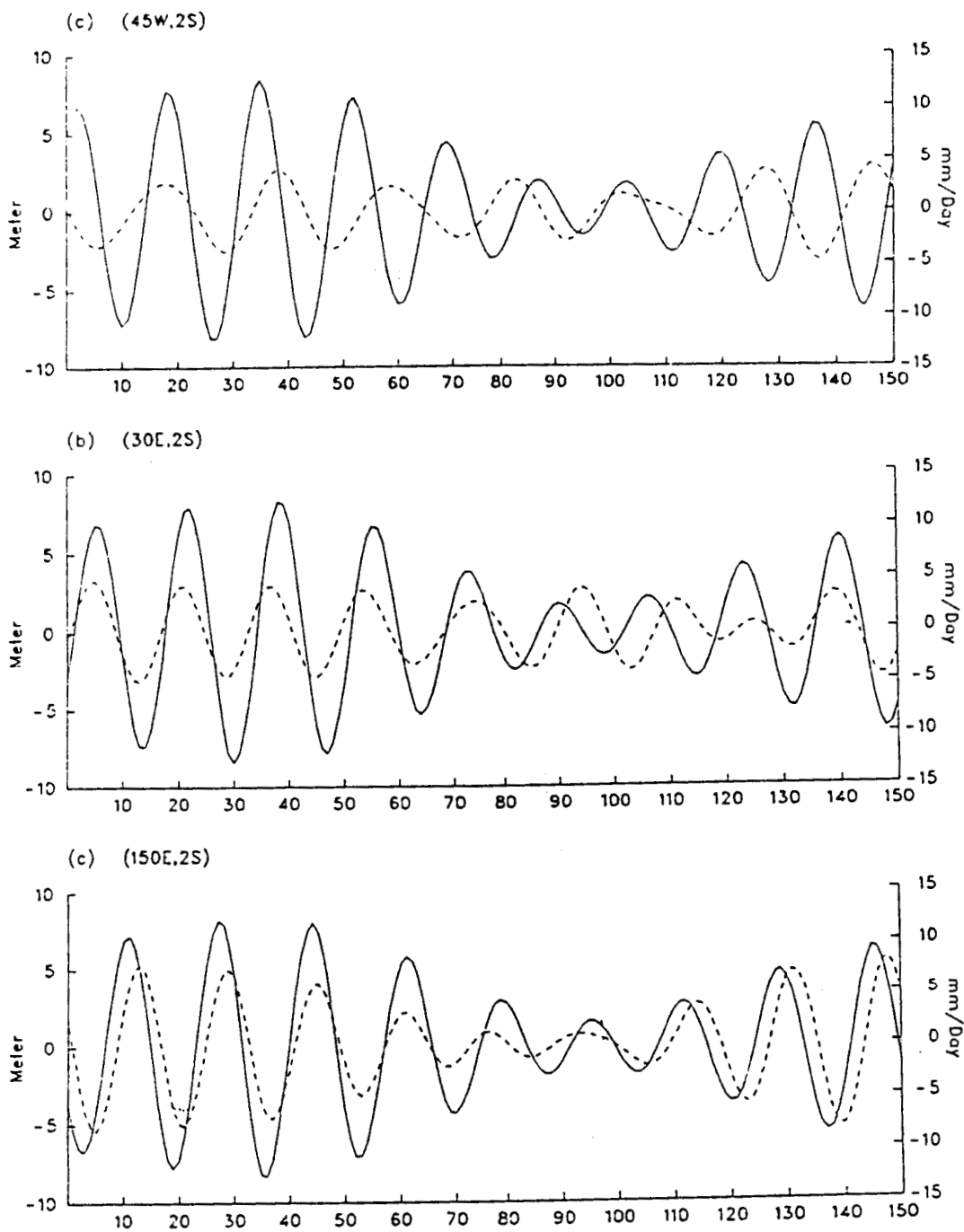


Figure A4. Same as Figure 8, except for the eastward moving periods of 15-20 days over the northern winter